Energy & Environmental Science

ROYAL SOCIETY OF CHEMISTRY

REVIEW

View Article Online
View Journal | View Issue

Cite this: *Energy Environ. Sci.*, 2023, **16**, 4872

Metal–iodine batteries: achievements, challenges, and future

Leiqian Zhang,[ab] Hele Guo,[c] Wei Zong,[b] Yunpeng Huang,[b] Jiajia Huang,*[d] Guanjie He,[e] Tianxi Liu,[b] Johan Hofkens[cf] and Feili Lai*[ac]

Received 25th May 2023,
Accepted 29th August 2023

DOI: 10.1039/d3ee01677c

rsc.li/ees

Metal–iodine batteries (MIBs) are becoming increasingly popular due to their intrinsic advantages, such as a limited number of reaction intermediates, high electrochemical reversibility, eco-friendliness, safety, and manageable cost. This review details past attempts and breakthroughs in developing iodine cathode-based (rechargeable) metal battery technology, to arrive at a comprehensive discussion and analysis of the battery's working mechanisms and fundamental challenges. Especially, the realization of available rechargeable MIBs relies heavily on the joint action of the battery components. We therefore cover here the progress starting from electrodes, electrolytes, and separator/interlayer requirements to introduce various types of MIBs and finally a critical analysis of the status quo, allowing us to gain insight into the roadblocks that still exist in MIBs. Also, we collect and compare the electrochemical performance of MIBs by category with listing their actual active material loading species and cell fabrication parameters. Finally, we conclude with recommendations for future strategies to leverage current advances in battery engineering, characteristics, and computational designs, all of which enable MIBs to reach their full potential in the energy age ultimately.

Broader context

The use of reversible redox reactions of chalcogens (O, S, and Se) and halogens (Cl, Br, and I) for energy storage has a long history due to their high theoretical capacity and abundance in feedstocks. Particularly, iodine has low toxicity, high reactivity, and few intermediates, leading to generally better electrochemical properties (*e.g.*, rate and cycling stabilities) than other elements. In addition, iodine also permits the creation of metal–iodine batteries (MIBs) by flexible pairing with different types of metal anodes, which readily caters to diverse forms of the electrochemical energy storage market. However, a number of issues, including iodine species dissolution, sluggish kinetics, anode corrosion/passivation, and dendrite growth, often lead to rapid capacity degradation, poor Coulombic efficiency, and even short-circuiting, greatly impeding the further practical application of MIBs. This review details past attempts and breakthroughs in developing iodine cathode-based (rechargeable) metal battery technology, while also presenting key innovations, deficiencies, and possible solutions for batteries. It is hoped that through this review article, further interest in MIBs will emerge, and efforts to make them useful for energy storage in the future will be triggered.

1 Introduction

The heightened global attention toward the energy crisis and global warming has triggered urgent investigations into carbon-free energy sources, such as wind and solar energy.[1,2] Especially, the recent surge in gas prices caused by Russia–Ukraine war appears to have accelerated the decarbonization process of the entire energy system from fossil-fuel-based power generation.[3] It is anticipated that, by 2050, nearly 27% of global energy consumption will come from renewable sources.[4] However, carbon-free energy sources usually have the characteristics of variability, uncertainty, and location-specificity. To make carbon-free energy compatible with our daily lives, efficient, flexible, and readily available electrical energy storage (EES) systems are essential.[5,6]

---

[a] *State Key Laboratory of Metal Matrix Composites, School of Materials Science and Engineering, Shanghai Jiao Tong University, Shanghai, 200240, P. R. China. E-mail: feililai@sjtu.edu.cn*

[b] *Key Laboratory of Synthetic and Biological Colloids, Ministry of Education, School of Chemical and Material Engineering, International Joint Research Laboratory for Nano Energy Composites, Jiangnan University, Wuxi, 214122, P. R. China*

[c] *Department of Chemistry, KU Leuven, Celestijnenlaan 200F, Leuven 3001, Belgium. E-mail: feili.lai@kuleuven.be*

[d] *School of Chemical Engineering, Zhengzhou University, Zhengzhou 450001, P. R. China. E-mail: huangjiajia@zzu.edu.cn*

[e] *Christopher Ingold Laboratory, Department of Chemistry, University College London, 20 Gordon Street, London, WC1H 0AJ, UK*

[f] *Department of Molecular Spectroscopy, Max Planck Institute for Polymer Research, Ackermannweg 10, Mainz 55128, Germany*

The development of lithium-ion battery (LIB) technology has revolutionized the way people live and brought energy into the era of portability. Despite these advancements, with the advent of electric vehicles and an increasing demand for large-scale energy storage solutions, the prices of raw materials for LIBs are sky-rocketing. For instance, as of February 2023, the price of battery-grade lithium carbonate increased by over 14 times, from around \$5816 ton^{-1} to approximately \$88 800 ton^{-1} in China (**https://www.ccmn.cn**). As a result, there is a significant research effort underway to develop new types of rechargeable battery systems as an adjunct or substitute to LIBs.

Typically, the conversion reactions of chalcogens (O, S, and Se) and halogens (Cl, Br, and I) have received significant attention because of their high theoretical storage capacity and abundance of raw materials (Table 1).[7–9] Through flexible matching with different types of metal anodes (*e.g.*, Li, Na, K, Mg, Al, Zn, and Fe), the as-prepared metal–element batteries can be well adapted for the speedy development of the electrochemical energy storage market.[9] Among them, metal–oxygen and metal–sulfur batteries are regarded as the most promising battery systems due to their outstanding advantages in energy density and price. However, the inherent instability and complexity of their intermediate products, including but not limited to polysulfide and peroxide/superoxide, pose great challenges for their applications.[10,11] On the other hand, the use of halogens for energy storage can be traced back to 1884.[12,13] Charles Renard employed a 435 kg zinc-chlorine battery to power the 52 m-long airship La France for flying about 8 km. Despite this, the high toxicity, high corrosiveness, and volatility of chlorine make chlorine-based solutions fundamentally unsuitable for large-scale energy storage.[14,15] Like chlorine, bromine also has been extensively studied for over a century.[14,15] Although it has low reactivity compared to chlorine, its inherent liquid nature, severe corrosiveness, and high toxicity also make it unusable in portable configurations.[16–18]

Significantly, metal–iodine batteries (MIBs) are gaining momentum in a wide variety of battery systems, including Li–I_2, Na–I_2, K–I_2, Zn–I_2, Mg–I_2, Al–I_2, and Fe–I_2 batteries.[19–25] This popularity can be attributed to the distinctive properties of iodine: (1) as an essential trace element in the human body, iodine is significantly safer, more stable, and more eco-friendly compared to chlorine and bromine.[12] Intriguingly, in late 1972, Li–I_2 primary cells were widely applied as a power source in cardiac pacemakers;[26] (2) iodine has high abundance in oceans (50–60 $\mu g_{\text{iodine}}\ L_{\text{ocean}}^{-1}$) and relatively low cost (~\$41 kg^{-1}), allowing its large-scale application;[12,27] (3) iodine possesses a high theoretical volumetric capacity (1040 mA h cm^{-3}), gravimetric capacity (211 mA h g^{-1}), and high redox potential (0.62 V *vs.* standard hydrogen electrode (SHE)), indicating a possible high energy density when it is coupled with an anode; and (4) although iodine has low solubility in water (~0.29 $g_{\text{iodine}}\ kg_{\text{water}}^{-1}$), it can spontaneously bond with iodide ions to form highly soluble triiodide, thereby significantly increasing its solubility (up to 8–12 M) and reaction kinetics.[28] Given these interesting properties, MIBs are poised to be a promising alternative to LIBs. It is high time for a systematic and up-to-date review of metal–iodine batteries.

In this review article, we first offer a historical perspective on MIBs to enable the reader to easily understand their development. Next, the electrochemistry principles, and the fundamental issues inherent in MIBs are discussed and analyzed in depth. Therefore, in Section 2, we further present a comprehensive overview of MIBs from the perspectives of iodine host, electrolyte, interlayer, separator, and anode, with a focus on how they achieve advanced electrochemical performance

Leiqian Zhang

Leiqian Zhang, graduated from Zhengzhou University in 2022 with a master's degree. Currently, he is pursuing his PhD degree at Jiangnan University. His research interests mainly focus on electrode and electrolyte design for iodine-based batteries.

Jiajia Huang

Jiajia Huang received his PhD degree in polymeric chemistry and physics from Sun Yat-Sen University in 2014. Currently, he is an associate professor at the School of Chemical Engineering, Zhengzhou University. His research focuses on functional polymers and carbon-based materials and their applications in adsorption separation of metal ions and electrochemical energy storage.

Feili Lai

Feili Lai received his PhD degree from the Max Planck Institute for Colloids and Interfaces/Potsdam University in 2019. His current interests include the design and synthesis of low-dimensional solids for energy storage and conversion applications, smart polygels, and theoretical calculations.

Table 1 Advantages and disadvantages of iodine over other chalcogens (O, S, and Se) and halogens (Cl and Br)[7,29–44]

	O	S	Se	Cl	Br	I
Price ($ Kg^{-1})	Available from the air	0.15	31.3	0.04 (NaCl)	2.5	41
Abundance (wt%, in the Earth's crust)	47	0.047	5×10^{-6}	0.017; 19 g L^{-1} (ocean)	2.1×10^{-4}; 65 mg L^{-1} (ocean)	4×10^{-5}; 55 μg L^{-1} (ocean)
Specific capacity (mA h g^{-1})	3860 (Li–O_2); 820 (Zn–O_2)	1672 (S^{2-}/S^0)	675 (Se^{2-}/Se^0)	755 (Cl^-/Cl^0)	335.5 (Br^-/Br^0)	211 (I^-/I^0); 422 (I^-/I^+)
Potential (V *vs.* SHE)	2.96 (Li–O_2); 1.65 (Zn–O_2)	−0.57 (S^{2-}/S_8)	−0.67 (Se^{2-}/Se^0)	1.36 (Cl^-/Cl^0)	1.08 (Br^-/Br^0)	0.62 (I^-/I^0); 1.07 (I^0/I^+)
Safety	High	High	High	Low	Moderate	High (essential element)
Cycle life	Low	Moderate	Moderate	Moderate	Moderate	High (up to 50 000 cycles)
Rate capacity	Low	Low	Moderate	Low	Moderate	High (up to 100C)

during battery operation. Also, advanced computational methods and *in situ* characterization techniques used in MIBs are summarized in Section 3. On this basis, Section 4 summarizes the key innovations and design guidelines of these strategies, and also suggests the corresponding deficiencies and possible solutions. Besides, the placement of various MIBs is discussed and analyzed in combination with the actual situation, while the future development and application of MIBs are also put forward. We hope that through this review article, more interest in metal–iodine batteries will be generated, and efforts to make them useful in energy storage in the future will be sparked.

1.1 Historical perspective (–2023): a myriad of concepts

Iodine (Greek: ioeides, violet) was accidentally discovered by Bernard Courtois in 1811 and named by Humphrey Davy in 1813.[45] For a long time thereafter, iodine was mainly used to treat and prevent goiter. It was not until 1900 that Crotogino began to study the electrochemical properties of iodine.[46] And in 1968, the first primary solid-state lithium–iodine (Li–I_2) cell was conceived by workers at the Catalyst Research Corporation (Fig. 1).[47] Then, in late 1972, it was introduced into commercial medical devices as a power source for cardiac pacemakers. Commonly, such a cell is composed of a lithium anode, lithium iodide, and a poly(2-vinylpyridine)–iodine (P2VP–I_2) cathode. Among them, lithium iodide, as a solid-state electrolyte, is formed *in situ* by the direct contact between the lithium anode and P2VP–I_2, while increasing in thickness with battery discharge. However, its poor lithium-ion conductivity (*ca.* 10^{-7} S cm^{-1} at room temperature), and increased thickness lead to poor rate capability of the cell (60 μA cm^{-2} at room temperature).[47,48] Therefore, intensive efforts have been devoted to improving the discharge rate and the low-temperature performance of lithium–iodine cells by designing advanced active cathodes or increasing the anode surface area.[48–51] Weinstein *et al.* first surveyed the electrochemical solid-state rechargeable Li–I_2 cells with the polyvinylpyrrolidone (PVP)–I_2 complex as the cathode in 2008.[52] Especially, with the rise of hybrid electric vehicles and modern mobile life, a novel all solid-state rechargeable Li–I_2 thin film battery was first proposed by Liu and co-workers in 2011.[48] In this system, the Li–I_2 battery is fabricated with a solid I_2-LiI(3-hydroxypropionitrile)$_2$ cathode and a Li anode, in which the rechargeability is made possible through the ionic conductivity of I^- anions. Despite its limited current density (about 20 μA cm^{-2}), this battery sparked considerable interest in rechargeable Li–I_2 batteries. In the years that followed, Li–I_2 battery technology continued to achieve breakthroughs. As of 2022, state-of-the-art Li–I_2 batteries can endure more than 10 000 cycles at 50C (1C = 211 mA g^{-1}) with an iodine loading of 80 wt%.[53] However, the development of other alkali metal batteries (Na–I_2 and K–I_2) has been slow in comparison with Li–I_2 batteries. Until 2015, Ingersoll *et al.* showed a prototype of a high-temperature sodium–iodine battery based on NaSICON ceramics, and an inorganic NaI/$AlCl_3$-based catholyte.[54] Furthermore, Gong *et al.* also proposed a room-temperature Na–I_2 battery with iodine quantum dots decorated reduced graphene oxide as the free-standing cathode in 2016.[55] On the other hand, due to the higher activity and larger atomic radius of K metal, the K–I_2 battery was not realized until 2018.[56]

In terms of multivalent MIBs, the Zn–I_2 battery enjoys the most extensive research due to the high operability and suitable redox potential of Zn metal. In 1981, the pioneers Yamamoto *et al.* built the first primary Zn–I_2 cell by employing polymer–iodine adducts as the cathode and Zn metal as the anode.[57] Then, they further succeeded in fabricating a Zn–I_2 secondary battery in 1984 by introducing an additional ion-exchange membrane and carbon powder conductor into the battery structure.[58] Despite this, the assembled battery undergoes only approximately 300 cycles due to the evaporation of aqueous electrolytes and partial degradation or corrosion of positive and negative electrodes. It is notable that the progress of Zn–I_2 battery research slowed down after the emergence of LIB technology. In 2017, with the development of Zn–I_2 flow batteries, Li *et al.* reported an up-to-date Zn–I_2 battery with iodine/microporous carbon as the cathode and $ZnSO_4$ as the electrolyte, marking the beginning Zn–I_2 battery research.[59] By January 2023, more than 100 articles on Zn–I_2 batteries have been published (data from Web of Science). Furthermore, the rise of Zn–I_2 batteries has brought attention to Fe–I_2 batteries because of their high reversibility, abundant resources, low costs, and non-toxicity of iron anodes.[19,60] In 2020, Bai and colleagues reported the first rechargeable Fe–I_2 battery that showed an excellent cycle stability of 100% after 550 cycles at 2000 mA g^{-1}.[19] Besides, Wu *et al.* recently further improved the lifecycle of Fe–I_2 batteries to 1200 cycles using a polyaniline cathode and a mixed electrolyte (5 M $FeCl_2$ and 1 M ZnI_2), which confirmed the promising potential of Fe–I_2 batteries as a

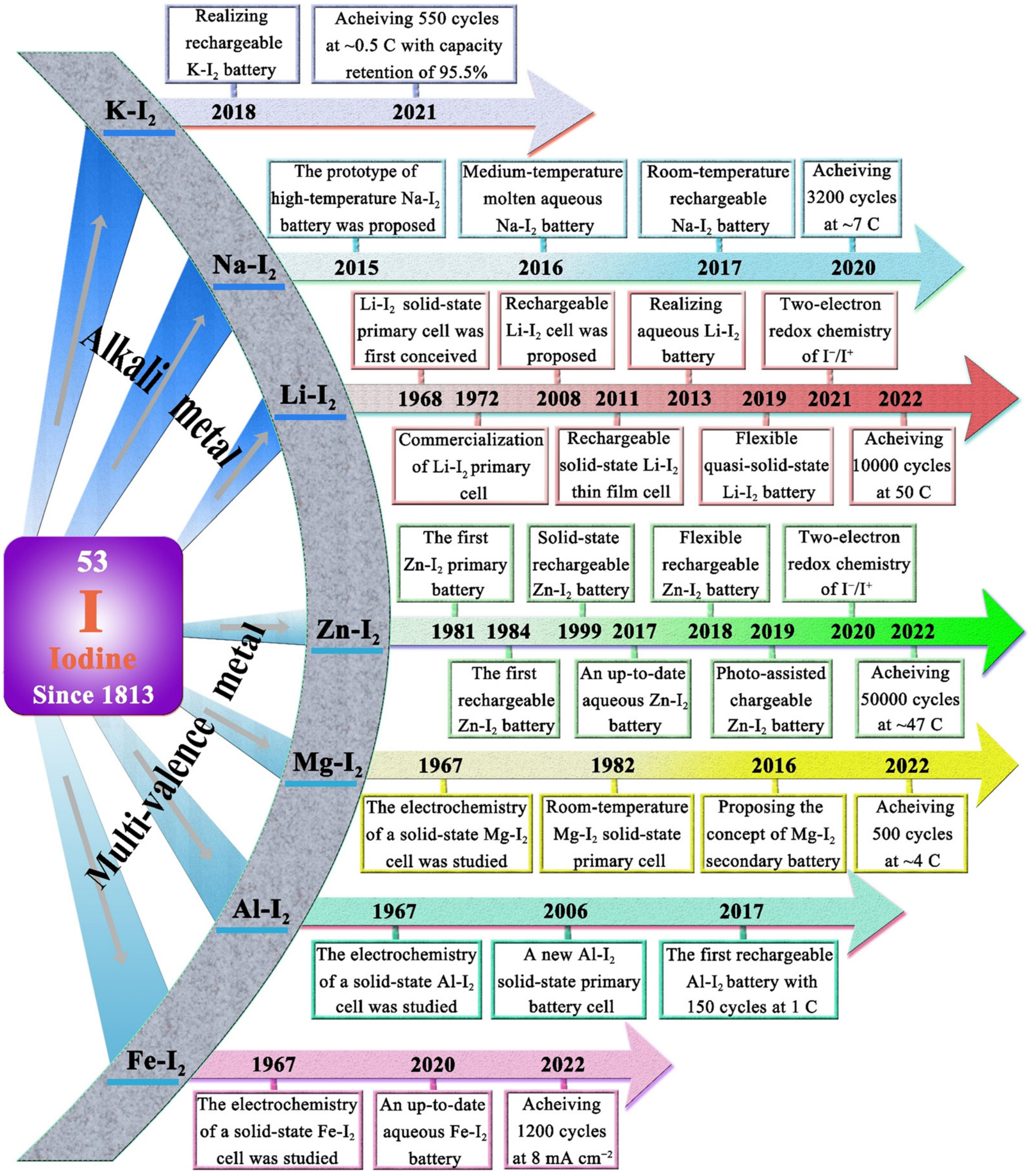

Fig. 1 Development timeline of various MIBs.[18,19,21,24,25,28,42,48,52–59,61,62,68–78]

low-cost, eco-friendly, and safe large-scale EES system.[61] Apart from Zn/Fe–I_2 batteries, the Mg–I_2 battery was also studied in 1967 by Gutmann and co-workers.[62] As compared to traditional intercalation cathodes in Mg-ion batteries, the conversion-type iodine cathode could well bypass the sluggish cation dissociation and solid-state ion diffusion process caused by high charge densities of Mg^{2+}.[63,64] Nevertheless, the high susceptibility of Mg to contaminants (*e.g.*, water, oxygen, carbon dioxide, protic residues, and polysulfide) results in a strong tendency to form a compact passivating surface film, which greatly blocks the electrochemical reaction on the Mg anode.[65] Consequently, the development of Mg–I_2 batteries lag far behind that of Zn–I_2 batteries due to practical limitations. As the discovery of new electrolytes always plays a key role in the advancement of battery technology, Li *et al.* first presented the concept of a Mg–I_2 secondary battery using ionic liquid as the electrolyte in 2016.[21] However, the long-term cycling performance data for this system was not initially available. Fortunately, a rechargeable Mg–I_2 battery was then implemented by Tian *et al.* in 2017, which exhibited a remarkable capacity retention of 94.6% after 120 cycles at 0.5C, demonstrating the feasibility of Mg–I_2 secondary batteries.[66] Similar to the Mg–I_2 battery, the use of a conventional aluminum anode in an Al–I_2 battery is problematic due to the formation of ionic and electrically insulating passivation layers.[67] While research on Al–I_2 batteries can be traced back to 1967,[62] the rechargeable Al–I_2 battery was developed by Tian *et al.* in 2017.[25]

1.2 Working principle

Commonly, MIBs are a type of conversion battery system, in which the storage of electric energy is based on the reversible redox reaction between a metal anode and an iodine cathode.

Most MIBs operate in a neutral or mild-acidic electrolyte, as iodine undergoes spontaneous disproportionation in an alkaline medium.[79] Therefore, an ideal redox event in the anodic region of MIBs can be represented using the following equation:

$$M \leftrightarrow M^{n+} + ne^{-} \quad (1)$$

where M represents the metal anode. During the discharge (oxidation) process, the generated metal ions and electrons move from the metal anode to the iodine cathode *via* the internal electrolyte and external electrical circuit, respectively. While charging, the metal ions from the iodine cathode are reduced back at the metal anode with the input of external energy, thus creating a reversible cyclic process.

The iodine cathode, on the other hand, involves various reaction processes that can be classified into the following five categories. (1) Intermittent two-step conversion reaction ($I^- \leftrightarrow I_3^-$, $I_3^- \leftrightarrow I_2$). This process is common in MIBs that utilize organic electrolytes, such as lithium bis(trifluoromethane sulfonyl) imide (LiTFSI) in 1,3-dioxolane/tetra-ethylene glycol dimethyl ether or 1,3-dioxolane/1,2-dimethoxyethane.[79,80] Some special gel electrolytes (*e.g.*, poly(ethylene oxide)-poly(propylene oxide)-poly(ethylene oxide)) in aqueous Zn–I_2 cells also lead to the formation of the above mechanism.[81,82] As shown in Fig. 2a, its typical cyclic voltammetry curve contains two pairs of redox peaks, for which the electrochemical reaction is essentially the reversible redox reaction of $I^- \leftrightarrow I_3^-$ and $I_3^- \leftrightarrow I_2$. Interestingly, Li *et al.* recently suggested that the peaks situated at high potential relate to the new chemistry of the $I^0 \leftrightarrow I^+$ pair instead of $I_3^- \leftrightarrow I_2$, when using 0.1 M LiCl as an additive in the electrolyte of Li–I_2 cells.[18] This controversial view makes it necessary for future work to ascertain the transformation mechanism of iodine in organic electrolytes in detail. (2) One-step incomplete iodine redox process ($I^- \leftrightarrow I_3^-$). This process is typically observed in MIBs with aqueous electrolytes (Fig. 2b). It is worth noting that when there is an excess production of I_2 at high charging states, I_3^- can be converted into higher-order polyiodide ions (I_5^-, I_7^-, *etc.*). This is due to the continuous combination of I_2 and polyiodide during cycling, which results in the formation of I_x^- in an aqueous solution. Significantly, the distinction between type (1) and type (2) mechanisms may be due to the solubility disparity of iodine species in different electrolytes (aqueous electrolytes: I^- (high), I_3^- (high), and I_2 (low); tetraglyme electrolytes: I^- (low), I_3^- (high), and I_2 (high)), which would affect the formation and stabilization of iodine intermediates during redox processes.[66] Despite this, in-depth studies are urgently needed to reveal the nature of the electrolyte affecting the reaction mechanism of MIBs. (3) One-step one-electron conversion process ($I^- \leftrightarrow I^0$). This mechanism is

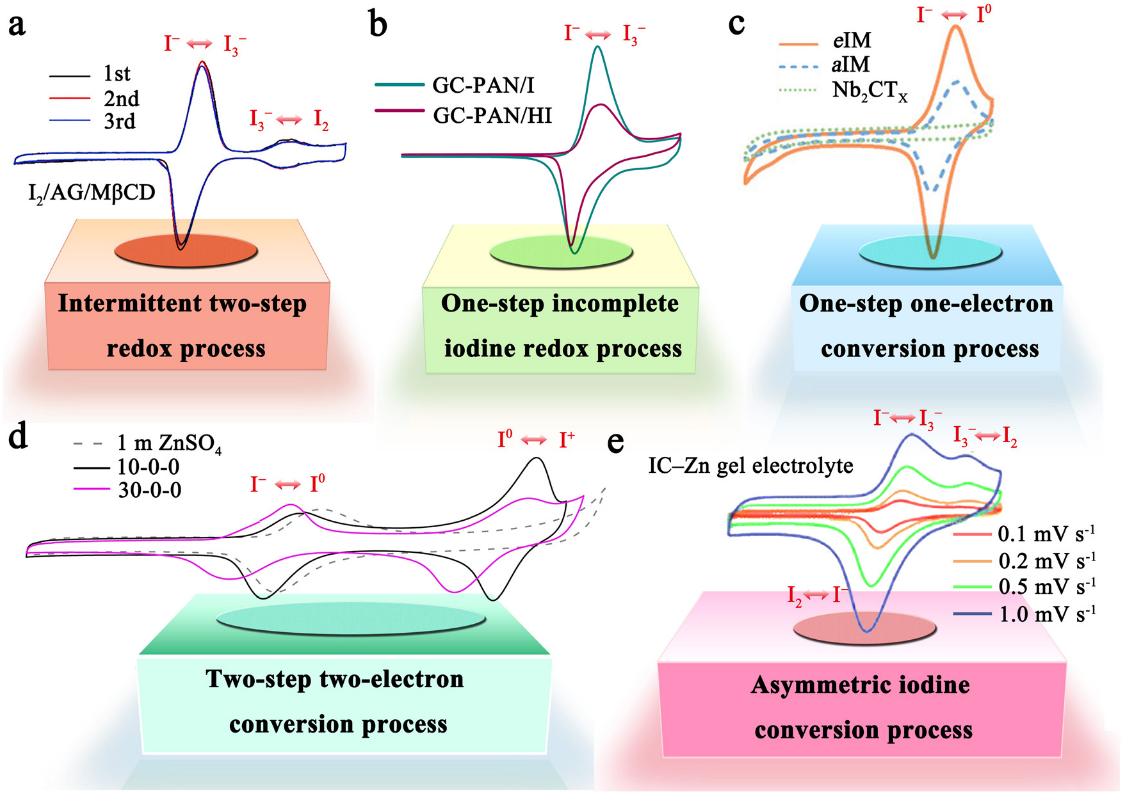

Fig. 2 Five representative reaction mechanisms of iodine cathodes in MIBs. (a) An intermittent two-step redox process ($I^- \leftrightarrow I_3^-$, $I_3^- \leftrightarrow I_2$). Reprinted with permission from ref. 89. Copyright 2020 Elsevier. (b) One-step incomplete iodine redox process ($I^- \leftrightarrow I_3^-$). Reprinted with permission from ref. 27. Copyright 2022 Wiley. (c) One-step one-electron conversion process ($I^- \leftrightarrow I^0$). Reprinted with permission from ref. 83. Copyright 2021 Wiley. (d) Two-step two-electron conversion process ($I^- \leftrightarrow I^0$, $I^0 \leftrightarrow I^+$). Reprinted with permission from ref. 40. Copyright 2021 Springer Nature. (e) Asymmetric iodine conversion process (oxidation: $I^- \leftrightarrow I_3^-$, $I_3^- \leftrightarrow I_2$; reduction: $I_2 \leftrightarrow I^-$). Reprinted with permission from ref. 88. Copyright 2023 Royal Society of Chemistry.

currently only found in aqueous Zn–I_2 batteries (Fig. 2c). Possible explanations for this reaction mechanism can be attributed to the following reasons: (1) the rapid electron supply of iodine host materials (*e.g.*, Nb_2CT_X flakes) enables a forceful one-step conversion between the I^- ion and I_2 element;[83] (2) the appropriately sized pores (*e.g.*, carbon cloth with a typical micropore size of around 6.3 Å) of iodine host material make it difficult for the distorted octahedral configuration of $Zn(I_3)_2$ (minimum diameter of 9.5 Å) to reside inside the material's channel;[72,84] (3) specific electrolytes (*e.g.*, high concentrations of $ZnCl_2$ and eutectic electrolytes) can hinder the formation of I_3^- by restricting the amount of free H_2O, leading to difficulties in the binding between I^- ions and I_2.[40,85,86] It is remarkable that, due to the absence of polyiodide, this mechanism is more conducive to the cycling stability of MIBs. (4) Two-step two-electron conversion process ($I^- \leftrightarrow I^0$, $I^0 \leftrightarrow I^+$). The corresponding cyclic voltammetry curve in Fig. 2d displays two processes of $I^- \leftrightarrow I^0$ and $I^0 \leftrightarrow I^+$. In particular, the energy density of MIBs is significantly increased by the high redox potential (up to 1.07 V *vs.* SHE) of the $I^0 \leftrightarrow I^+$ couple.[40,74] Nevertheless, this process requires to be implemented in a very harsh environment, since I^+ is very unstable in aqueous electrolytes and could be further oxidized to form irreversible IO_3^-.[40,87] Remarkably, the addition of nucleophilic species (*e.g.*, halide, cyanide, and amines) into the electrolyte can stabilize I^+ ions through the formation of charge-transfer complexes.[40] Besides, electrolyte activity towards I^+ ions is also an essential factor that impacts the conversion process's reversibility. Therefore, Zou *et al.* chose acetonitrile which is inert to I^+, as a diluent to promote the ion transport and tune the activity of H_2O in the electrolyte solution, thereby realizing 6000 cycles in a Zn–I_2 battery based on two-electron conversion.[40] Despite these strict conditions, this high voltage redox chemistry potentially represents a new avenue into MIBs. (5) Asymmetric iodine conversion process (oxidation: $I^- \leftrightarrow I_3^-$, $I_3^- \leftrightarrow I_2$; reduction: $I_2 \leftrightarrow I^-$). This process has only been observed in limited instances, specifically in the Zn–I_2 cell using a high-conductivity iota-carrageenan gel electrolyte (Fig. 2e).[88] The factors contributing to its occurrence are still unknown and necessitate further research.

1.3 Fundamental issues

Throughout the development history and internal reaction mechanisms of MIBs described above, several fundamental issues have greatly hindered the widespread success of rechargeable MIBs. The foremost problem is the shuttle effect of iodine species, *i.e.*, iodine and polyiodide, formed during the charge/discharge cycling process. These species dissolve uncontrollably into the electrolyte and subsequently diffuse towards the anode side. The outcomes include severe capacity degradation, rapid self-discharge, and low Coulombic efficiency of the battery (Fig. 3a).[90] To address this issue, it is noteworthy that the iodine host materials in MIBs should strongly interact with iodine species, leading to great enhancement in the thermal stability of iodine species in composites.[53] Thus, the thermal instability of iodine species (iodine is volatile even at room temperature) may be considered as a less important issue in MIBs. Another critical issue for MIBs is the insulating property of iodine that inevitably results in poor redox kinetics, low

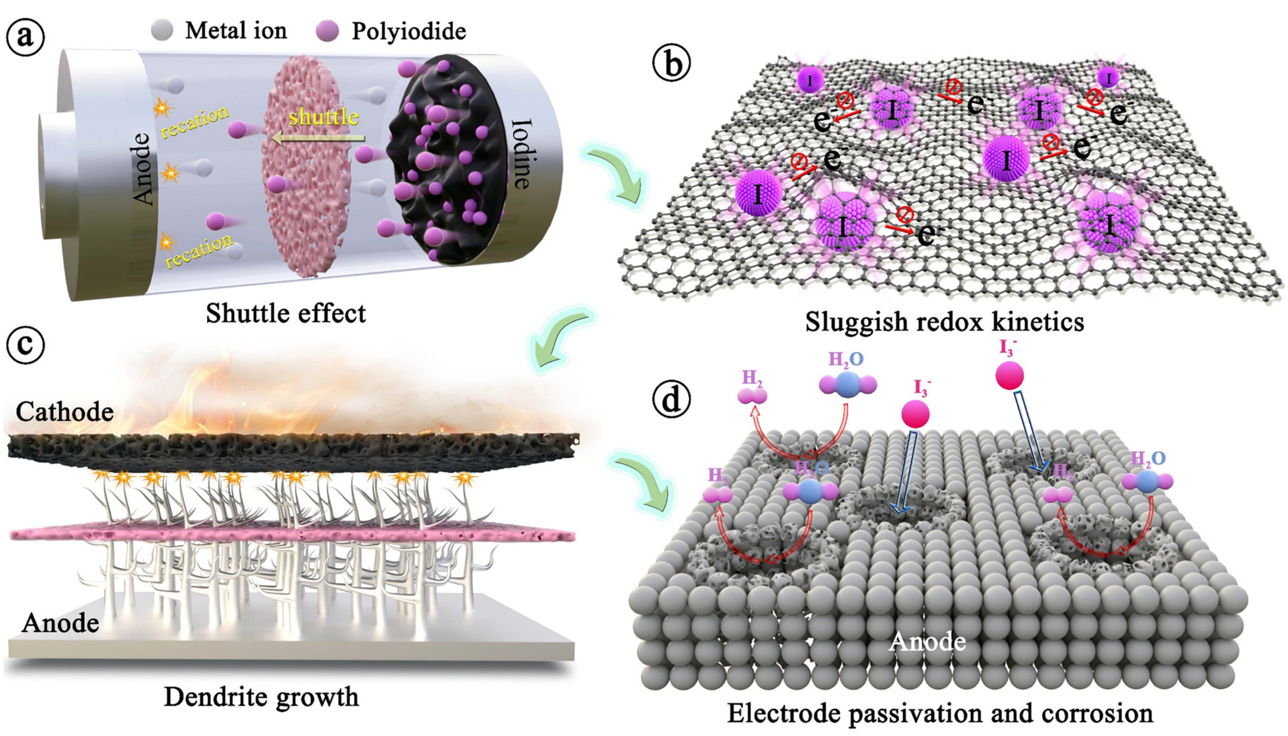

Fig. 3 Four fundamental issues faced by metal–iodine batteries. (a) The shuttle effect of iodine species. (b) Intrinsic insulation of iodine. (c) Dendrite growth on anodes. (d) Passivation and corrosion of metal anodes.

energy/iodine utilization, and high polarization (Fig. 3b).[83,91] In addition, the long-term cycle performance of the whole battery also depends heavily on the metal anode. Initially, the anode has minimal impact on battery performance, but as non-uniform plating/stripping of metal anodes (except Mg) causes dendrite growth, there is a risk of a short circuit, creating a severe safety hazard for the battery system (Fig. 3c). Besides, the formation of dendrites can result in "dead" metal, that is, dendrites fall off into the electrolyte, making it unsuitable for reuse, which commonly leads to rapid deterioration of battery performance. Meanwhile, the side reactions occurring between the metal anodes and electrolytes also frequently cause the corrosion and passivation of metal anodes; this not only consumes fresh metals and limited electrolytes, but also increases the impedance with severely restricted subsequent reaction of anodes, resulting in poor plating/stripping CE (Fig. 3d).[92] Significantly, corrosion/passivation and dendrite growth interact and promote each other, accelerating the end of cell life.[93] Extensive efforts that surround the above fundamental question have been carried out on various metal–iodine systems. Especially, the design of the iodine host, anode, separator, and electrolyte commonly affects kinetics (power), lifetime, and safety, while also tuning the limits of cell voltage and energy density. To account for these, we sort out and analyze MIBs from the above aspects based on available research results in the following sections systematically and comprehensively.

2 Metal–iodine batteries

2.1 Lithium–iodine battery

Tables 2–17 summarizes the electrochemical performance, fabrication parameters, and cell-testing conditions for metal–iodine batteries (MIBs) using different strategies, from 2011 to 2023. Among various MIBs, Li–I_2 batteries are at the forefront of development. This is closely related to the keen interest in the research of lithium-based batteries (*e.g.*, Li–O_2 and Li–S batteries). Undoubtedly, it is also inseparable from the inherent benefits of Li–I_2 batteries. One advantage of Li–I_2 cells lies in their iodine/iodide redox chemistry that results in an open-circuit voltage of $\sim$3.5 V for Li/Li^+. Additionally, the limited number of intermediates and rapid iodine conversion reaction enable the state-of-the-art Li–I_2 battery to achieve over 10 000 cycles with a high-power density of 29 kW kg^{-1}. Nonetheless, the aforementioned fundamental problems in Fig. 3 still plague the development of Li–I_2 batteries. Through a combination of tabularized numbers and the detailed discussion below, we hope to make it easier for readers to understand the development and progress of Li–I_2 batteries. In particular, the specific capacities of batteries in this article are calculated based on the mass of iodine, unless otherwise stated.

2.1.1 Iodine host

2.1.1.1 Carbon-based iodine host. Generally, it is not feasible to directly employ iodine as a cathode due to the high solubility of iodine in organic electrolytes and inherent insulating properties. Therefore, it is crucially important to have an effective host that can effectively store iodine and promote its utilization for high-performance MIBs. Table 2 presents critical data pertaining to hosts for Li–I_2 batteries, where carbon-based materials have been used extensively as hosts for iodine and are considered highly advantageous. This can be attributed to their three prominent characteristics: (1) the abundant pores and high specific surface area of carbon-based hosts can provide strong adsorption, decreasing the solubility of active iodine species in organic electrolytes and thereby improving the stability of batteries; (2) the capacitive properties of carbon-based hosts can provide additional capacity and increase the energy density of rechargeable Li–I_2 batteries; and (3) carbon-based materials normally have high conductivity and excellent electronic transfer ability, thus leading to improved utilization of iodine species despite their inherent insulating properties. Given these, Wang *et al.* first employed conductive carbon black borrowed from Li–S batteries as an iodine host, which exhibited a lifetime of up to 1000 cycles and a capacity retention of 71.4% at a current density of $\sim$24C (Fig. 4a).[94] Subsequently, carbon cloth, 3D bio-foam carbon, and active graphene were also investigated as iodine hosts.[79,95,96] Since free-standing carbon cloth is commercially available, has moderate iodine species binding, and can compound well with other active materials as a carrier, it is currently often used as a current collector in MIBs to provide dual iodine fixation.[97–99] On the other hand, Li–I_2 batteries exhibit a light-assisted charging behavior after combining the N719-dye@TiO_2 photo-electrode with the iodine@activated carbon cathode (Fig. 4b).[100] Despite this, the performance of these carbon-based hosts is less than satisfactory ($\leq$1000 cycles), as their inertness leads to low interaction with iodine species.

In this regard, several approaches have been developed to enhance the performance of carbon-based hosts. One basic approach is elemental doping, which involves incorporating polar heteroatoms like nitrogen and phosphorus atoms into carbon materials. Theoretically, these heteroatoms with abundant lone pair electrons would change the inertness of carbon materials, thereby effectively enhancing the interaction between the carbon support and iodine species with rapid charge transfer. As reported by Lu's group, Li–I_2 batteries fabricated from nitrogen and phosphorus co-doped hierarchically porous graphitic carbon (HPMC-NP) hosts could achieve a high capacity retention of 84.5% after 2000 cycles at a current density of 500 mA g^{-1} (Fig. 4c).[101] Furthermore, given the carbon cloth as the current collector, Lai's group prepared a free-standing oxygen-doped porous carbon-coated carbon cloth@iodine host by *in situ* carbonization of the metal organic framework (MOF) precursor. As a result, the as-prepared Li–I_2 batteries could maintain an ultra-high capacity retention of 91% after 3500 cycles at 10C, which well proves that heteroatomic doping is an effective method to improve the performance of Li–I_2 batteries. However, hollow carbon spheres do not show a significant improvement in cell cycle stability performance ($\leq$500 cycles) after heteroatom doping.[102,103] A plausible explanation is that iodine or polyiodide tends to detach from the hollow carbon surface during the cycling process, leading to a rapid loss of active species.[104] Therefore, it is recommended to refrain from utilizing carbon

Table 2 Electrochemical performance, fabrication parameters, and cell-testing conditions of different parts in MIBs from 2011 to 2023. Iodine host materials in Li–I_2 batteries

1	2	3	4	5	6	7	8	9	10
2011	I_2/conductive carbon black	1 M $LiPF_6$ in EC/EMC/DMC (1 : 1 : 1, v/v/v)	24	~1.2	~24	1000	71.4	125	94
2015	I_2/nanoporous carbon cloth	1 M LiTFSI/1 wt% $LiNO_3$ in DOL/DME (1 : 1, v/v)	22	5.6	0.5	300	~64.8	195	95
2017	$TiC_{0.7}N_{0.3}$/liquid I_2	1 M $LiNO_3$/0.04 M I_2/0.02 M LiI in DMA	—	1	10 mA cm^{-2}	7000	—	100	111
2017	I_2/N-doped carbon hollow folded hemisphere	1 M LiTFSI/1 wt% $LiNO_3$ in DOL/DME (1 : 1, v/v)	32	—	~5	300	84	—	102
2017	I_2/3D bio-foam carbon	1 M LiTFSI/1 wt% $LiNO_3$ in DOL/DME (1 : 1, v/v)	30–40	~1–1.5	10/4	500	94	—	96
2017	I_2/active graphene	1 M LiTFSI/0.2 M $LiNO_3$ in DOL/TEGDME (1 : 1, v/v)	56	1–1.4	1	500	73.8	161	79
2017	I_2/N,P co-doped porous graphitic carbon	1 M LiTFSI/1 wt% $LiNO_3$ in DOL/DME (1 : 1, v/v)	—	2	~2.4	2000	84.5	~250	101
2018	PVP–I/N-doped hollow carbon sphere–I_2	1 M LiTFSI/1 wt% $LiNO_3$ in DOL/DME (1 : 1, v/v)	~35	—	4	400	86	—	103
2018	I_2/β-cyclodextrin	1 M LiTFSI/1 wt% $LiNO_3$ in DOL/DME (1 : 1, v/v)	15	~0.9	0.1	300	~93.7	164	80
2018	LiI/meso–micro porous carbon polyhedrons	4.5 M LiTFSI/0.1 M $LiNO_3$ in DOL/DME (1 : 1, v/v)	30 (LiI)	~1–1.2	2	800	~83.2	200.1	107
2018	Activated carbon cloth/PVP–I	1 M LiTFSI/1 wt% $LiNO_3$ in DOL/DME (1 : 1, v/v)	~10–11	1.6–1.8	8	2400	~81	240	98
2018	PVP–I	1 M LiTFSI/1 wt% $LiNO_3$ in DOL/DME (1 : 1, v/v)	13	2	2	1100	79.1	190.6	109
2019	LiI/N,P co-doped carbon cloth	1 M LiTFSI/1 wt% $LiNO_3$ in DOL/DME (1 : 1, v/v)	—	~0.2 (LiI)	10	2000	95.8	200.2	97
2020	I_2/active graphene/methyl-beta-cyclodextrin	1 M LiTFSI/0.2 M $LiNO_3$ in DOL/TEGDME (1 : 1, v/v)	51	~0.5–0.8	1	500	87.3	~194.4	89
2020	I_2/active graphene/PVP	1 M LiTFSI/0.2 M $LiNO_3$ in DOL/TEGDME (1 : 1, v/v)	49	~0.5–0.8	1	500	90.1	~200.1	89
2020	I_2/active graphene/amylose corn starch	1 M LiTFSI/0.2 M $LiNO_3$ in DOL/TEGDME (1 : 1, v/v)	50	~0.5–0.8	1	500	79.7	~178.6	89
2021	Graphene oxide/CNT/few-layer iodine nanosheets	1 M LiTFSI/1 wt% $LiNO_3$ in DOL/DME (1 : 1, v/v)	41	1.0–1.5	~9.5	1000	—	93.2	108
2021	N-containing porous carbon/carbon fiber cloth/PVP–I	0.5 M LiTFSI/0.5 M $LiNO_3$ in DOL/DME (1 : 1, v/v)	8	—	1	3000	79.7	~119.6	264
2021	LiI/active graphene	1 M LiTFSI/0.2 M $LiNO_3$ in DOL/TEGDME (1 : 1, v/v)	40 (LiI)	~0.4–0.6	~0.95	1000	93.7	232.0	265
2022	Methylamine hydroiodide	1 M LiTFSI in DOL/DME (1 : 1, v/v)	80	—	5	10 000	98.3	207.6	53
2022	I_2/MOF derived carbon/carbon cloth	1 M LiTFSI/1 wt% $LiNO_3$ in DOL/DME (1 : 1, v/v)	~44	1–2	10	3500	91	~257.5	99
2022	I_2@AC/N719-dye/TiO_2	1 M LiTFSI/3 wt% $LiNO_3$ in DOL/TEGDME	~40	1.0–1.6	~0.47	20	—	—	100
2022	I_2/hydrogen bonded organic framework@$Ti_3C_2T_x$	1 M LiTFSI/1 wt% $LiNO_3$ in DOL/DME (1 : 1, v/v)	44.3	~0.93	0.2	300	~79.1	~260	146

1, year; 2, cathode; 3, electrolyte formula; 4, the mass loading of iodine at the cathode (wt%); 5, the area loading of iodine at the cathode (mg cm^{-2}). Evaluation of Li–I_2 cell performance: 6, current density (C, 1C = 211 mA g^{-1}); 7, cycle number; 8, capacity retention (%); 9, reversible capacity (mA h g_{iodine}^{-1}). 10, reference. PVP, polyvinyl pyrrolidone; CNT, carbon nanotube; AC, activated carbon; LiTFSI, $LiN(CF_3SO_2)_2$; EC, ethylene carbonate; DOL, 1,3-dioxolane; DME, dimethoxyethane; DMC, dimethyl carbonate; DMA, dimethylacetamide; EMC, ethyl methyl carbonate; TEGDME, tetraethylene glycol dimethyl ether.

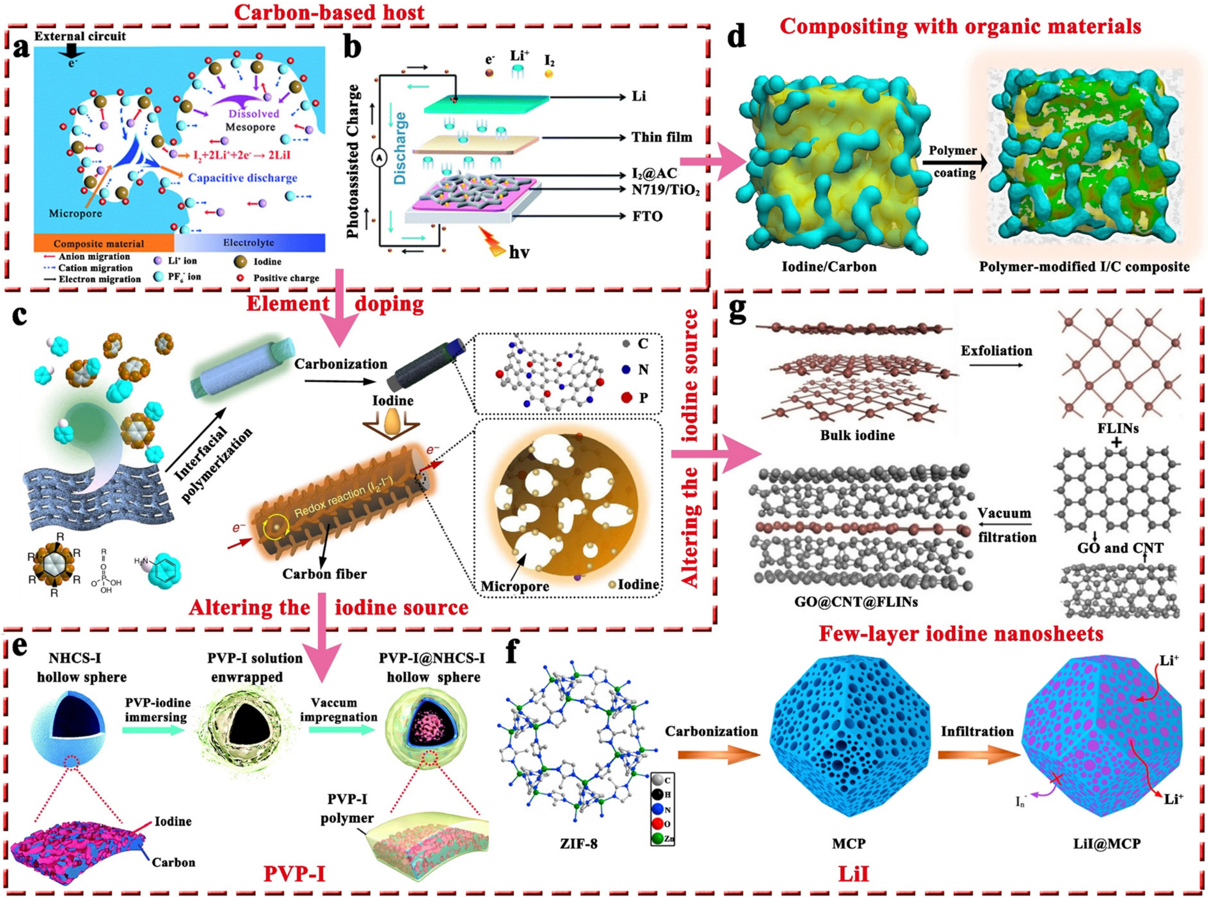

Fig. 4 (a) Schematic illustration of the discharge mechanism of iodine in the iodine@conductive carbon black composite in Li–I_2 batteries. Reprinted with permission from ref. 94. Copyright 2011 Royal Society of Chemistry. (b) Schematic diagram of the structure of a photo-assisted rechargeable Li–I_2 battery. Reprinted with permission from ref. 100. Copyright 2022 Royal Society of Chemistry. (c) Schematic diagram of the preparation process of HPMC-NP@iodine composite. Reprinted with permission from ref. 101. Copyright 2017 Springer Nature. (d) Schematic description of the fabrication process for the polymer-modified I_2@carbon composite. Reprinted with permission from ref. 89. Copyright 2020 Elsevier. (e) Schematic of the "top-down" synthesis process of N-doped carbon sphere@PVP–I composite. Reprinted with permission from ref. 103. Copyright 2018 Royal Society of Chemistry. (f) Schematic of the synthesis process of LiI@meso–micro porous carbon polyhedrons composite. Reprinted with permission from ref. 107. Copyright 2017 Elsevier. (g) Schematic illustration of the fabrication process of graphene oxide@carbon nanotubes@FLINs film. Reprinted with permission from ref. 108. Copyright 2021 Wiley.

materials with hollow structures when hosting iodine. Nonetheless, if unavoidable, such materials' cavities should not exceed the size of the iodide, allowing for better confinement of the active substance within the hollow structure.[105,106]

In addition to the aforementioned solution, organic materials capable of chemisorption to capture iodine have also been reported to enhance the electrochemical performance of carbon-based hosts (Fig. 4d).[89] Commonly, porous carbons are highly conductive, but their weak physical adsorption abilities can poorly restrict iodine species, particularly on cathodes with a high iodine loading amount.[89] On the other hand, rich polar functional groups in organic materials can lead to strong chemisorption to trap dissolved iodine species, but generally, they have poor electrical conductivity. Given all these facts, organic material-coupled porous carbon is a promising iodine host for the development of advanced Li–I_2 batteries. Zhang *et al.* employed three water-soluble nonionic polymers, including methyl-beta-cyclodextrin (MβCD), polyvinylpyrrolidone (PVP), and amylose corn starch (ACS), as the functional adsorption coatings of carbon-based hosts (active graphene).[89] As a result, Li–I_2 batteries using these polymer-modified iodine/carbon composites as cathodes showed enhanced electrochemical performance in terms of cycling stability and Coulombic efficiency (CE). However, the organic–inorganic composites prepared in the related follow-up studies did not show dramatic breakthroughs in battery electrochemical performance due to the lack of further systematic studies on the polymer properties. Encouragingly, with the introduction of quaternary ammonium groups into the polymer structure, the polymer-based Zn–I_2 cell has achieved over 17 000 cycles with 100% capacity retention due to the strong electrostatic interaction between the quaternary ammonium groups and the iodine species.[27] To this end, it is desirable to combine rationally designed polymers and carbon materials for realizing high-capacity, high-rate, and high-stability Li–I_2 batteries.

Altering the form in which iodine is present in carbon-based entities is another path to improvement. In this context, polyvinylpyrrolidone complexed iodine (PVP–I) (Fig. 4e) and inorganic LiI (Fig. 4f) are frequently used as iodine sources, while 2D few-layer iodine nanosheets (Fig. 4g) are rarely reported due to their additional preparation process, including sonication, and centrifugation[103,107,108] In detail, the advantages of PVP–I are as follows: (1) the heteroatoms (oxygen and nitrogen) in the PVP chain enable the PVP to complex with iodine, thus reducing the solubility of iodine in electrolyte and improving its thermal stability;[109] (2) PVP can bind strongly to carbon surfaces in aqueous solutions as it provides a strong thermodynamic driving force that eliminates the hydrophobic interface.[104] Benefiting from these, the Li–I_2 battery with nitrogen-containing porous carbon plate arrays grown on carbon fiber cloth as the host and PVP–I as the iodine source, can be cycled 3000 times at 1C with a capacity retention of 79.7%. But a thought-provoking issue is that the iodine content in commercial PVP–I is usually lower than 20 wt%, which greatly reduces the actual energy density of the whole battery and makes PVP–I unsuitable for real applications. On this basis, Zhang *et al.* directly used the iodine@activated graphene composites as the matrix, while employing PVP as the coating.[89] Despite achieving a 49 wt% iodine content in the composite, the performance for the as-prepared Li–I_2 battery dropped drastically (500 cycles with a capacity retention of 90.1% at 1C). This suggests that the ability of PVP to restrict iodine species is not as strong as expected. All in all, PVP–I, as an iodine source, may be somewhat limited in a practical sense due to its low iodine content and moderate interaction with iodine species.

On the other hand, LiI is also used as a replacement for iodine. One of the main reasons is that LiI is the discharge product that reduces cathode volume expansion (about 49% increase in volume from I_2 to LiI) during cycling to forestall pulverization of the active components.[107] Also, with LiI as an iodine source, the resulting Li–I_2 battery is therefore compatible with Li-free metal electrodes, ensuring the battery's safety. To be noted, the theoretical capacity drops but is only about 5% when I_2 (211 mA h g^{-1}) is replaced with LiI (200 mA h g^{-1}) as the iodine resource. Given all these facts, Wu *et al.* first demonstrated the performance of the Li–I_2 cell with LiI confined in meso–micro porous carbon polyhedrons as the cathode (Fig. 4f),[107] which displayed a cycling life of 800 times at 2C with a capacity retention of 83.2%. Particularly, Li *et al.* further combined LiI with nitrogen and phosphorus co-doped carbon cloth, enabling the as-assembled Li–I_2 cell to be cycled more than 2000 times with an excellent capacity retention of 95.8%.[97] Hence, LiI can be regarded as a promising alternative to thermally labile iodine.

As compared to PVP–I and LiI which have a role in mitigating iodine species shuttling, two-dimensional few-layer iodine nanosheets (FLINs) are primarily used to obtain high-rate iodine-based batteries (Fig. 4g). This is because FLINs are ultrathin and have a large aspect ratio, making them highly uniform when dispersed in carbon-based materials. Since iodine is equivalent to active sites in carbon materials capable of desorbing/adsorbing zinc ions, FLINs will therefore not only provide sufficient active sites but also shorten the ion paths, thereby effectively enhancing the rate capability of batteries.[108,110] Qian and her team reported the application of FLINs in Li–I_2 batteries for the first time, which showed a long life of 1000 cycles with a capacity retention of 93.2% at 9.5C. Even at a high current density of ∼38C, the FLINs-based cell was capable of exhibiting a reversible capacity of ∼96 mA h g^{-1}, which fully demonstrated the feasibility of FLINs in achieving fast cathode kinetics. In consideration of the excellent rate capability and feasible preparation procedure of FLINs, more extensive studies on FLINs in MIBs as the iodine source are desirable in the future.

2.1.1.2 Other iodine hosts (titanium carbonitrides, MXenes, and organic polymer/salts). Apart from carbon-based materials, high-performance Li–I_2 batteries have also been constructed using other iodine hosts, including titanium carbonitrides, MXenes, and organic polymers/salts. Among them, titanium carbonitrides with ceramic properties are highly stable and corrosion-resistant, making them an interesting class of electrically conducting materials, which were then introduced by Anju *et al.* into Li–I_2 batteries as an iodine host (Fig. 5a).[111] By adjusting the C/N ratio, they found that $TiC_{0.7}N_{0.3}$ possessed a work function of 4.85 eV that is close to the potential of the redox couple (I_3^-/I^-, 4.9 eV), thus considering that $TiC_{0.7}N_{0.3}$ has favorable adsorption characteristics for iodine species. Density functional theory (DFT) calculations also demonstrated the favorable interaction between $TiC_{0.7}N_{0.3}$ and the iodine/iodide couple, which may originate from the overlap of the d-band of Ti and the p-orbital of iodine. As a result, the as-prepared Li–I_2 battery exhibited an outstanding performance over 7000 cycles with negligible capacity decay. However, follow-up research on this type of material is lacking. In addition to titanium carbide, a flexible hydrogen-bonded organic framework (HOF) linked to $Ti_3C_2T_x$ MXene complexes (HOF@$Ti_3C_2T_x$) has been recently reported to serve as the iodine host. However, the performance of the I_2/HOF@$Ti_3C_2T_x$ cathode was less than satisfactory, showing a short lifetime of 300 cycles corresponding to a capacity retention of 79.1%. Despite this, from this single report, one cannot yet conclude that such materials are not suitable for MIBs, as Nb_2CT_x MXene has shown excellent performance (23 000 cycles with 80% capacity retention) in a Zn–I_2 battery.[83] The exploration of organic polymer materials is more extensive compared to titanium carbonitrides and MXenes (Fig. 5b).[80] But these attempts have been restricted to a handful of well-known polymers, such as starch, PVP, and β-cyclodextrin, lacking a systematic study of polymers. In this connection, it is not surprising that Li–I_2 batteries based on polymers exhibited sub-optimal performance.[80] The utilization of organic iodized salts as alternatives to organic polymer materials may be a potentially viable solution for several reasons: (1) the compact structures of organic iodized salts allow them to load more iodine-active substances and (2) organic iodized salts inherit the advantages of polymer materials, including lightweight, chemical abundance, sustainability, cost-effectiveness, tunable structure, and abundant active sites (Fig. 5c and d). Recently, Li *et al.* employed methylamine hydroiodide with an iodine content of 80 wt% for the first time as the cathode for Li–I_2 batteries, achieving an ultra-high capacity retention of 98.3% over 10 000 cycles at 5C (Fig. 5e);

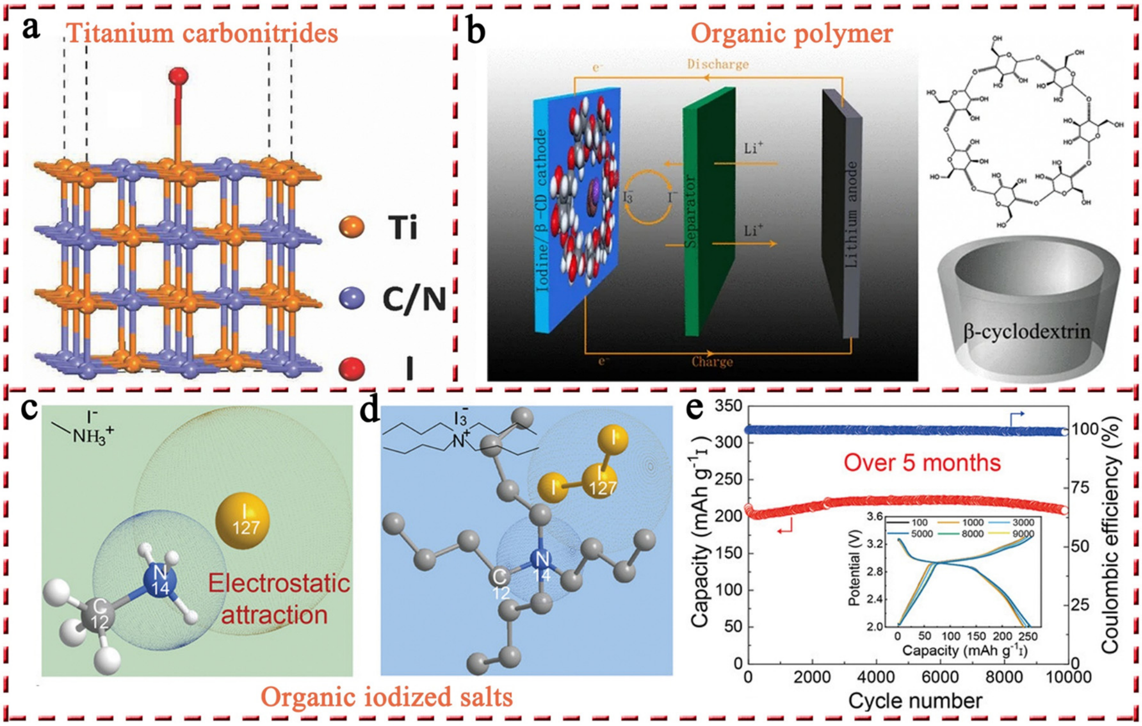

Fig. 5 (a) The relaxed slab of (100) (titanium carbonitride) 2D surface unit cell with iodine extended periodically along *x* and *y* directions. Reprinted with permission from ref. 111. Copyright 2017 Wiley. (b) Schematic illustration of a Li–I_2 battery with the iodine@β-cyclodextrin composite cathode. Reprinted with permission from ref. 80. Copyright 2018 Springer Nature. Schematic showing the electrostatic interactions between iodine species and (c) methylamine, and (d) tetrabutylammonium. (e) Long-term stability of Li–I_2 cell with the methylamine hydroiodide cathode at 5C. Inset: Corresponding voltage profiles of the cell from the 100th to the 10 000th cycle. Reprinted with permission from ref. 53. Copyright 2022 Wiley.

this can be attributed to the robust chemical interaction between iodides and the positively charged organic group ($-NH_3^+$).[53] This result fully demonstrates the great potential of organic iodized salts in Li–I_2 batteries, although the development of organic iodized salts for MIBs is still in its infancy. Some key issues still remain to be investigated, such as the structure–activity relationship between the functional group, chain length, and spatial structure of organic iodide salts and the electrochemical properties of cells, as well as the compatibility of organic iodide salts with electrolytes. The rapid advancement of research on organic iodized salts is expected to realize high-capacity, high-stability, and low-cost MIBs.

2.1.2 Interlayers. In general, the shuttle effect in MIBs originates from two factors (*i.e.*, dissolution and diffusion of polyiodide/iodine), while the construction of iodine host materials can effectively solve these issues. Nevertheless, the high solubility of iodine species in the electrolyte facilitates rapid cathode chemistry *via* a liquid-phase reaction mechanism, that is, selective regulation that allows the dissolution but resists the diffusion behavior of polyiodide could serve as an ideal approach to realize high-rate Li–I_2 batteries. Following this concept, researchers have been enthusiastic about constructing functional interlayers between the cathode and separator (Fig. 6a).[23,43,112] Table 3 presents relevant battery information and performance data regarding the interlayer section for Li–I_2 batteries. Ideally, the interlayer materials shall be capable of chemically or physically interacting with the iodine species to curb the diffusion of polyiodide. Additionally, high electronic conductivity and high porosity of materials are also required for creating a larger number of active sites to adsorb dissolved polyiodide, catalyze the charge/discharge electrochemistry of the iodine redox couple, and accelerate Li^+ transfer.[113] In these cases, Li–I_2 batteries equipped with functional interlayers will generate pseudocapacitance for energy storage due to the accompanying chemical and physical adsorption–desorption of iodine species on the interlayer surface (see Fig. 6b for the characteristic cyclic voltammetry (CV) curves). Considering the pseudo-capacitive contribution and the fast liquid-phase conversion of iodine species, Li–I_2 batteries with interlayers could effectively enhance energy storage capacity and power density.

Commonly, carbon matrices can assume the role of functional interlayers in Li–I_2 cells. For example, Wu *et al.* employed carbon nanotubes (CNTs) as interlayers, which demonstrated a high capacity of 100 mA h g^{-1} and a CE value of $\sim$100% after 5000 cycles at an astonishing rate of 100C.[114] Moreover, nitrogen-doped graphene nanosheets and honeycomb-like carbon materials from coffee extract were also reported as functional interlayers.[43,113] Benefiting from the successful incorporation of electrochemical conversion reaction and pseudo-capacitive process into Li–I_2 batteries, the as-fabricated batteries achieved a high power density output ($\geq$50C) and an ultra-long cycling life ($\geq$4000 cycles) (Fig. 6c). In addition to the carbon-based interlayers, the B_2O_3@CNT composite interlayer was also investigated (Fig. 6d).[115] Coincidentally, the as-prepared Li–I_2 battery

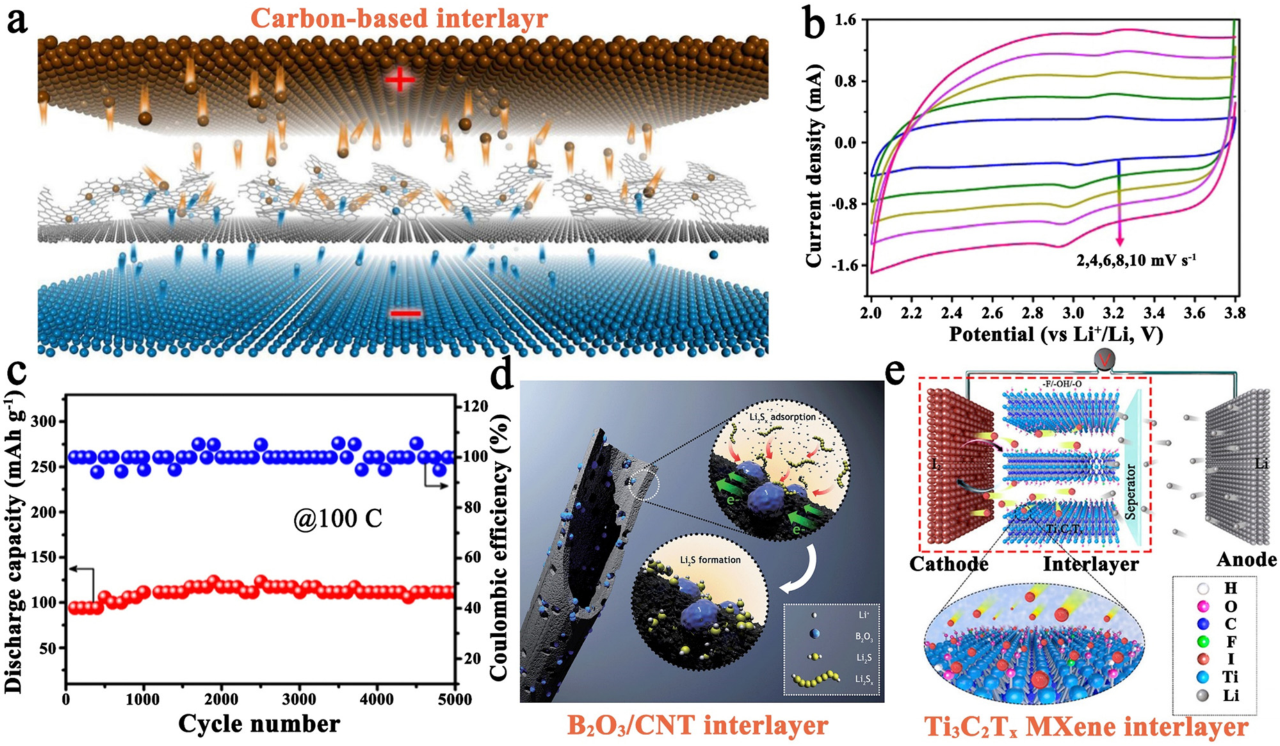

Fig. 6 (a) Schematic construction of a pseudo-capacitive Li–I_2 battery with a carbon-based interlayer. (b) Characteristic CV curves at various scan rates, and (c) long-term cycling performance (100C) of a Li–I_2 battery with the carbon-based interlayer. Reprinted with permission from ref. 43. Copyright 2018 Elsevier. (d) Schematic diagram for the working mechanism of B_2O_3 nanocrystal-modified CNT. Reprinted with permission from ref. 115. Copyright 2016 Royal Society of Chemistry. (e) Schematic illustration for the reaction mechanism of a Li–I_2 battery with the MXene interlayer. Reprinted with permission from ref. 23. Copyright 2020 American Chemical Society.

showed a high reversible capacity of 140.7 mA h g^{-1} after 5000 cycles at 100C. Such excellent cycling stability of Li–I_2 cells is mainly attributed to the strong interaction between the ultra-small B_2O_3 nanocrystals and iodine species. Despite this, the iodine content in this cell is relatively low ($\sim$1 mg cm^{-2}), leading to the significantly restricted energy density of the cell. Therefore, Sun *et al.* proposed to employ $Ti_3C_2T_x$ MXene as an interlayer to implement a Li–I_2 cell with high iodine loading because of the unique hexagonal lattice symmetry, surface chemistry, and metallic nature of MXene materials (Fig. 6e).[23] As a result, the $Ti_3C_2T_x$-based battery can be cycled stably for over 1000 cycles at 2C with a cathode loading mass of 5.2 mg cm^{-2} (the actual iodine loading is about 2.5 mg cm^{-2}). However, the performance of the cell under this condition is much worse than that of the battery with low iodine loading. More data and experiments are needed to establish a conclusive link between iodine loading and battery performance for this specific design.

All in all, constructing interlayers seems to enhance the performance of high-rate and stable Li–I_2 batteries compared to the iodine hosts discussed above, indicating a positive effect of interlayers on battery performance. However, some problems and phenomena are worthy of consideration. (1) The introduction of interlayers actually increases the battery's inactive component, which may reduce the actual energy density and increase assembly cost. Thus, it is necessary to evaluate the pros and cons of the battery in terms of cost and performance after introducing the functional interlayers. (2) Compared with iodine host materials, there is still a lack of systematic research on interlayers. More breakthroughs for the improvement of interlayers are expected in the future. (3) The iodine host and the functional interlayer may be complementary in terms of both structure and function, that is, the iodine host can retain most of the polyiodide species well, while the functional interlayer can serve as an additional adsorption layer to prevent polyiodide diffusion, provide pseudo-capacitance, and catalyze the charge/discharge electrochemistry of the iodine redox couple. Interesting phenomena may arise by combining the iodine host and interlayer, which are worthy of further investigation.

2.1.3 Electrolyte

2.1.3.1 Conventional organic liquid electrolytes. The electrolyte is critical to battery performance as it enables batteries to efficiently build a complete and functional circuit, much like blood in the human body.[116–118] Table 4 in the section modified electrolyte for Li–I_2 batteries provides the relevant battery information and performance details. In general, the most commonly used electrolyte formulation in Li–I_2 batteries is 1 M lithium bis(trifluoromethane sulfonyl) imide (LiTFSI) with 1 wt% $LiNO_3$ in 1,3-dioxolane (DOL)/1,2-dimethoxyethane (DME) (1 : 1, v/v); this is similar to Li–S batteries due to the same problem (*i.e.*, shuttle effect) that exists in both types of batteries.[8] Particularly, the addition of $LiNO_3$ into the ether-based electrolyte will help in

Table 3 Interlayers in Li–I_2 batteries

1	2	3	4	5	6	7	8	9	10
2016	B_2O_3-modified CNT	I_2/superconducting CB	1 M $LiPF_6$ in PC/EC/DEC (1 : 4 : 5, v/v/v)	∼1	∼100	5000	—	140.7	115
2018	N-doped graphene	I_2/superconducting CB	1 M $LiPF_6$/0.1 M LiTFSI in EC/DMC (1 : 1, v/v)	∼1	100	5000	—	111.3	43
2018	CNT	I_2/super-P CB	1 M $LiPF_6$/0.1 M LiTFSI in EC/DMC (1 : 1, v/v)	1	100	5000	100	100	114
2020	Honeycomb-like carbon	I_2/superconducting CB	0.5 M LiTFSI/0.1 M $LiNO_3$ in DOL/DME (1 : 1, v/v)	∼1.1	50	4000	—	120.2	113
2020	$Ti_3C_2T_x$ MXene foam	I_2@N-doped graphene	1 M LiTFSI/0.2 M $LiNO_3$ in DOL/DME (1 : 1, v/v)	∼2.5	2	1000	78	80	23

1, year; 2, interlayer; 3, cathode; 4, electrolyte formula; 5, iodine loading (mg cm^{-2}). Evaluation of Li–I_2 cell performance: 6, current density (C, 1C = 211 mA h g^{-1}); 7, cycle number; 8, capacity retention (%); 9, reversible capacity (mA h g^{-1}_{iodine}). 10, reference. CB, carbon black; PC, propylene carbonate.

Table 4 Modified electrolytes in Li–I_2 batteries

1	2	3	4	5	6	7	8	9
2011	LiI(3-hydroxypropionitrile)$_2$ (LiI(HPN)$_2$)	I_2/LiI(HPN)$_2$	—	20 μA cm^{-2}	∼5	—	—	48
2013	Anodolyte, 1 M $LiPF_6$ in EC/DMC (3 : 7, v/v); catholyte, 0.08 M I_2/1 M KI/0.03 M LiI in aqueous solution	Super P/PVDF	—	2.5 mA cm^{-2}	100	99.6	∼207	28
2014	Anodolyte, P(EO)$_{20}$LiTFSI/PP13TFSI; catholyte, 0.2 M I_2/1 M KI in aqueous solution	Super P/PVDF	—	1 mA cm^{-2}	50	97	∼190	266
2014	Anodolyte, 1 M $LiPF_6$ in EC/DMC (3 : 7, v/v); catholyte, 0.1 M I_2/1 M KI in aqueous solution	Vertically aligned multi-walled CNT	—	2.5 mA cm^{-2}	200	∼89.8	185	125
2015	LiI(HPN)$_2$	I_2/LiI(HPN)$_2$ film paper	—	0.25 mA cm^{-2}	15	—	—	131
2016	Anodolyte, 1 M LiTFSI in EC/DMC (3 : 7, v/v); catholyte, 0.2 M I_2/2 M KI in aqueous solution	α-Fe_2O_3/fluorine-doped tin oxide coated glass	—	0.3 mA cm^{-2}	22	∼99	180	127
2019	$NaNO_3$ particles in pentaerythritol-tetraacrylate-based gel polymer electrolyte	$Ti_3C_2T_x$/carbon cloth/I_2	—	0.5	1000	85	280.5	70
2021	1 M LiTFSI/0.2 M $LiNO_3$/0.1 M LiCl in DOL/DME (1 : 1, v/v)	Ammonium methyl iodide/carbon cloth	∼1.9	∼9.5	1300	80	∼274	18
2021	U-shaped garnet $Li_{6.4}La_3Zr_{1.4}Ta_{0.6}O_{12}$ ceramic electrolyte	Molten CsI/LiI eutectic salt	∼174 (LiI)	3	2000	∼100	∼180.2	132
2022	PEO/LiTFSI (18 : 1) on the $Li_{1.5}Al_{0.5}$-$Ge_{1.5}(PO_4)_3$	I_2@KB/PEO/LiTFSI/carbon cloth	0.5	1	9000	84.1	112.9	128

1, year; 2, electrolyte formula; 3, cathode; 4, iodine loading (mg cm^{-2}). Evaluation of Li–I_2 cell performance: 5, current density (C, 1C = 211 mA h g^{-1}); 6, cycle number; 7, capacity retention (%); 8, reversible capacity (mA h g^{-1}_{iodine}). 9, reference. KB, ketjenblack; PVDF, polyvinylidene fluoride; PEO, poly(ethylene oxide); PP13TFSI, *N*-methyl-*N*-propylpiperidinium bis(trifluoromethanesulfonyl) imide.

stabilizing the anode surface and preventing electrolyte decomposition.[95,119] In their study, Zhao *et al.* employed three different electrolytes, including 1 M $LiPF_6$ in ethylene carbonate (EC)/ethyl methyl carbonate (EMC)/dimethyl carbonate (DMC) (1 : 1 : 1 by volume), 1 M LiTFSI in DOL/DME (1 : 1 by volume), and 1 M LiTFSI in DOL/DME (1 : 1 by volume) with 1 wt% $LiNO_3$ addition, to investigate the relationship between electrochemical properties of Li–I_2 batteries and electrolyte formulations (Fig. 7a).[95] As a result, the cell using 1 M LiTFSI in DOL/DME with 1 wt% $LiNO_3$ addition showed negligible self-discharge even after five days, thanks to the formation of passive films on the Li surface through the addition of $LiNO_3$ in ether solvent. Besides, a few works used tetra-ethylene glycol dimethyl ether (TEGDME) as a solvent instead of DME, but the underlying reason was not known. A plausible explanation, although, is that TEGDME is capable of effectively solubilizing and dissociating lithium salt and polyiodide due to its abundant glycolate structures.[120,121] Overall, there still remains a lack of in-depth understanding of electrolytes for Li–I_2 batteries, which are inherited more from the Li–S battery system. Nonetheless, Li *et al.* recently discovered novel two-electron redox chemistry of iodine (*i.e.*, $I^- \leftrightarrow I^0 \leftrightarrow I^+$) by adding LiCl into the DOL/DME electrolyte system, where the Cl^- ion can fully activate and stabilize the deactivated I^+ ions by forming I^+Cl^- complexes (Fig. 7b).[18] To this end, the Li–I_2 battery

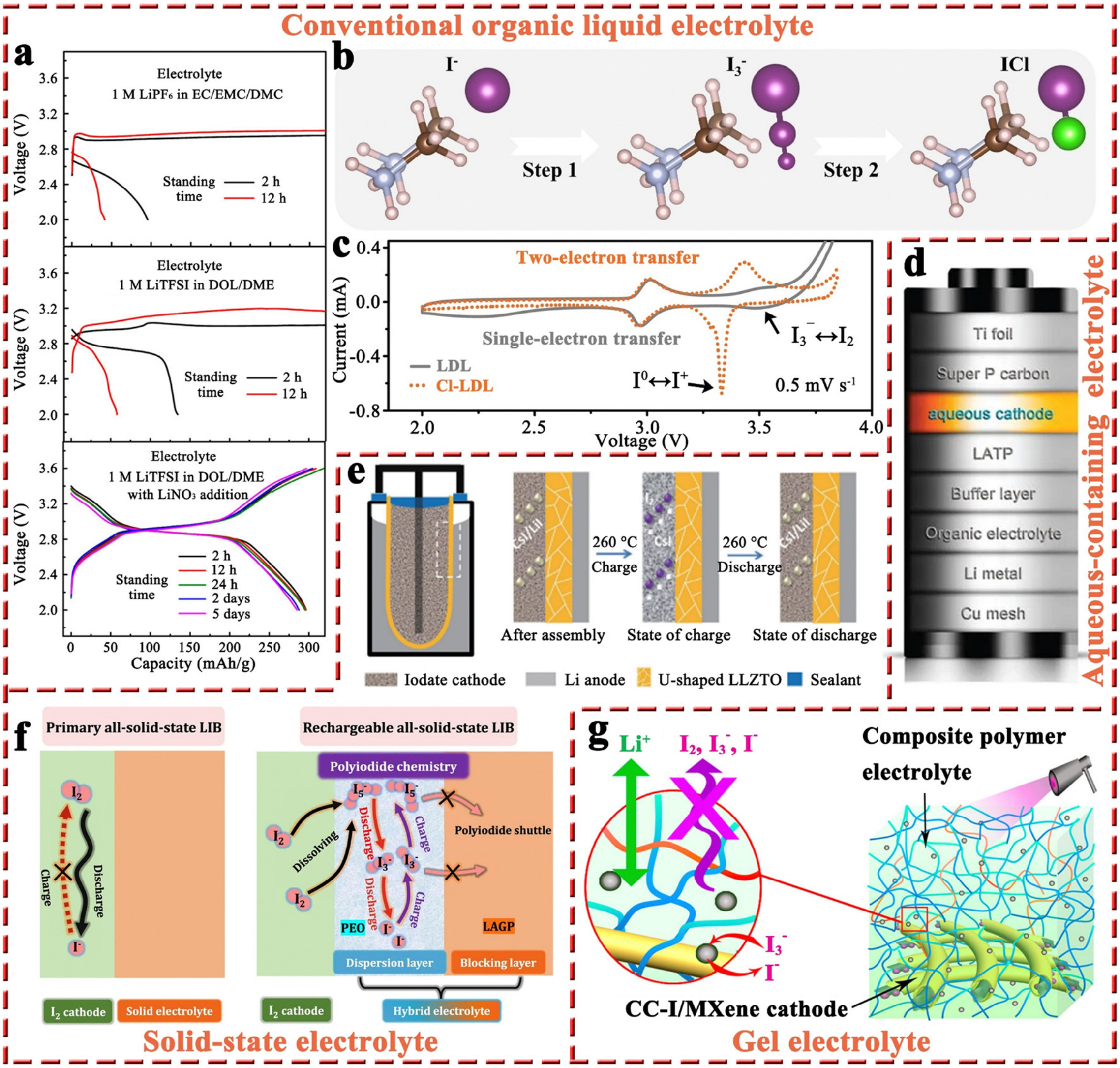

Fig. 7 (a) Discharge and charge curves of Li–I_2 batteries with the electrolytes of 1 M $LiPF_6$ in EC/EMC/DMC, 1 M LiTFSI in DOL/DME, and 1 M LiTFSI in DOL/DME with 1 wt% $LiNO_3$ addition after different standing times at 0.5C. Reprinted with permission from ref. 95. Copyright 2015 American Chemical Society. (b) The possible conversion process from I^- to I^+. (c) CV profiles of Li–I_2 cells with or without two-electron redox chemistry at 0.5 mV s^{-1}. Reprinted with permission from ref. 18. Copyright 2021 Wiley. (d) Schematic diagram for the composition of an aqueous Li–I_2 battery. Reprinted with permission from ref. 28. Copyright 2013 Springer Nature. (e) Schematic diagram for the structure of Li–I_2 batteries with LLZTO electrolyte and its working mechanism. Reprinted with permission from ref. 132. Copyright 2021 Springer Nature. (f) Schematic illustration for the reaction mechanism of all-solid-state Li–I_2 batteries at the cathode/electrolyte interface with or without the "confined dissolution" strategy. Reprinted with permission from ref. 128. Copyright 2022 Springer Nature. (g) Schematic compositions for the MXene-wrapped carbon cloth–iodine cathode and composite polymer electrolyte. Reprinted with permission from ref. 70. Copyright 2019 American Chemical Society.

can double the theoretical capacity to 422 mA h g^{-1}, while obtaining a remarkable improvement in energy density of over 200%. With ammonium methyl iodide as the cathode, the as-prepared Li–I_2 battery exhibited excellent cycle stability for over 1300 cycles with a low capacity decay ratio of 20% at 2.0 A g^{-1}. This work endows Li–I_2 batteries with new vitality as they exhibit attractive energy density (1324 W h kg^{-1} based on iodine), and more achievable multi-electron reactions compared to Li–S and Li–O_2 batteries. However, in such a system, it is puzzling that the redox peaks ascribed to the $I^0 \leftrightarrow I^+$ process coincide with those of $I_3^- \leftrightarrow I_2$ transition in conventional Li–I_2 batteries, although the intensity of the former peak is much higher (Fig. 7c). One possible reason is that the $I^0 \leftrightarrow I^+$ process actually also occurs in conventional Li–I_2 batteries without the use of LiCl-containing electrolyte. Of course, this urgently needs to be further clarified in future work.

2.1.3.2 Organic/aqueous mixed electrolytes. As compared to organic electrolytes, aqueous solutions generally have high ionic conductivity and can lead to fast redox reactions in electrochemical cells. Additionally, the high solubility of the I_3^-/I^- (over 11 mol L^{-1} with a lithium salt) redox couple in aqueous solution also ensures that Li–I_2 batteries can deliver superior energy density.[122] Furthermore, the electron-transfer rate for the I_3^- reduction reaction in an aqueous solution is superior to that in organic mediums, such as acetonitrile, dimethyl sulfoxide, *N,N*-dimethylformamide, and propylene carbonate (PC).[123–125] Therefore, Byon's group proposed the concept of a Li–I_2 battery with an aqueous cathode. As shown in Fig. 7d, the aqueous Li–I_2 battery consists of a Li composite anode (*i.e.*, Cu mesh/Li metal/organic electrolyte/buffer layer), a ceramic separator (Li_2O–Al_2O_3–TiO_2–P_2O_5, LATP), an aqueous cathode, and a current collector (*i.e.*, super P carbon/Ti foil).[28] The as-prepared Li–I_2 cell showed that the primary redox reactions occur in the potential region of 3.5–3.7 V with about 100 cycles. Furthermore, they employed vertically aligned carbon nanotubes (VACNT) instead of super P/polyvinylidene fluoride as the current collector.[125] Because the binder-free VACNTs eliminated unnecessary mass and prevented parasitic corrosive reactions arising from polymer binders, the Li–I_2 cell exhibited improved cycling performance over 200 cycles with negligible capacity decline. In addition, stemming from the rise of the "all-in-one" concept (*i.e.*, the integrated power system with energy conversion and storage functions),[126] they also demonstrated a self-charging aqueous Li–I_2 cell using a hematite electrode, which enables a facile charging process with the aid of harnessed photoenergy.[127] However, the resulting battery exhibited a very short lifespan of about 30 cycles.

As a whole, aqueous Li–I_2 batteries are still in the conceptual stage and confronted with a plenty of difficulties: (1) a complex battery structure is necessary to match the Li anode with the aqueous cathode. Whereas this not only increases battery costs and reduces battery energy density dramatically but also shortens battery life due to possible breakage of battery components during cycling and (2) given the introduction of aqueous electrolyte, the inherent safety problems associated with the metal anode are also more worrisome. Therefore, it is essential to assess the costs and benefits of aqueous Li–I_2 batteries carefully in future research to ensure their practical feasibility.

2.1.3.3 Solid-state electrolytes. The utilization of non-flammable solid-state electrolytes can effectively improve the inherent safety of batteries, addressing concerns such as leakage, fire, and explosion commonly faced by liquid electrolytes.[128–130] The primary all-solid-state Li–I_2 battery was commercialized in 1972 to serve as the power source for cardiac pacemakers.[26] Nevertheless, it can barely be recharged due to the poor Li-ion conductivity of LiI solid-state electrolyte and its continuous increase in thickness during discharge.[47,48,131] Thanks to the vigorous development of solid-state electrolytes in battery systems (*e.g.*, Li-ion batteries), Sun *et al.* introduced a U-shaped garnet $Li_{6.4}La_3Zr_{1.4}Ta_{0.6}O_{12}$ (LLZTO) ceramic electrolyte into Li–I_2 batteries.[132] As shown in Fig. 7e, the battery comprises a molten lithium anode, LLZTO electrolyte, and a molten CsI/LiI eutectic salt (CLES) cathode with an operating temperature of 260 °C. During the charge/discharge process, the CLES cathode undergoes a highly reversible conversion between LiI and I_2, while the Li anode is capable of exhibiting ultra-high stability due to its liquid form. Notably, the addition of CsI significantly reduces the melting point of LiI, allowing the cathode to form a liquid–solid interface with the LLZTO electrolyte, thereby maintaining good interfacial contact and low interfacial impedance. Given that the LLZTO electrolyte can also effectively separate the Li anode from the eutectic iodate cathode, the as-fabricated Li–I_2 battery possessed a long-term lifetime of 2000 cycles with a negligible capacity decay at 3C, even with a LiI loading of 593 mg. However, this battery system requires an ultra-high operating temperature (260 °C) to maintain the melting characteristics of the anode and cathode, as well as the high ionic conductivity of LLZTO, which severely limits its application range. In response to this limitation, Cheng *et al.* proposed a "confined dissolution" strategy, that is, polyethylene oxide (PEO) was introduced into the iodine cathode as a dispersion layer to facilitate the dissolution of polyiodide, while adopting a single lithium-ion conductor $Li_{1.5}Al_{0.5}Ge_{1.5}(PO_4)_3$ (LAGP) as a barrier layer to effectively avoid the shuttle effect of polyiodide (Fig. 7f).[128] Benefiting from the utilization of the PEO dispersion layer with well-dissolved polyiodide, the all-solid-state Li–I_2 battery can operate at 60 °C with a high specific capacity of 202 mA h g^{-1}. Meanwhile, the PEO dispersion layer also had a low Young's modulus, which could lead to close contact between the LAGP and I_2 cathode and facilitate fast Li-ion transport within the cell. On this basis, the battery exhibited an 84.1% capacity retention over 9000 cycles at 1C, which opens a new avenue for the development of rechargeable all-solid-state Li–I_2 batteries.

Overall, the incompatibility between the solid iodine cathode and solid-state electrolyte has limited the development of all-solid-state Li–I_2 batteries due to their sluggish reaction kinetics, low capacity, and poor rechargeability. The use of a molten iodine cathode and the "confined dissolution" strategy could greatly solve this fundamental problem. Furthermore, given the intrinsic safety and strong blocking ability for polyiodide, solid-state electrolytes may be the cornerstone for the rapid development of Li–I_2 batteries in the future.

2.1.3.4 *Gel electrolytes.* Similar to solid-state electrolytes, the aim of using gel electrolytes is to replace liquid electrolytes, thus improving battery safety and restraining the diffusion of dissolved iodine species. In particular, gel electrolytes have higher ionic conductivity at ambient temperature and a more stable electrode/electrolyte interface compared to solid-state electrolytes.[70] To this end, Tang *et al.* developed a flexible quasi-solid-state Li–I_2 battery, which integrates a composite polymer electrolyte (CPE), composed of catalytic $NaNO_3$ particles dispersed in a pentaerythritol-tetraacrylate-based (PETEA-based) gel, and a $Ti_3C_2T_x$ MXene-wrapped carbon cloth–iodine (CC–I/MXene) cathode (Fig. 7g).[70] As a result, the as-prepared Li–I_2 quasi-solid-state battery exhibited superior long-term cycling stability with 85% capacity retention after 1000 cycles at 0.5C. This can be attributed to the abundant surface functional groups present in $Ti_3C_2T_x$ MXene sheets, which effectively confine the iodine species within the cathode. Meanwhile, the CPE can greatly block the diffusion of iodine species and stabilize the Li anode without dendrite growth. On the other hand, the addition of $NaNO_3$ particles into PETEA-based polymer matrix could enhance the conversion kinetics of iodine species. Because the NO_3^* radical generated by the oxidation of NO_3^- can act as a reaction intermediate and is prone to be consumed instantly by I_3^- as described in the following equation: $2NO_3^* + 2I_3^- \rightarrow 2NO_3^- + 3I_2$.[133] In this regard, the $LiNO_3$ additive in liquid electrolyte may play a dual role of inhibiting dendrite growth and promoting iodine/iodide conversion. Owing to the excellent mechanical properties (strength, flexibility, *etc.*) of gel electrolytes, the as-assembled quasi-solid-state battery also showed promising application prospects in flexible electronic devices. Nonetheless, high levels of liquid plasticizers, such as EC, DMC, DME, and TEGDME, are inevitably required to achieve a satisfactory ion conductivity value ($>10^{-4}$ S cm^{-1} at 25 °C) in gel electrolytes, which usually results in a poor thermal stability and safety hazard during thermal runaway.[134] At the same time, there is a lack of systematic research on gel electrolytes in Li–I_2 batteries. Therefore, there is an urgent need to optimize the composition and structure of gel polymers in Li–I_2 batteries for achieving better performance and extending the range of applications for this type of battery.

2.1.4 Modified anodes. The modified anode section of Li–I_2 battery in Table 5 shows relevant battery information and performance. It is well known that Li anodes often suffer from several challenges, including the formation of detrimental Li dendrites, electrode volume fluctuation electroplating/stripping, and an unstable solid electrolyte interphase (SEI), all of which have a significantly negative impact on battery performance.[135,136] Another problem affecting the lithium anode in Li–I_2 batteries is related to the shuttle effect of polyiodide, as Liu *et al.* revealed that the metallic Li (100, 110) surface is very active in capturing and facilitating the dissociation of I_2 molecules (Fig. 8a and b).[137] When the iodine coverage on the Li anode surface is less than 12.5%, the dissociated iodine atoms will not destroy the anode surface. With the coverage increasing to 100%, a thin LiI layer forms but it can be exfoliated from the Li surface, resulting in an irreversible loss of active materials. Notably, $LiNO_3$ additives can effectively protect Li anodes from iodine species. O and N atoms generated from nitrate decomposition can form a Li–N–O layer between the Li metal and the topmost LiI layer, thereby cutting off the direct interaction between I_2 and metallic Li. Therefore, the addition of $LiNO_3$ into the DOL/DME system can be used as a common strategy to protect the Li anode from polyiodide and dendrite growth due to the formation of a passivation layer on the Li anode. Besides, constructing a robust passivation layer on the surface of Li anode may be a critical factor in enhancing the performance of Li–I_2 batteries. To this end, Ren *et al.* proposed an electrodeposition strategy for pre-passivating Li anodes, *i.e.*, construction of a Li–In alloy layer on the Li surface during battery charging.[138] This layer allows for facile Li storage and Li^+ transport, and is highly inertial to iodine and polyiodide, thereby shielding the Li anode from the side reactions. Simultaneously, they also integrated a layered graphene paper (LGP) as the anode interlayer onto the Li-indium (In) alloy layer to stabilize the as-formed passivation layer and further protect the Li anode from polyiodide and dendrites (Fig. 8c). As a result, the as-prepared Li-polyiodide semi-liquid battery demonstrated a reasonable average CE of ∼90% after 100 cycles with an average decay rate of 0.11% at 1.5C. However, the aggressive volume change during plating/stripping in this system can cause internal stress fluctuations resulting in a floating interface, thereby causing the fragmentation of the SEI layer. Thus, Li *et al.* fabricated a 3D stable Li metal anode by loading molten lithium into carbon cloth doped with nitrogen and phosphorus.[136] Since the N,P co-doping introduced on the carbon cloth greatly improves the lithiophilicity of the carbon cloth, molten lithium can be loaded on the carbon cloth uniformly, which is beneficial for reversible Li stripping and electroplating (Fig. 8d). Impressively, the Li–I_2 battery showed a capacity retention of around 100% over 4000 cycles at 10C. Despite recent advancements, the issue of low iodine loading (1–2 mg cm^{-2}) remains a significant challenge for Li–I_2 batteries. Thus, Giammona *et al.* proposed an innovative

Table 5 Modified anodes in Li–I_2 batteries

1	2	3	4	5	6	7	8	9	10	11
2017	Passivated Li by InI_3/layered graphene paper	1 M LiTFSI/1 wt% $LiNO_3$/1 M LiI_3 in DOL/DME (1 : 1, v/v)	Carbon cloth	—	—	1.5	100	89	∼80	138
2019	Molten Li in N,P co-doped carbon cloth	1 M LiTFSI/1 wt% $LiNO_3$ DOL/DME (1 : 1, v/v)	LiI/porous doped carbon	3 (—)	600	10	4000	99	197	136

1, year; 2, anode; 3, electrolyte formula; 4, cathode. Evaluation of Li‖Li cell performance: 5, current density (mA cm^{-2}) and areal capacity (mA h cm^{-2}); 6, cycle time (h). Evaluation of Li–I_2 cell performance: 7, current density (C, 1C = 211 mA h g^{-1}); 8, cycle number; 9, capacity retention (%); 10, reversible capacity (mA h $g^{-1}_{\text{iodine or LiI}}$). 11, reference.

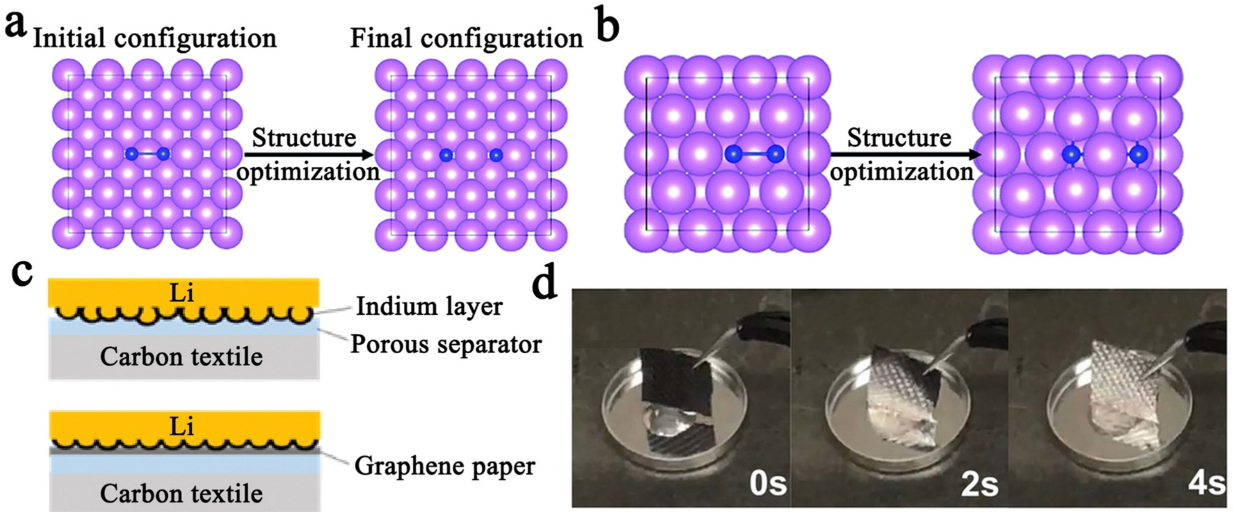

Fig. 8 Initial and optimized atomistic configurations of I_2 adsorption on the top sites of (a) (100) surface, and (b) (110) surface of Li. The violet spheres stand for Li atoms, while the blue spheres are I atoms. Reprinted with permission from ref. 137. Copyright 2018 Royal Society of Chemistry. (c) Graphs showing the combined effect of a pre-deposited indium layer with the graphene paper. Reprinted with permission from ref. 138. Copyright 2017 Elsevier. (d) Time-lapse images of molten lithium immersed into the N,P co-doped carbon cloth. Reprinted with permission from ref. 136.

solution by introducing oxygen gas into the cell, which dramatically increased the iodine loading to 10 mg cm^{-2} in Li–I_2 batteries.[139] Concretely, oxygen gas can react with iodine species and NO_3^- ($I_3^- + 3O_2 + 2e^- \rightarrow 2IO_3^- + I^- + 8.74$ eV; $I_2 + 3O_2 + 2e^- \rightarrow 2IO_3^- + 8.50$ eV; $2I_2 + 3O_2 + 2NO_3^- + 8e^- \rightarrow 4IO_3^- + 2N^{3-} + 9.45$ eV), resulting in the formation of a robust SEI layer consisting of $LiIO_3$ and Li_3N on the lithium anode surface. This SEI layer enables fast ion transfer, suppresses dendritic growth, and mitigates the shuttle effect, allowing Li–I_2 cells with an iodine loading of 10 mg cm^{-2} to be cycled up to 50 times at 1 mA cm^{-2}. This advancement is potentially important for facilitating the practical application of Li–I_2 batteries. Notably, the utilization of solid-state/gel electrolytes could be a useful approach for suppressing dendrite growth and polyiodide shuttling as described previously.

To sum up, the strategies proposed in Li–I_2 batteries to protect the Li anode can be mainly classified into the following four categories: (1) adding $LiNO_3$ to the electrolyte that can protect the Li anode; (2) using solid-state electrolytes based on the "molten electrode" or "confined dissolution" strategy, and gel electrolytes; (3) constructing a passivation layer (*i.e.*, artificial SEI); and (4) preparing a 3D-stabilized Li metal anode. It is worth noting that these strategies can all be found in Li-based batteries. We therefore predict that lithium-based batteries will experience new breakthrough once the bespoke lithium anode problems are solved.

2.2 Sodium–iodine batteries

Li–I_2 batteries possess the highest energy density among various MIBs due to their high voltage window. However, the scarcity, uneven distribution, and exorbitant price of lithium resources greatly limit the extensive utilization of Li–I_2 batteries, especially in the presence of numerous other Li-based batteries. Thus, it is crucial to develop MIBs based on earth-abundant metal anodes. As a high-performance anode, Na has become the focus of researchers due to its highly abundant natural sources (2.74% in the Earth's crust), high theoretical specific capacity (1166 mA h g^{-1}), and low potential (−2.71 V *vs.* SHE).[140–142] Given this, a promising path to expand the application of MIBs is by replacing Li with Na as the anode. Tables 6 and 7 in the section on Na–I_2 batteries provides the relevant battery information and performance. Research on Na–I_2 batteries began with medium-temperature molten Na-based batteries,[54,143] as similar high-temperature Na-S battery systems have been put into commercial production and tested for grid storage in Japan, France, and the United States.[144] Ngersoll *et al.* demonstrated the prototype of a Na–I_2 battery based on NaSICON ceramics and inorganic NaI/$AlCl_3$-based catholyte.[54] Zhu *et al.* further conducted a theoretical study on an aqueous Na–I_2 system with a molten sodium anode under an operating temperature of 120 °C (Fig. 9a).[143] Moreover, Holzapfel *et al.* realized a rechargeable molten-sodium system at approximately 100 °C using aqueous iodine/iodide solution as the catholyte and sodium-ion conductive NaSICON ($Na_3Zr_2Si_{2.3}P_{0.7}O_{11.85}$) as the solid-state electrolyte.[54] Despite this, room-temperature Na–I_2 batteries are still eagerly pursued because of their less demanding and safer operation compared to the high-temperature cell systems.[145]

Up to now, the commonly used electrolytes for realizing room temperature Na–I_2 batteries are focused on 1 M $NaClO_4$ in carbonate electrolytes (*i.e.*, propylene carbonate, ethylene carbonate, and dimethyl carbonate). In this case, Gong *et al.* first demonstrated a room-temperature rechargeable Na–I_2 battery by employing free-standing iodine quantum dots (IQDs)-decorated reduced graphene oxide (IQDs@RGO) as the cathode (Fig. 9b).[55] Given that porous RGO acts as a conductive network, the loaded IQDs will favor intercalation and shorten the diffusion distance of Na^+ ions. The RGO can also provide strong adsorption, restraining the free diffusion of iodine species. As a

Table 6 Iodine host materials in Na–I_2 batteries

1	2	3	4	5	6	7	8	9	10
2016	Iodine quantum dots decorated RGO	1 M $NaClO_4$ in EC/DEC (1 : 1, v/v)	26	∼0.8	∼0.5	500	∼82	141	55
2017	I_2/3D bio-foam derives from *C. Barometz* spores	1 M $NaClO_4$ in PC	30–40	∼1–1.5	6/2	500	91	—	96
2018	PVP–I‖N-doped hollow carbon sphere–I_2	1 M $NaClO_4$ in PC	∼35	—	4	400	73	—	103
2020	CNT/GO/few-layer iodine nanosheets	1 M $NaClO_4$ in EC/DEC (1 : 1, v/v)	∼44	—	∼24	5000	—	84.5	110
2020	Fe_2–O_8–PcCu/I_2 phthalocyanine copper COF	1 M $NaClO_4$ in EC/DEC (1 : 1, v/v)	40	—	∼7	3200	—	150	24
2022	I_2/single primitive polypyrrole	1 M $NaClO_4$ in EC/DEC (1 : 1, v/v)	48	—	1	400	∼52 (from 10th cycle)	∼70	147
2022	I_2/hydrogen bonded organic framework@$Ti_3C_2T_x$	1.0 M $NaClO_4$/5.0% FEC in EC/DEC (1 : 1, v/v)	44.3	∼0.93	0.2	200	∼100	207.6	146
2023	I_2@γ-Mo_2N/mNC	1.0 M $NaClO_4$/5.0% FEC in EC/DEC (1 : 1, v/v)	25	0.7–1.5	3.55	800	—	213.5	148

1, year; 2, cathode; 3, electrolyte formula; 4, the mass loading of iodine at the cathode (wt%); 5, the area loading of iodine at the cathode (mg cm^{-2}). Evaluation of Na–I_2 cell performance: 6, current density (C, 1C = 211 mA g^{-1}); 7, cycle number; 8, capacity retention (%); 9, reversible capacity (mA h g_{iodine}^{-1}). 10, reference. RGO, reduced graphene oxide; GO, graphene oxide; COFs, covalent organic frameworks; FEC, fluoroethylene carbonate. γ-Mo_2N/mNC, N-doped hierarchical mesoporous carbon decorated with γ-Mo_2N nanoparticles.

Table 7 Modified anodes in Na–I_2 batteries

1	2	3	4	5	6	7	8	9	10	11
2019	NaI SEI	1 M $NaClO_4$ in EC/DEC with 5% FEC	I_2/active carbon cloth with iodine of ∼1.5 mg cm^{-2}	0.25 (0.75)	500	2	2200	100	110	151

1, year; 2, anode; 3, electrolyte formula; 4, cathode. Evaluation of Na‖Na cell performance: 5, current density (mA cm^{-2}) and areal capacity (mA h cm^{-2}); 6, cycle time (h). Evaluation of Na–I_2 cell performance: 7, current density (C, 1C = 211 mA h g^{-1}); 8, cycle number; 9, capacity retention (%); 10, reversible capacity (mA h $g_{iodine\ or\ LiI}^{-1}$). 11, reference. SEI, solid electrolyte interface.

result, Na–I_2 with the IQDs@RGO cathode exhibited 500 cycles at a current density of 100 mA g^{-1}. However, the preparation of iodine quantum dots also results in a low iodine content (∼26 wt%) in the material. On the other hand, Qian *et al.* reported the successful preparation of FLINs *via* a sonochemical liquid-phase exfoliation approach, which can thus increase the iodine content in the material to about 44 wt% (Fig. 9c).[110] Especially, with the loading of FLINs into the carbon nanotube-graphene oxide composite, the as-prepared Na–I_2 battery showed an outstanding rate performance of 109.5 mA h g^{-1} at a high current density of 10 A g^{-1} (Fig. 9d). Therefore, the utilization of FLINs may be more suitable for implementing high-rate MIBs. Moreover, hollow carbon spheres and HOF@$Ti_3C_2T_x$ were also investigated in Na–I_2 batteries, but their performance was consistently poor as in Li–I_2 batteries.[96,103,146] On the other hand, attempts have been made to utilize ordered porous materials synthesized through self-assembly techniques as iodine hosts in Na–I_2 batteries. For instance, Xiang *et al.* tried to employ ordered single primitive polypyrrole, poly(*m*-phenylenediamine), and polydopamine as iodine hosts but with poor performance (70 mA h g^{-1} after 400 cycles of the optimal polypyrrole/I_2 cathode at 1C).[147] This may be attributed to the excessively large pores (45 nm) of these materials, leading to inadequate confinement of iodine species. Therefore, when the pore size was reduced to 10–20 nm and γ-Mo_2N was introduced as a catalyst for iodine conversion, the self-assembled porous materials demonstrated improved battery stability and capacity (213.5 mA h g^{-1} after 800 cycles at 3.55C).[148] Notably, a novel fully conjugated phthalocyanine copper metal–organic framework (MOF) was introduced into Na–I_2 batteries as the iodine host. The presence of atomically dispersed metal centers, abundant pore structures, and an extended π-conjugation structure makes it an ideal host for iodine. As a result, Wang *et al.* investigated three fully conjugated PcCu-MOFs (*i.e.*, Fe_2–O_8–PcCu, Ni_2–O_8–PcCu, and Zn_2–O_8–PcCu) with 2, 3, 9, 10, 16, 17, 23, 24-octahydroxy phthalocyaninato copper as the building blocks and metal-bis(dihydroxy) complexes as the linkages (Fig. 9e).[24] Benefiting from the strong polarization interaction between polyiodide and conjugated Fe-O_4 centers, as well as more favorable polyiodide oxidation conversion on the Fe-O_4 centers, the Na–I_2 battery with a Fe_2–O_8–PcCu/I_2 cathode exhibited superior long-term cycling stability up to 3200 cycles at 1.5 A g^{-1}. This confirms the potential application of MOFs in MIBs.

From the perspective of sodium anodes, Na metal is unstable with carbonate electrolytes, which usually leads to the formation of a loose and fragile SEI. Meanwhile, the uneven plating/stripping behavior of Na^+ during the cycling process would greatly induce the formation of Na dendrites that deteriorate the battery's performance.[149,150] Hence, extensive efforts to stabilize metallic Na anodes are essential. As previously stated, the application of an ''artificial'' SEI layer of Li–In alloy on the Li surface will effectively minimize the side reaction and dendrite growth on Li anodes. Similarly, Tian *et al.* proposed a method of *in situ* construction of an ultrathin NaI SEI layer on the Na anode surface *via* the reaction between 2-iodopropane and Na metal (Fig. 9f).[151] The resulting Na/Na symmetrical cells can be cycled for up to 500 h, while the as-assembled Na–I_2 battery showed over 2200 cycles at 2C with an active carbon cloth@iodine cathode. However, the presence of LiI is generally believed to negatively affect the anode stability in Li–I_2 batteries. This results from its loose structure that cannot prevent the anode surface from corrosion, also, it can easily react with soluble I_2 to

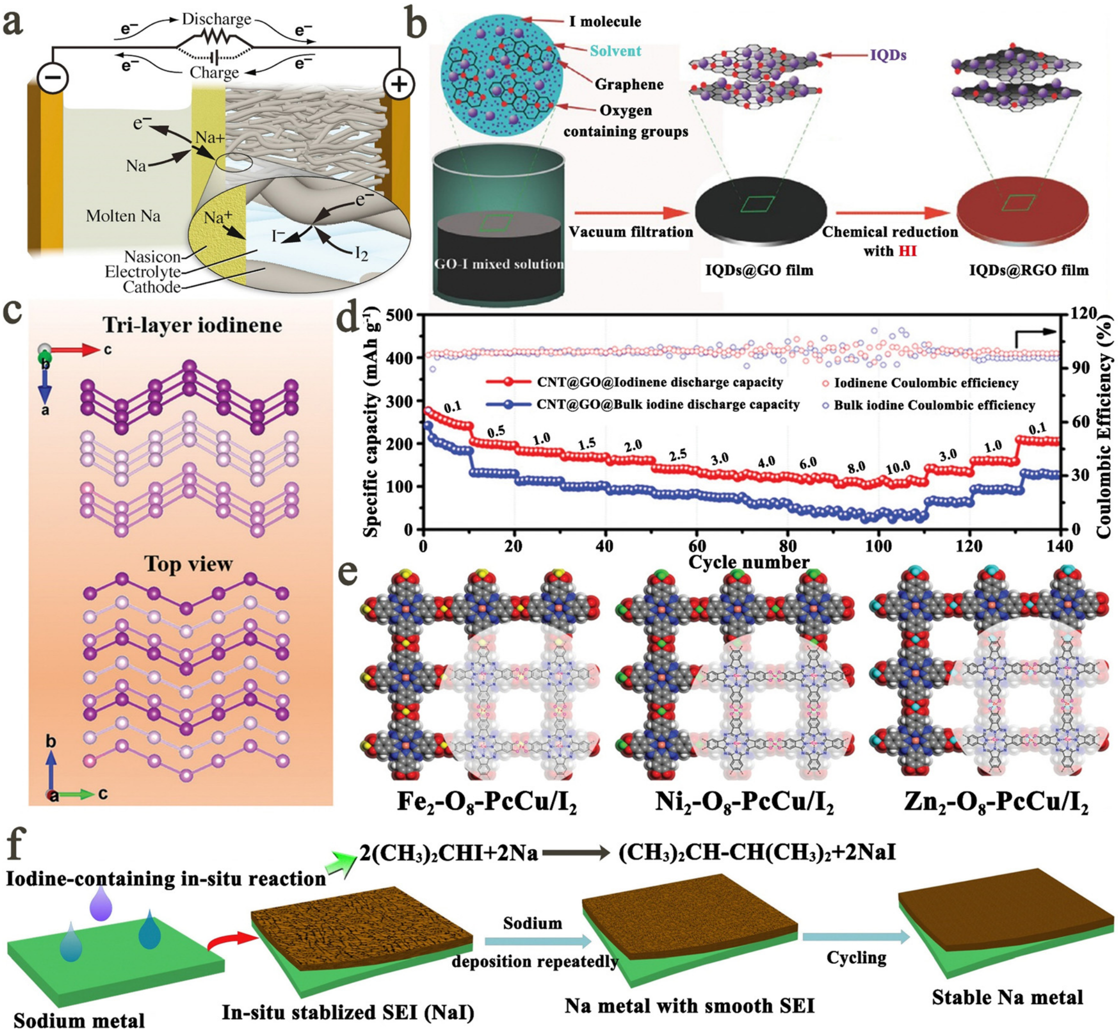

Fig. 9 (a) Schematic diagram for the structure of a high-temperature Na–I_2 secondary battery. Reprinted with permission from ref. 143. Copyright 2016 Elsevier. (b) Schematic diagram for the fabrication process of the IQDs@RGO cathode. Reprinted with permission from ref. 55. Copyright 2016 Wiley. (c) The structure of tri-layer iodine (the top and bottom parts present the front and top views, respectively). (d) Rate capabilities of Li–I batteries with bulk iodine and FLINs at various current densities from 0.1 to 10 A g^{-1}. Reprinted with permission from ref. 110. Copyright 2020 Wiley. (e) Schematic modeling and chemical structures of Fe_2–O_8–PcCu, Ni_2–O_8–PcCu, and Zn_2–O_8–PcCu. Reprinted with permission from ref. 24. Copyright 2019 Wiley. (f) Schematic illustration for *in situ* construction of an ultra-thin NaI SEI layer on the Na metal anode. Reprinted with permission from ref. 151. Copyright 2018 Elsevier.

form LiI_3.[95,137] For this case, a possible explanation is that the NaI layer in the Na–I_2 battery formed by the *in situ* reaction of 2-iodopropane with metallic Na is compact and even, which is conducive to achieving a uniform reaction between carbonate-based electrolyte and soluble iodine species, thereby improving the interfacial stability of Na anodes. In the comparative experiments performed by Tian *et al.*, the morphology of the NaI layer prepared using diethyl carbonate (DEC) with 50 mM I_2 is loose and inconsecutive, and as a result, the as-assembled battery showed poor performance. Besides, the NaI layer also exhibits a lower diffusion barrier (ionic conductivity: $\sim 3 \times 10^{-2}$ S cm^{-1}) compared to NaF (common inorganic component for dendrite inhibition in the Na-based SEI layer),[151,152] enabling high-performance Na–I_2 batteries. Therefore, achieving a uniform and dense NaI layer with high ionic conductivity could be a new approach toward a highly stable Na anode.

Compared to Li–I_2 batteries, studies on Na–I_2 batteries are few and far between. Benefiting from the commonality of iodine cathodes, however, strategies to improve iodine cathodes can be shared between both types of MIBs, as shown by the applications of FLINs in Li/Na–I_2 batteries. On the other hand, room-temperature Na–I_2 batteries typically use carbonate ester-based electrolytes derived from Na-ion batteries because of their ability to form more stable SEI films.[149] However, Tian *et al.* discovered that treating Na with an I_2-containing ether solvent can lead to the creation of a relatively dense NaI layer, which is beneficial for stabilizing the Na anode.[151] In this regard, extensive investigation into new-type electrolyte formulations for Na–I_2 batteries is required in the future. Besides, few studies have explored the issues related to the Na metal anode in Na–I_2 batteries. It is anticipated that more work will be devoted to realizing advanced Na–I_2 batteries in the future, as they exhibit advantages of high stability, low cost, and moderate energy density. Last but not least, the concept of high-temperature Na–I_2 batteries is also worth exploring, considering the successful application of high-temperature Na-S batteries.

2.3 Potassium–iodine batteries

The redox potential of K/K^+ (−2.93 V *vs.* SHE), compared to that of Na/Na^+ (−2.70 V *vs.* SHE), is closer to that of Li/Li^+ (−3.04 V *vs.* SHE) in nonaqueous electrolytes.[153] Besides, potassium reserves in the Earth's crust show a high abundance of 2.09 wt%. These advantages suggest that potassium-based batteries might have high cost-efficiency and promising energy density, thus leading to the emergence of K–I_2 batteries. Relevant battery information and performance for K–I_2 batteries can be found in Tables 8 and 9. In 2018, Lu *et al.* first reported a rechargeable K–I_2 battery by employing a free-standing I_2/carbon cloth composite cathode and a metallic K anode (Fig. 10a).[56] By combing *in situ* Raman and *ex situ* X-ray photoelectron spectroscopy studies, they confirmed a reversible conversion mechanism between I_2, KI_3, and KI species, which is similar to the one in Li–I_2 batteries. And the as-prepared K–I_2 battery showed over 500 charge/discharge cycles with a capacity retention of 71% at 100 mA g^{-1}, demonstrating the feasibility of K–I_2 batteries. Subsequently, a K–I_2 battery with a mesoporous carbon (CMK-3)/iodine cathode was also investigated, which can be cycled for 300 times at 0.17 A g^{-1} (Fig. 10b).[154] Notably, as the development of K–I_2 cells is in its initial infant stage, the cathode materials used above are commonly derived from other MIBs. Especially, on comparison with Li/Na–I_2 batteries, several issues associated with K–I_2 batteries are exposed, including short lifespan and sluggish kinetics. This could be attributed to the large potassium ion radius, as well as the highly reactive potassium metal anode. Typically, a larger ionic radius means a difficult uptake/release process of K^+ in the iodine cathode. This can also cause the iodine cathode to undergo a large volume change (about 106% increase in volume from I_2 to KI) upon potassiation and depotassiation. Inevitably, this will drive severe pulverization of iodine hosts, especially carbon-based hosts that typically rely on physical effects to capture and reutilize iodine species. Furthermore, K-metal anodes with high reactivity are prone to dendrite formation and interactions with iodine species, leading to the formation of an unstable SEI layer.[68,155,156] Given these facts, K–I_2 batteries would perform poorly compared to Li/Na–I_2 batteries. To address the above problems, Deng *et al.* employed KI as the iodine source to effectively alleviate the volume expansion of the iodine cathode.[68] Meanwhile, to avoid the possible pulverization of iodine host material, a graphene-modified separator was further adopted to alleviate the shuttle effect, which also led to a dissolution–precipitation reaction mechanism at the iodine cathode (Fig. 10c). For the electrolyte, a 7 M potassium bis(fluorosulfonyl) imide (KFSI) dissolved in EC and DEC (volume ratio 1 : 1) electrolyte was chosen. As the polyiodide dissolution can be efficiently mitigated by reducing the number of free solvent molecules in the electrolyte, it could be a useful strategy to slow down the diffusion of polyiodide by increasing the viscosity of the electrolyte (Fig. 10d). As a result, the as-prepared K–I_2 batteries can maintain a high-capacity retention of 95.5% after 550 cycles at 100 mA g^{-1}, thus representing a state-of-the-art K–I_2 battery (Fig. 10e). Nevertheless, these batteries have a shorter lifespan in comparison to Li/Na–I_2 batteries. This may be attributed to easier dendrite growth in potassium anodes, thus making potassium anode protection critical for optimal performance.[157,158] Combined with the characteristics of KI cathode and previous studies, strategies such as carbon-based, alloy, and transition metal compound anodes could be used to further improve the performance of K–I_2 batteries.[156] Overall, it is more challenging to achieve high-performance potassium–iodine batteries compared to lithium/sodium–iodine batteries, but perhaps that is what the science is about.

2.4 Zinc–iodine batteries

Aqueous zinc-ion batteries are one of the most promising sustainable energy storage technologies due to their safety, non-toxicity, and high theoretical capacity.[159–162] Especially, the aqueous Zn–I_2 battery has garnered significant attention as an ideal contender for large-scale energy storage applications. This can be ascribed to their many intrinsic merits: (1) both of zinc and iodine have high environmental tolerance. Both of them are stable in an atmospheric environment at room temperature, greatly facilitating battery assembly (*e.g.*, without the need of a glovebox) and

Table 8 Iodine host materials in K–I_2 batteries

1	2	3	4	5	6	7	8	9	10
2018	I_2/carbon cloth	0.5 M KPF_6 in EC/DEC (1 : 1, v/v)	44	4	0.1 A g^{-1}	500	71	156	56
2019	Mesoporous carbon (CMK-3)	1 M KPF_6 in PC/DEC (1 : 1, v/v)	29	—	0.17 A g^{-1}	300	—	126.3	154

1, year; 2, cathode; 3, electrolyte formula; 4, the mass loading of iodine at the cathode (wt%); 5, the area loading of iodine at the cathode (mg cm^{-2}). Evaluation of K–I_2 cell performance: 6, current density; 7, cycle number; 8, capacity retention (%); 9, reversible capacity (mA h g_{iodine}^{-1}). 10, reference.

Table 9 Modified separators in K–I_2 batteries

1	2	3	4	5	6	7	8	9	10
2021	Graphene-modified separator	KI/KB	7 M KFSI in EC/DEC electrolyte (1 : 1, v/v)	~1 (KI)	0.1 A g^{-1}	550	95.5 (form 5th cycle)	—	68

1, year; 2, separator; 3, cathode; 4, electrolyte formula; 5, iodine loading (mg cm^{-2}). Evaluation of K–I_2 cell performance: 6, current density; 7, cycle number; 8, capacity retention (%); 9, reversible capacity (mA h g_{iodine}^{-1}). 10, reference. KFSI, $KN(SO_2F)_2$.

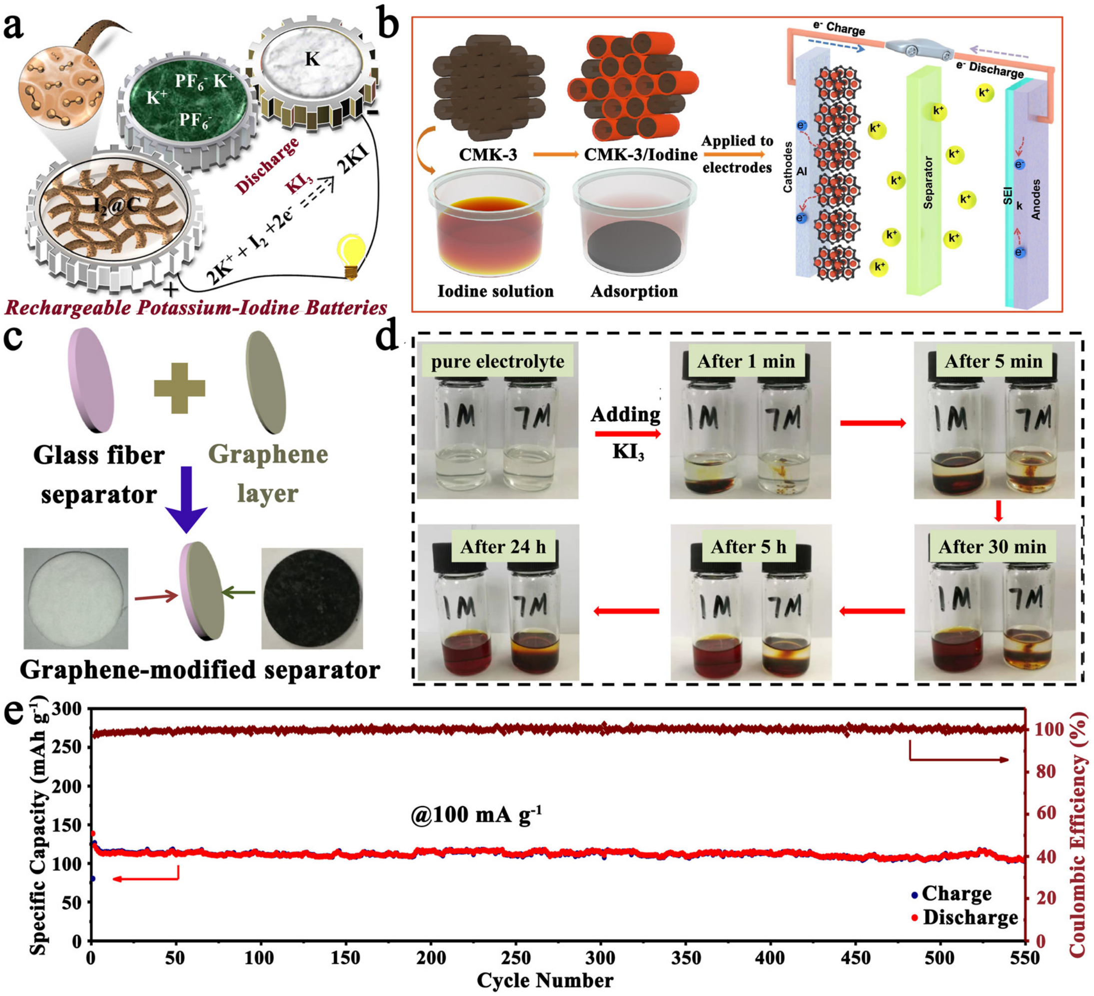

Fig. 10 (a) Schematic diagram for the structure and discharge process of a rechargeable $K-I_2$ secondary battery. Reprinted with permission from ref. 56. Copyright 2018 Elsevier. (b) The preparation process and working mechanism of CMK-3/iodine electrode in a $K-I_2$ battery. Reprinted with permission from ref. 154. Copyright 2019 Elsevier. (c) Schematic diagram for the preparation process of a graphene-modified separator. (d) Digital images of color changes over time for 1 M and 7 M KFSI-EC/DEC electrolytes after adding KI_3. (e) Long-term cycling performance of $K-I_2$ cell at 100 mA g^{-1} with 7 M KFSI-EC/DEC electrolyte, graphene-modified separator, and KI@carbon cathode. Reprinted with permission from ref. 68. Copyright 2021 Elsevier.

lowering the entry criteria for battery research. Besides, they show good compatibility with aqueous electrolytes (*e.g.*, $ZnSO_4$ aqueous solution), avoiding the usage of toxic, flammable, and expensive organic electrolytes and (2) Zn metal offers high theoretical volumetric and gravimetric capacities of 5855 mA h cm^{-3} and 820 mA h g^{-1}, respectively, coupled with a low redox potential of −0.76 V (*vs.* SHE). When matched with an iodine cathode, a theoretical capacity of 211 mA h g^{-1} (even up to 422 mA h g^{-1}) and a voltage window of ∼1.3 V can be obtained. Remarkably, this voltage range is close to that of water splitting (∼1.23 V), indicating that the side reaction of H_2 evolution at the Zn anode can be effectively avoided to realize a highly stable $Zn-I_2$ battery. Considering its low environmental testing and research necessities, coupled with its environmentally friendliness, safety, and cost-effectiveness, the research on $Zn-I_2$ batteries is poised to experience rapid development. In particular, the high solubility of ZnI_2 in water (up to 7 M) allows for the classification of $Zn-I_2$ batteries into two configurations: static and flow (Fig. 11).[163] The static configuration primarily loads iodine at the cathode and employs a small amount of electrolyte to achieve high energy density. This makes it well-suited for mobile electronic devices and flexible batteries. On the other hand, the flow configuration dissolves iodine in the electrolyte and stores energy through the reaction of active species in the flow electrolytes at both the cathode and anode. As a result, this configuration is more suitable for large-scale energy storage stations that provide low-cost service to the grid. In the subsequent section, we will delve into a detailed discussion on both types of $Zn-I_2$ cells.

2.4.1 Zinc–iodine static batteries

2.4.1.1 *Iodine hosts*

Carbon-based hosts. Carbon-based hosts, like those used in $Li-I_2$ batteries, are commonly utilized in $Zn-I_2$ batteries to prevent the shuttle effect caused by the dissolution and diffusion of iodine species. Table 10 in the iodine host section for $Zn-I_2$ batteries presents relevant battery information and performance. In the early stage of $Zn-I_2$ battery development,

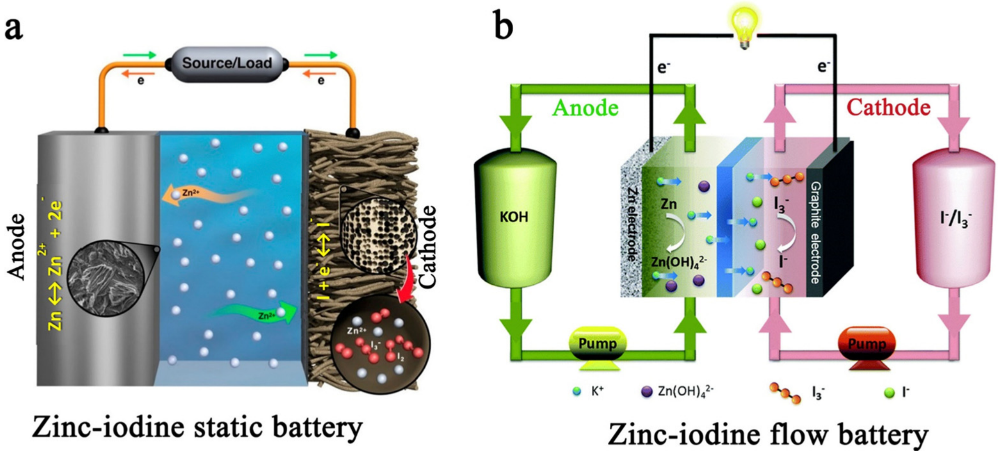

Fig. 11 Schematic illustration of a typical (a) Zn–I_2 static device. Reprinted with permission from ref. 59. Copyright 2017 American Chemical Society; and (b) Zn–I_2 flow device. Reprinted with permission from ref. 164. Copyright 2018 Royal Society of Chemistry.

carbon cloth was extensively studied as an iodine host. Pan *et al.* found that a low E/I ratio (the ratio of the electrolyte volume to iodine mass) could improve the ability of active carbon fiber cloth to inhibit the dissolution of iodine species (Fig. 12a).[59] This is because the lower E/I ratio favors a fast equilibrium between adsorption on the carbon surface and solvation in the electrolyte of iodine species, thereby reducing the total loss of iodine species. Li *et al.* also demonstrated that carbon cloth can act as a self-supporting, mechanically flexible cathode to construct cable-type Zn–I_2 batteries.[72] Particularly, carbon cloth was also revealed to avoid the generation of I_3^- intermediates (the main "culprit" behind the shuttle effect in Zn–I_2 batteries), due to its small internal channels (typical micropore size of ∼6.3 Å), making it difficult for $Zn(I_3)_2$ (minimum diameter of 9.5 Å) to reside (Fig. 12b).[72,165] As a result, carbon cloth was subsequently often adopted as a current collector of Zn–I_2 batteries to improve the battery performance. In combination with the electrodeposition method (*i.e.*, deposition of I^- onto carbon cloth electrochemically), the Zn–I_2 cell with the as-obtained carbon cloth electrode can stably cycle for 2000 cycles with 19% capacity decay at 1 A g^{-1}.[166] Intriguingly, light-assisted chargeable Zn–I_2 cells can be realized by incorporating photo-electrodes (*i.e.*, TiO_2 and BiOI) onto carbon cathodes.[73,167] In particular, a p-type BiOI photocathode is able to increase the discharge voltages (up to 1.49 V) of Zn–I_2 batteries because the positive photovoltage of BiOI can be superimposed onto the I^-/I_3^- redox pair during discharging.[167] However, the stability and rate performance of this kind of battery are very poor and require further optimization and improvement. In addition to carbon cloth, other carbon materials, such as hollow carbon nanostraws,[105] biomass (litchi-shell or gingko) derived hierarchically porous carbon,[168,169] and ZIF-8 derived porous carbon,[170] have also been reported. However, the non-polar nature of carbon weakens its adsorption to polyiodide polarities, causing these materials to have inferior properties.

Next, a heteroatom doping strategy has been proposed for Zn–I_2 batteries, capable of fine-tuning the composition and physicochemical properties of carbon materials, resulting in increased surface polarity of the carbon crystal lattice. Yu *et al.* took the lead in achieving a breakthrough in carbon-based iodine hosts (Fig. 12c).[171] With N-doped porous carbon as the iodine scaffold, they implemented a high-performance Zn–I_2 battery that can be cycled 10 000 times with a capacity retention of 81% at 10C. Especially, they discovered that graphitic-N exhibits the strongest adsorption of iodine, while pyridinic-N has the weakest adsorption of iodine. Furthermore, Liu *et al.* revealed that graphitic-N can promote the conversion of I^- to I_2; this is due to the charge redistribution effect resulting from the interaction of graphite N with iodine molecules, which increases the length of I–I intermolecular bonds, leading to the facile cleavage/formation of I–I bonds during cycling.[170] Surprisingly, Gong *et al.* recently concluded that pyridinic-N is superior in adsorbing iodine species and catalyzing the electrochemical reactions.[172] These conflicting findings call for additional studies with sufficient samples to understand the real role played by different-N species. In any case, it is essential for carbon materials to promote the electrochemical performance of Zn–I_2 batteries by tuning the ratio of graphite-N to pyridine-N species. It is worth noting that the reported multi-component doping materials did not effectively enhance the electrochemical properties of batteries compared to those using a single N-doping. For example, Lu *et al.* reported S and N co-doped three-dimensional graphene foams that can be used as both cathodic and anodic matrixes.[173] However, the as-assembled Zn–I_2 batteries can only achieve 500 cycles with a capacity retention of 81% at 200 mA g^{-1}. Coincidentally, Zn–I_2 batteries with multiple heteroatoms (N, O, S, *etc.*) co-doped graphitic/porous carbon microtubes as the iodine host showed a capacity retention of 86.8% after 1000 cycles.[174] One possible reason for this is that the electrolytes used in these systems contain ZnI_2, which greatly promotes the polyiodide shuttling in the cathode, resulting in poor battery stability.[95,175] As shown in Fig. 12d, the ZnI_2 additive results in a low CE at low rates, indicating that the addition of ZnI_2 actually leads to the formation of more water-soluble polyiodide *via* the process of $I^- + I_2 \rightarrow I_3$, promoting the shuttle effect of batteries. Nonetheless, the battery exhibits an enhanced capacity as the

Table 10 Iodine host materials in Zn–I_2 batteries

1	2	3	4	5	6	7	8	9	10
2017	I_2/active carbon fiber cloth	1 M $ZnSO_4$	38	—	2	3000	90	~128	59
2018	I_2/carbon cloth	2 M $ZnSO_4$	—	8.8	~1	200	91	275	72
2018	I_2/nanoporous activated carbon cloth	1 M $ZnSO_4$	—	4.5	5	1500	90	160	165
2019	S,N co-doped graphene foam	Anolyte, 0.05 M $ZnSO_4$; catholyte, 0.1 M ZnI_2/0.01 M I_2	—	—	~1	500	81	—	173
2019	Super P carbon/Ti/TiO_2 photo-electrode	0.5 M ZnI_2	—	—	0.1 mA cm^{-2}	10	—	—	73
2020	I_2/N-doped porous carbon	1 M $ZnSO_4$	52	1.7	10	10 000	80.9	~144	171
2020	I_2/polyaniline	2 M $ZnSO_4$	~33	~0.7–1.2	~7	700	79	160	186
2020	$I_2/Co[Co_{1/4}Fe_{3/4}(CN)_6]$	2 M $ZnSO_4$	61.2	—	~19	2000	80.2	165.6	190
2021	Polypyrrole/carbon cloth	0.5 M ZnI_2 in 0.1 M HAc/NaAc buffer solution	—	—	~0.4	600	—	—	187
2021	I_2/porous carbon material ZC-mK_2CO_3	2 M $Zn(CF_3SO_3)_2$/0.1 M ZnI_2	50	~1.0–1.4	50	35 000	~98.4	150	175
2021	I_2/N-doped carbon nanofiber	2 M $ZnSO_4$	—	0.8–1.0	5	10 000	77	—	176
2021	I_2/Nb_2CT_X	1 M $ZnSO_4$	80–85	—	~28	23 000	80	—	83
2022	I_2/N-doped porous carbon nanocages	2 M $ZnSO_4$	50	~1.0	~24	3500	—	—	177
2022	Polyiodide/the strong base resin-D296	2 M $ZnSO_4$	40	1.5–2.0	~15	17 000	100	105.1	27
2022	I_2/graphitic/porous carbon microtubes	1 M $ZnSO_4$/0.1 M ZnI_2	50	2.9–3.2	~19	1000	86.8	—	174
2022	Starch	Anolyte, 0.5 M $ZnSO_4$/0.5 M Li_2SO_4; catholyte, 0.1 M I_2/1 M LiI	—	—	~47	50 000	90.5	75	42
2022	Polyaniline/carbon felt	0.75 M $ZnCl_2$/1.5 M KI	—	—	~17	10 000	75.7	—	188
2022	I_2/ZIF-8 derived porous carbon	1 M $ZnSO_4$	22	1.7	~4	1000	72	99	267
2022	I_2/biomass derived hierarchically porous carbon	1 M $ZnSO_4$	41	—	~1.4	800	—	~70	169
2022	I_2/porous hollow carbon nanostraw	0.5 M $ZnSO_4$/0.5 M H_2SO_4	~25	—	~4.7	1500	—	—	105
2022	I_2/CMK-3	2 M $ZnSO_4$	60	1.2–1.5	~47	39 000	~80.6	—	268
2022	I_2/N-doped porous carbon@single Fe atom	2 M $ZnSO_4$	30	1	10	10 000	—	170	183
2022	I_2/carbon cloth	2 M $ZnSO_4$	—	1.45	~4.7	2000	81	~136	166
2022	I_2/ZIF-8-derived N-doped porous carbon	1 M $ZnSO_4$	58	6	~47	10 000	67	~133	170
2022	BiOI semiconductor photoelectrode	10 mM ZnI_2/1.6 mM I_2	—	—	—	—	—	—	167
2023	I_2/N-doped litchi-shell derived porous carbon	1 M $ZnSO_4$	44	1.5	~1.4	400	—	—	168
2023	I_2/N-doped hierarchical porous carbon	1 M $ZnSO_4$	61.6	—	5	10 000	85.2	166.7	172
2023	I_2/carbon nanosheets derived from ZIF-8	2 M $ZnSO_4$	40	~2	20	6000	85	—	180
2023	I_2-loaded defect-rich graphene	2 M $ZnSO_4$/25 mM ZnI_2	40	0.5–1	~4.7	3500	88.1	~230	185
2023	W_2N modified porous carbon polyhedron	2 M $ZnSO_4$	—	0.8–1	5	2000	85	170.3	178
2023	PTCDA-derived porous carbon	2 M $ZnSO_4$	40	—	~23.7	50 000	55	~90	269
2023	I_2/Fe single atom on mesoporous N-doped carbon	2 M $ZnSO_4$/0.04 M I_3^-	76.72	—	~23.7	50 000	79.5	159.7	182
2023	$I_2/LiVS_2$	2 M $ZnSO_4$	60.7	~1.5	~23.7	30 000	86	—	270
2023	I_2/Fe_2N decorated porous N-doped carbon fibers	2 M $ZnSO_4$	—	—	2	1500	79	214	184
2023	I_2/Ni single atoms on hierarchical porous carbon	2 M $ZnSO_4$	41.7	11.6	10	10 000	93.4	141	181
2023	I_2/porous oxidized salt-templated carbon	2 M $ZnSO_4$	26.6	~0.3–0.5	~4.7	10 000	85.04	—	251
2023	Pre-embedded Prussian blue with iodide ions	1 M $ZnSO_4$/5 mM KI	—	—	~19	1500	94	206	191
2023	I_2/N-doped nanocarbons with ~2.5 nm pores	1 M $ZnSO_4$	60.8	—	5	10 000	—	178.8	179

1, year; 2, cathode; 3, electrolyte formula; 4, the mass loading of iodine at the cathode (wt%); 5, the area loading of iodine at the cathode (mg cm^{-2}). Evaluation of Zn–I_2 cell performance: 6, current density (C, 1C = 211 mA h g^{-1}); 7, cycle number; 8, capacity retention (%); 9, reversible capacity (mA h g_{iodine}^{-1}). 10, reference. HAc/NaAc, acetic acid/sodium acetate.

ZnI_2 additive can realize a rapid transformation of iodine from the solid to liquid state and result in an improved iodine utilization.[175] Therefore, the ZnI_2 additive may be a double-edged sword, increasing the utilization of insulating iodine but also aggravating the shuttle effect of the battery. In terms of the structural design of heteroatom-doped carbon, N-doped porous carbon nanofibers, N-doped porous carbon nanocages, and tungsten nitride-modified porous carbon (ZIF-8) polyhedra have also been reported with excellent energy storage performance (Fig. 12e).[176–178] Besides, as mentioned earlier, the control of pore size in carbon-based materials enables the I^-/I_2 process and prevents the polyiodide shuttle effect effectively. Thus, Hou *et al.* constructed an N-doped nanocarbon with a pore structure of approximately 2.5 nm meticulously.[179] As anticipated, the resulting N-doped nanocarbon cathode, with an iodine content of 60.8 wt%, exhibited excellent long-term cycling stability, corresponding to a reversible specific capacity of 178.8 mA h g^{-1} after 10 000 cycles at 5C. To further investigate the structure-electrochemical properties of heteroatom-doped carbon cathodes in Zn–I_2 batteries, Sun *et al.* prepared four different configurations of porous carbon, namely, carbon nanosheets, carbon nanoshells, carbon skeletons, and carbon dodecahedra, by altering the additives with ZIF-8 as precursors.[180] Despite having the highest heteroatom content, carbon dodecahedra/I_2 did not exhibit the best electrochemical performance. In contrast, carbon nanosheets/I_2 displayed superior performance due to its maximum total pore volume and suitable pore size (containing pores of 1.2–3 nm). This indicates that heteroatom content alone is insufficient in assessing material properties, while factors such as pore size, porosity, specific surface area, and morphology, are equally significant.

Based on the aforementioned approaches, the polyiodide shuttle effect in Zn–I_2 batteries can be mitigated effectively. However, another pressing concern pertains to the sluggish cell

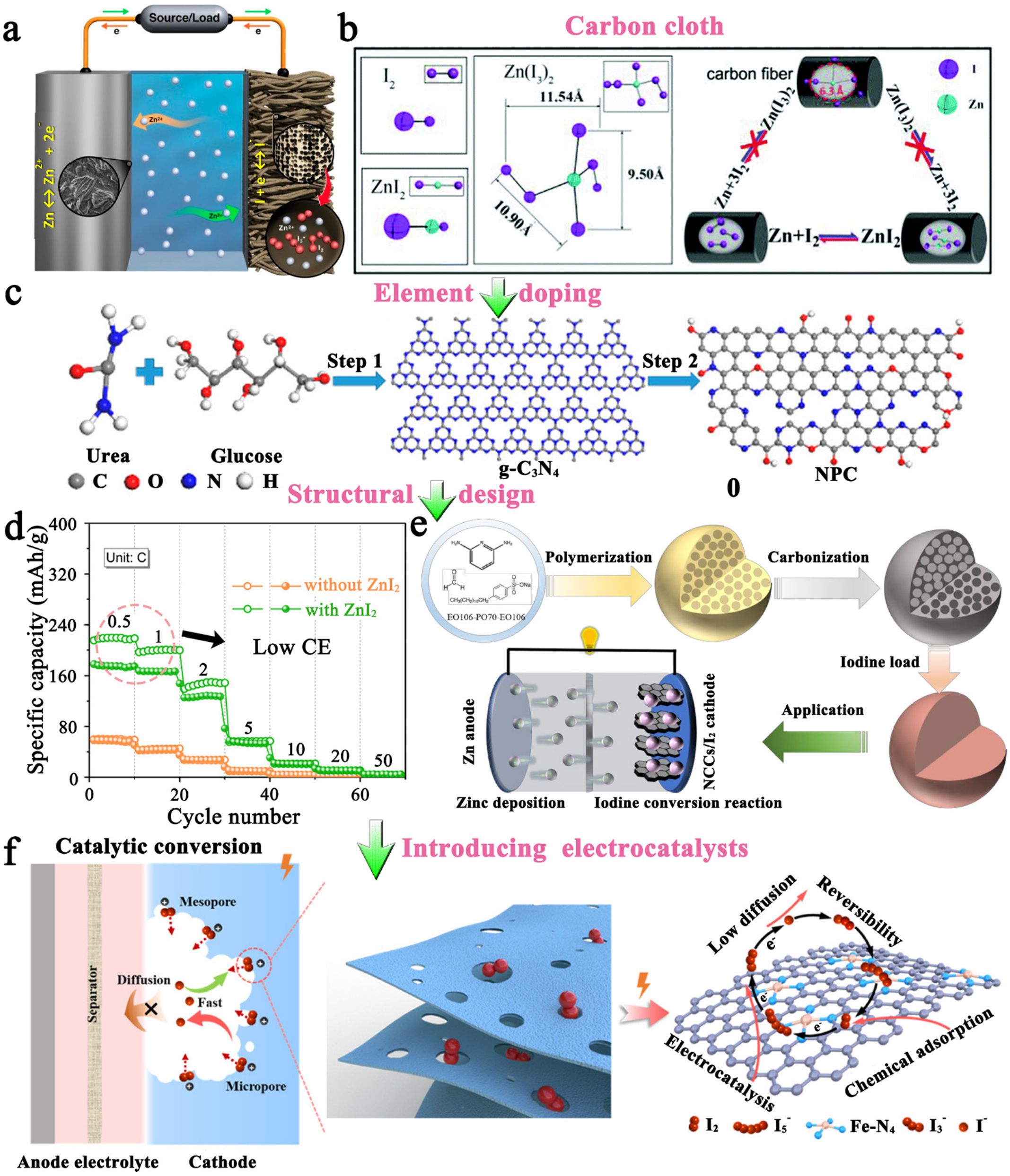

Fig. 12 (a) Schematic diagram for the working process of Zn–I_2 battery with active carbon fiber cloth@I_2 cathode. Reprinted with permission from ref. 59. Copyright 2017 American Chemical Society. (b) The configurations of I_2, ZnI_2 and $Zn(I_3)_2$ molecules, and the proposed possible electrode reaction process in the micropores of carbon cloth. Reprinted with permission from ref. 72. Copyright 2018 Royal Society of Chemistry. (c) Schematic illustration for the synthesis process of a nitrogen-doped porous carbon host. Reprinted with permission from ref. 171. Copyright 2020 American Chemical Society. (d) Rate performance of Zn–I_2 cells in 2 M $Zn(CF_3SO_3)_2$ electrolyte with or without 0.1 M ZnI_2 additive. Reprinted with permission from ref. 175. Copyright 2021 American Chemical Society. (e) Schematic synthesis for the nitrogen-doped porous carbon nanocages@I_2 cathode in a Zn–I_2 battery. Reprinted with permission from ref. 183. Copyright 2022 American Chemical Society. (f) Schematic diagram for the working mechanism of polyiodide adsorption/conversion on the porous carbon with the atomic bridging structure of metal–nitrogen–carbon. Reprinted with permission from ref. 177. Copyright 2022 American Chemical Society.

kinetics caused by the high activation energy of iodine conversion and the insulating property of I_2 ($\sim 10^{-9}$ S cm^{-1}).[180] To address this, one effective solution lies in the incorporation of single atom catalysts (SACs) into carbon-based materials (Fig. 12f). This strategy exploits the activated and isolated catalytic metal atoms of SACs, which provide optimal utilization of catalytic sites for catalytic reactions. Consequently, a small amount of catalyst enables a potent catalytic effect, avoiding an increase in the inactive cathode material. Currently, investigations are focusing on Fe and Ni single atoms in Zn–I_2 batteries, both exhibiting excellent catalytic properties.[181–183] For instance, when Fe single atoms were introduced into N-doped porous carbon, the resulting composite could achieve an outstanding redox kinetics, corresponding to a specific capacity of

158 mA h g^{-1}, even at 20C.[183] This can be attributed to the decreased energy barrier for the iodine conversion process facilitated by the Fe single atoms. Similarly, Ma *et al.* realized an ultra-high specific capacity of 121 mA h g^{-1} at 50C by dispersing Ni single atoms within hierarchical N-doped porous carbon, affirming the beneficial role of SACs in facilitating the iodine redox process.[181] On the other hand, transition metal oxides, sulfides, nitrides, and carbides are also regarded as excellent electrocatalysts. Among them, transition metal nitride (Fe_2N) has been explored for use as an electrocatalyst in Zn–I_2 batteries due to its favorable electronic conductivity and intrinsic catalytic activity. Ding *et al.* reported the fabrication of a Fe_2N-decorated N-doped carbon fiber-based iodine host using electrospinning and carbonization techniques.[184] The resulting Zn–I_2 batteries delivered a specific capacity of 146 mA h g^{-1} at 10C, slightly inferior to that achieved with SACs. In addition to the above electrocatalysts, Niu *et al.* also proposed the concept of defect-induced catalysis to expedite the iodine conversion process.[185] By introducing defects (specifically carbon seven-membered ring defect sites) in the N-doped graphene, the active sites were increased while effectively catalyzing the iodine conversion process. Consequently, Zn–I_2 batteries exhibited impressive specific capacities of 278.4 mA h g^{-1} at 0.5 A g^{-1} and 131.9 mA h g^{-1} at 10 A g^{-1}. Therefore, the incorporation of electrocatalytic functionality into carbon-based materials proves to be a viable approach for achieving fast cathodic kinetics.

Overall, future design of carbon-based hosts in Zn–I_2 batteries may require the following key factors: (1) a large surface area to provide a large number of active sites to reserve and anchor iodine species; (2) suitable pore size to hinder the formation of $Zn(I_3)_2$; (3) heteroatom doping to enhance the interaction between carbon and iodine species, thereby resulting in increased stability and reversibility of battery; (4) modulation of the graphite-N/pyridine-N value to optimize the adsorption and catalytic capacity of the materials for iodine species; and (5) the introduction of electrocatalysts (*e.g.*, metal single atoms, transition metal oxides/sulfides/nitrides/carbides), and defective engineering to further enhance the catalytic ability for efficient iodine conversion.

Organic polymer hosts. In addition to carbon-based hosts, organic compounds have recently been pursued in Zn–I_2 batteries due to their abundant active sites, adjustable structure, sustainability, and cost-effectiveness. However, PVP, which has been commonly investigated in Li–I_2 batteries, may not be suitable for Zn–I_2 batteries because of its high solubility in water. Therefore, when designing organic iodine hosts for different MIBs, the compatibility of electrolytes and electrode materials must be considered to avoid possible problems, such as dissolution and side reactions. Conducting polymers, such as polyaniline (PANI) and polypyrrole (PPy), have been extensively studied in Zn–I_2 batteries. In general, the PANI framework can confine polyiodide through the electrostatic interactions with non-protonated amine (–NH–) and protonated imine (–NH^+=) functional groups (Fig. 13a).[186] Besides, the doping/de-doping processes of polyiodide in the PANI framework could improve the conductivity of PANI, thereby promoting the redox kinetics. Likewise, PPy also exhibits a doping/de-doping mechanism of iodine species on its backbone.[187] Significantly, PANI has higher capacity and stronger stability than PPy.[188] This can be attributed to the micro-nano-porous structure of PANI (PPy with a dense structure), which can facilitate the contact of PANI with electrolytes and also provide more active adsorption sites to minimize the shuttling of polyiodide ions. However, the lifetime of PANI-based Zn–I_2 batteries is relatively short (<1000 cycles). One boosting strategy is to compound PANI with carbon materials but this undoubtedly increases the content of inactive material and reduces the cell density (Fig. 13b).[188] Another approach is to change the electrolyte formulation by using a high concentration of $ZnCl_2$ (containing KI or ZnI_2 as the iodine source) (Fig. 13c). In this case, I^- ions exist in the form of $[ZnI_x(OH_2)_{4-x}]^{2-x}$ ($x = 2$), which can prevent I_2 from forming water-soluble polyiodide, thereby improving battery performance[86,189] As a result, the as-prepared PANI-based Zn–I_2 battery was able to maintain an ultrahigh capacity retention of 99.9% after 1000 cycles.[189] Despite this, the adsorption capacity of PANI for polyiodide is not sufficient to realize Zn–I_2 batteries with long-term service life. Zhang *et al.* took the lead in making a breakthrough in the polymer-based iodine host of Zn–I_2 batteries.[27] They proposed an inexpensive, facile, and universal quaternization engineering approach to regulate polyiodide. Benefiting from the construction of an "electric double layer" structure between quaternary ammonium cations and iodine anions, the polyiodide shuttling is significantly eliminated. Especially, quaternary ammonium cations enable the generation of a large energy barrier between I_3^- and I_2, resulting in fast solution-based iodine chemistry (I^-/I_3^-) for high-rate charge–discharge of batteries. The resulting cutting-edge Zn–I_2 battery demonstrated ∼100% capacity retention over 17 000 cycles at 3.2 A g^{-1}, which greatly prolongs the life of polymer-based Zn–I_2 batteries and effectively improves the rate performance of the battery (Fig. 13d). Besides, Qiao's group reported the utilization of starch as an iodine host.[42] Owing to the unique double-helix structure of starch, various iodine species can be strongly confined within the helical chains through bonding effects (Fig. 13e and f). The resulting starch-based Zn–I_2 battery delivered over 50 000 cycles with a capacity retention of 90.5% at 10 A g^{-1}. All these results well confirm the promising application of organic polymer hosts in Zn–I_2 batteries, especially considering that long-lasting and high-rate Zn–I_2 batteries have been achieved.

Other types of iodine hosts. In addition to carbon-based hosts and organic polymer hosts, several other types of materials have been taken into consideration for their utilization as iodine hosts, including Prussian blue analogues (PBAs), Prussian blue (PB) and MXenes.[83,190,191] Generally, PBAs possess adequate porosity, continuous and ordered micropore channels, and transition-metal species with electrochemical catalytic functions, which endow PBAs with the promising potential to act as iodine hosts. Accordingly, the rate capability of the $Co[Co_{1/4}Fe_{3/4}(CN)_6]/I_2\|Zn$ cell can reach to 151.4 mA h g^{-1} even at 20 A g^{-1}.[190] Nevertheless, its cycle stability performance is not very prominent, with a capacity retention of 80.2% after 2000 cycles at 4 A g^{-1}. This may be

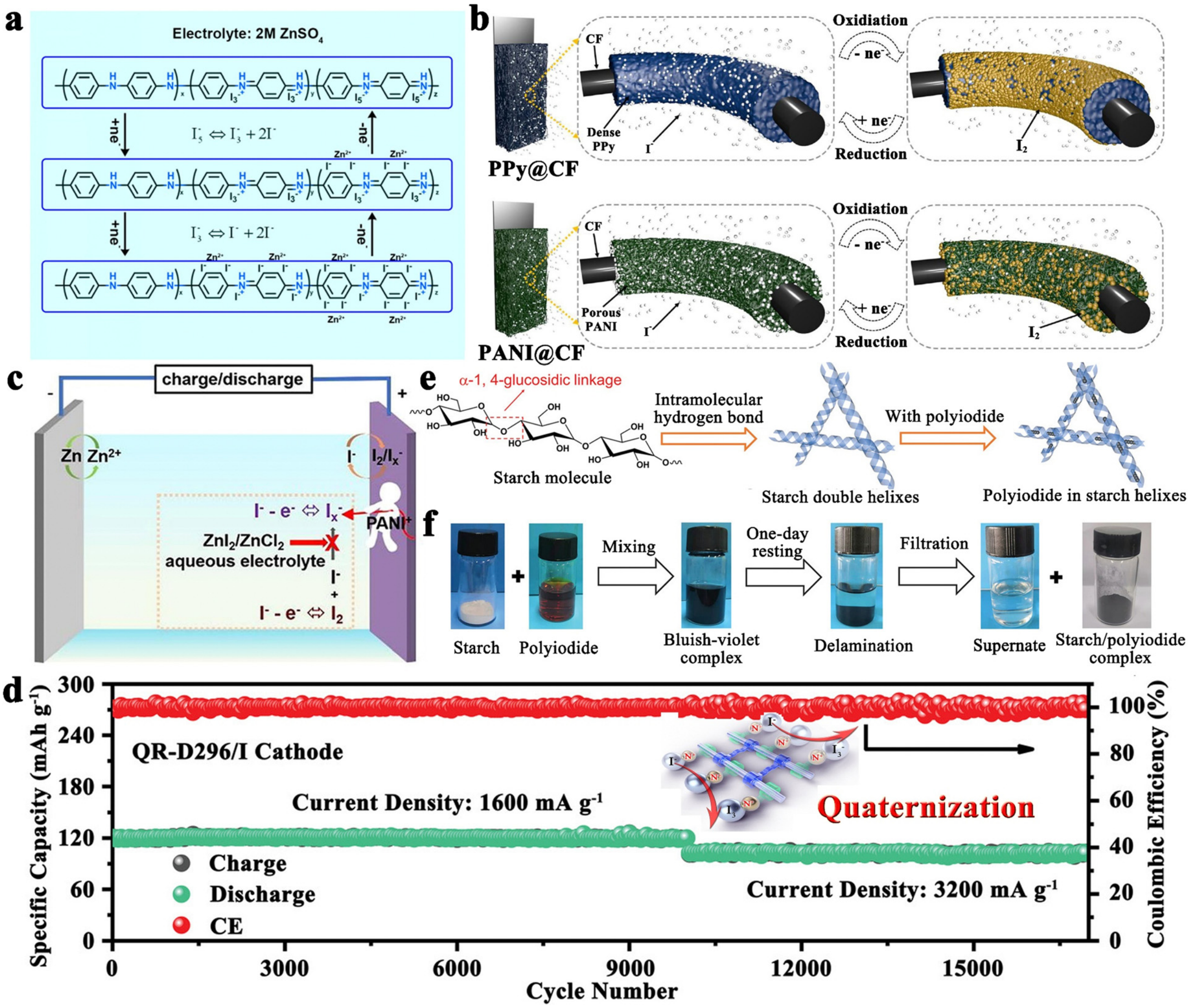

Fig. 13 (a) Proposed redox mechanism of the PANI@I_2 cathode in a Zn–I_2 battery. Reprinted with permission from ref. 186. Copyright 2020 American Chemical Society. (b) Schematic diagram for the redox reaction of iodine species in PPy@carbon felt and PANI@carbon felt hosts. Reprinted with permission from ref. 188. Copyright 2022 Elsevier. (c) Schematic illustration for the working process of the PANI@I_2 cathode using ZnI_2/$ZnCl_2$ electrolyte in a Zn–I_2 cell. Reprinted with permission from ref. 189. 2021 Elsevier. (d) Long-term cycling performance of quaternized cathode at different C-rates. Reprinted with permission from ref. 27. Copyright 2022 Wiley. (e) Schematic diagrams for the chemical/double-helix structure of starch molecules and starch/polyiodide complex. (f) Photographs revealing the polyiodide capture processes by starch. Reprinted with permission from ref. 42. Copyright 2022 Wiley.

attributed to its uncontrolled phase transformation upon cycling process, resulting in structural failure.[192,193] Similarly, the PB cathode with pre-embedded iodide ions had a short lifetime of 1500 cycles at 4 A g^{-1}.[191] On the other hand, MXenes could also be considered as iodine hosts on account of their exceptional electrical conductivity, abundant surface terminations (=O, –F, –OH, *etc.*), periodic layered microstructure, and arrayed interlayer gap. Li *et al.* used the 211-type Nb-based MXene (Nb_2CT_x) as a proof-of-concept for incorporation with I_2.[83] As a result, the obtained I_2@Nb_2CT_x MXene electrode exhibited a lifespan of 23 000 cycles at 6 A g^{-1}, corresponding to a capacity retention of 80%. The emergence of these materials has greatly expanded the selection of iodine hosts. Importantly, the concept of catalyzing the iodine reduction reaction could be popularized more widely, as it commonly leads to batteries with extremely high-rate capability, even as high as 20 A g^{-1} (PBAs).

2.4.1.2 Electrolyte. Extensive research has also been carried out on electrolytes for Zn–I_2 batteries. Table 11 in the modified electrolyte section for Zn–I_2 batteries presents the relevant battery information and performance. An important breakthrough lies in the realization of the two-electron iodine redox reaction (*i.e.*, $I^- \leftrightarrow I^0 \leftrightarrow I^+$). Typically, I^+ is highly unstable in aqueous solutions and can be further oxidized to form electrochemically irreversible IO_3^-. However, electrophilic I^+ will be activated and stabilized by forming charge-transfer complexes through strong interactions with nucleophile species, such as halides, cyanides, and amines.[40,87,194–197] For the first time, Li *et al.* investigated the effects of different salt components (*i.e.*, 2 M $ZnSO_4$ electrolyte with/without one of KF, NaF, NH_4F, KCl, NaCl, and NH_4Cl salt) on the activation and stability of I^+ ions in Zn–I_2 batteries.[74] As shown in Fig. 14a, with the introduction

Table 11 Modified electrolytes in Zn-I_2 batteries

1	2	3	4	5	6	7	8	9
2020	2 M $ZnCl_2$/1 M KCl	$Ti_3C_2I_2$ MXene	—	~14	2800	80	—	74
2020	Anolyte, 0.5 M $ZnSO_4$/PEO_{53}–PPO_{34}–PEO_{53}; catholyte, 0.1 M I_2/1 M KI/PEO_{53}–PPO_{34}–PEO_{53}	Carbon cloth	—	1	500	94.3	198	82
2020	Anolyte, 0.5 M $ZnSO_4$ in PEO_{53}–PPO_{34}–PEO_{53}; catholyte, 0.2 M I_2/porous MOF gel/carbon cloth	—	—	1	1500	95.8	184.9	81
2021	$ZnCl_2$/LiCl/acetonitrile (19 : 19 : 8, m/m/m)	I_2/PAC carbon	0.48–0.8	~9.5	6000	82	420	40
2021	Alginate-based polyanionic hydrogel electrolyte	I_2/AC	—	~9.5	2000	66.8	75.3	207
2022	25% PEG/1 M $Zn(CF_3SO_3)_2$/1 M KI	Double carbon cloth	—	7 mA·cm^{-2}	1200	~58	—	203
2022	1 M $Zn(CF_3SO_3)_2$/4 M *N*-methylacetamide/ 0.5 M KI in 20% volume fractions of H_2O	AC	—	4 mA·cm^{-2}	5000	98.7	2.2 mA h cm^{-2}	85
2022	9 M $ZnCl_2$/1 M ZnI_2	Polyaniline	—	6 mA cm^{-2}	1000	99.9	—	189
2022	1 M ZnI_2 in starch aqueous solution	Carbon cloth	—	10 mA cm^{-2}	2000	92	0.72 mA h cm^{-2}	271
2022	Cross-linked polyacrylamide/2 M $ZnSO_4$/ 0.5 M 1-methyl-3-*n*-propylimidazolium iodide polyelectrolyte	Hydrophilic O-containing CNT	—	10 mA cm^{-2}	2600	89.2	~0.35 mA h cm^{-2}	206
2023	2 M $ZnSO_4$/0.2 M ZnI_2/20% EG	Ordered porous graphene	—	~24	15 000	97.6	144.1 mA h cm^{-3}	204
2023	Iota-carrageenan gel electrolyte	N,P co-doped porous carbon	~1.5	5	5000	91.9	—	88
2023	5 M KI/20 M $ZnCl_2$	Hydrothermal RGO	22.5	50 mA cm^{-2}	2000	~100	2 mA h cm^{-2}	202
2023	Vermiculite nanosheets suspension electrolyte	I_2/activated carbon cloth	2.5–2.8	20	40 000	~100	149.8	205
2023	4 M $ZnSO_4$/0.4 M LiI	3D porous carbon	—	2	5000	95	—	272
2023	5.9 mole per kilogram $ZnCl_2$ + 0.20 M KI	I_2/activated porous corncob carbon	0.8–1.8	~2.4	600	—	—	273

1, year; 2, electrolyte formula; 3, cathode; 4, iodine loading (mg cm^{-2}). Evaluation of Zn–I_2 cell performance: 5, current density (C, 1C = 211 mA h g^{-1}); 6, cycle number; 7, capacity retention (%); 8, reversible capacity (mA h g_{iodine}^{-1}). 9, reference. EG, ethylene glycol; PPO, poly(propylene oxide); PEG, poly(ethylene glycol).

of F^- (Cl^-) ions, an obvious redox peak pair related to the redox of I^0/I^+ appeared at approximately 1.84/1.66 V (1.74/1.66 V), indicating the successful activation of I^0/I^+ conversion. Intriguingly, the high-potential I^0/I^+ reaction in chloride-containing salt electrolytes is more reversible compared to the electrolytes containing F^- ions. On the other hand, cations also affect the stability of I^0/I^+ conversion. Among three different cations (K^+, Na^+, and NH_4^+), the K^+ cation is recognized to raise the redox potential of the I^-/I^0 transition due to its lower conversion energy barrier compared to the Na^+ and NH_4^+ ions.[74] In view of this, a mixed electrolyte with 2 M $ZnCl_2$ and 1 M KCl was chosen to realize the two-electron iodine redox reaction in Zn–I_2 batteries. By using the $Ti_3C_2I_2$ MXene as the cathode and Zn foil as the anode, the as-assembled Zn–I_2 battery showed a cyclic lifespan of over 2800 cycles with 80% capacity retention, as well as an excellent rate of 126 mA h g^{-1} (207 mA h g^{-1}) at 5 A g^{-1} (0.5 A g^{-1}) (based on the mass of $Ti_3C_2I_2$). However, the charge transfer complexes may be at risk of hydrolysis in aqueous media.[196,198,199] Because ICl would be hydrated by water (donating its lone pair of electrons) to form H_2OICl due to the unsaturated coordination sphere of iodine in ICl.[198,200] Then, the deprotonation or the disproportionation of the H_2OICl hydrate yields HIO, *via.* $H_2OICl \rightarrow HIO + HCl$ (deprotonation), or $H_2OICl \rightarrow H_2OI^+ + Cl^- \rightarrow HIO + HCl$ (disproportionation) (total reaction: $ICl + H_2O \rightarrow HIO + HCl$). Moreover, HIO intermediates could be further decomposed in acidic environments, *via.* $2HOI \rightarrow HIO_2 + HI$, and $HOI + HIO_2 \rightarrow HIO_3 + HI$ (total reaction: $3HOI \rightarrow HIO_3 + 2HI$).[196,199] Especially, in the presence of light or metal catalysts, HIO intermediates would be decomposed *via* another pathway, *i.e.*, $2HIO \leftrightarrow 2HI + O_2$, and $2HIO + 2IH \leftrightarrow 2I_2 + 2H_2O$ (total reaction: $4HIO \leftrightarrow 2I_2 + 2H_2O + O_2$).[40,201] Therefore, Zou *et al.* recently achieved a more reversible I^0/I^+ conversion by considering the hydrolysis issue of ICl.[40] They found that the I^0/I^+ process could be activated even in a diluted 1 M $ZnCl_2$ solution, despite its low reversibility. Upon increasing the $ZnCl_2$ concentration to 30 M, the I^0/I^+ conversion will be fully activated and exhibit high reversibility due to the reduction of free water and the strong coordination of Cl^- to I^+. Nevertheless, such a high concentration of $ZnCl_2$ electrolyte resulted in poor battery stability, which may be attributed to the formation of non-electroactive Zn–I clusters ($[ZnI_x(OH_2)_{4-x}]^{2-x}$ (x = 2)) during the cycling process and the low Cl^- activity that cannot greatly suppress I^+ hydrolysis (Fig. 14b). Notably, Hong *et al.* revealed that the Zn–I clusters formed by high concentrations of chloride salts can effectively inhibit the shuttling of polyiodide; this is due to the low concentration level of free iodide ions in such an electrolyte, which prevents iodine to combine with iodide ions to form water-soluble polyiodide (Fig. 14c).[86] In this respect, it is still worth considering whether the formation of Zn–I clusters contributes to cell instability in two-electron iodine redox reactions. One more thing to note is that $ZnCl_2$ is a strong Lewis acid that can form $[ZnCl_2(OH)]^-$ anions and is therefore highly corrosive. Consequently, 30 M $ZnCl_2$ electrolyte may cause severe corrosion to the battery structure, causing a decline in battery capacity. Given this, a hybrid electrolyte of 19 M $ZnCl_2$ + 19 M LiCl + 8 M acetonitrile was formulated. LiCl, which possesses high solubility and miscibility with $ZnCl_2$, can not only provide an extra Cl^- source but also further regulate the coordination between Zn^{2+}, H_2O, and Cl^- due to the unique solvation properties of lithium ions. Additionally, acetonitrile can act as a diluent to facilitate ion transport while also reducing water activity due to its inertness. In this case, the Zn–I_2 battery revealed a reversible

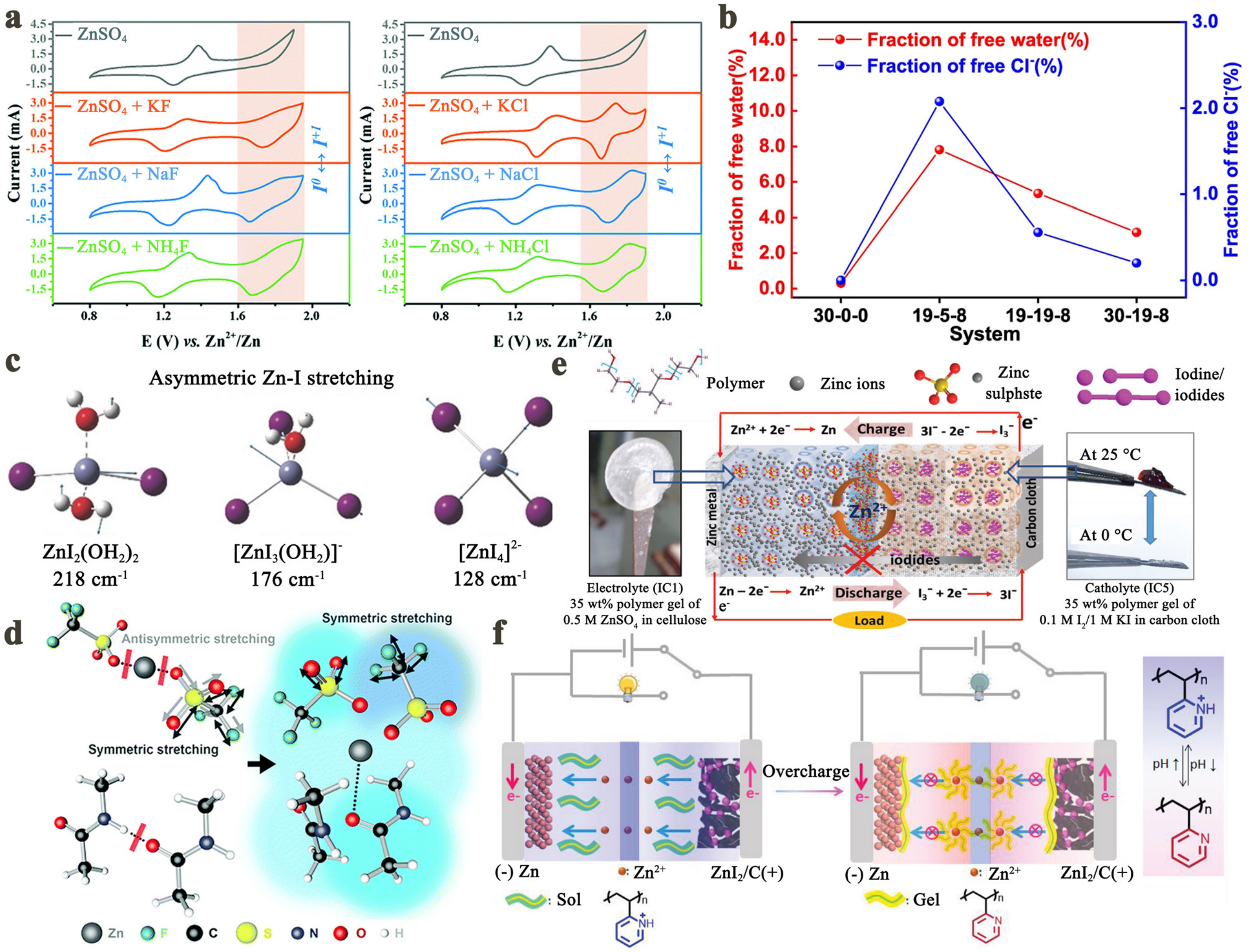

Fig. 14 (a) CV curves of the Zn–I_2 batteries in 2 M $ZnSO_4$ electrolyte without or with various F^-/Cl^-ions additives (including KF, NaF, NH_4F, KCl, NaCl, and NH_4Cl salts). Reprinted with permission from ref. 74. Copyright 2020 Royal Society of Chemistry. (b) Summary of free water and Cl^- contents in electrolytes with different formulations based on molecular dynamics simulations. The horizontal coordinate in the graph defines the specific molarity of $ZnCl_2$, LiCl, and ACN in water. For example, 19-19-8 means 19 M $ZnCl_2$ + 19 M LiCl + 8 M acetonitrile. Reprinted with permission from ref. 40. Copyright 2021 Springer Nature. (c) Depiction of major Raman modes of zinc iodide in aqueous solution from DFT calculations. H, white; O, red; Zn, light blue; I, purple. Reprinted with permission from ref. 86. Copyright 2019 Wiley. (d) The proposed formation mechanism of $Zn(CF_3SO_3)_2$@*N*-methylacetamide eutectic solution. Reprinted with permission from ref. 85. Copyright 2022 Royal Society of Chemistry. (e) Schematic representation of the working mechanism of Zn–I_2 battery with PEO_{53}–PPO_{34}–PEO_{53} gel electrolyte. Reprinted with permission from ref. 82. Copyright 2020 Wiley. (f) Schematic illustration of the self-protection function of a stimulus-responsive Zn–I_2 battery. Reprinted with permission from ref. 208. Copyright 2020 Wiley.

capacity of 420 mA h g^{-1} after 6000 cycles with a capacity fading of only 0.003% per cycle at 2 A g^{-1}, indicating noteworthy competitiveness against vanadium-based/manganese-based oxides.

In addition to increasing the theoretical capacity of the battery, electrolytes have also been developed to serve multiple functions, including the reduction of iodine species diffusion, fabrication of flexible electronic devices, protection of the zinc anode, and prevention of battery overcharging. Of these functions, research into mitigating the shuttle effect of Zn–I_2 batteries has received the most attention. In theory, the shuttle effect in Zn–I_2 batteries arises primarily from the formation of water-soluble polyiodide (iodine is hardly soluble in water). Therefore, the aforementioned high concentration of chloride salts can effectively avoid the shuttle effect by inhibiting the formation of polyiodide. As reported by Ji *et al.*, a Zn–I_2 cell based on a hydrothermally RGO cathode and a highly concentrated $ZnCl_2$ electrolyte (5 M KI/20 M $ZnCl_2$) was able to achieve 2000 cycles without capacity decline even at an ultra-high iodine load of 25.33 mg cm^{-2}.[202] Nevertheless, the high cost brought by the highly concentrated electrolytes cannot be ignored. Given this, Yang *et al.* developed a novel electrolyte (*i.e.*, 1 M $Zn(CF_3SO_3)_2$ + 4 M *N*-methylacetamide + 0.5 M KI in 20% volume fractions of H_2O) to circumvent the formation of I_3^- intermediates.[85] In this case, Zn^{2+} in the eutectic solution has a unique double-shell solvated structure, that is, a compact inner layer composed of I^- and $CF_3SO_3^-$, and an outer layer including H_2O and C_3H_7NO (Fig. 14d). This not only reduces the amount of free water effectively, but also screens the I^- interaction with surrounding ions or molecules, thereby suppressing the formation of I_3^-. As a result, the as-assembled Zn–I_2 battery performed 5000 cycles with a capacity retention of 98.7%. In such a system, however, a low concentration of active species (0.5 M KI) means a low energy density, suggesting that the protocol may need further refinement. On the other hand, the restriction of polyiodide diffusion, as a conventional method to mitigate the shuttle effect, is also achieved by electrolyte additives and gel electrolytes. Research on electrolyte additives is relatively scarce. Recently, polyethylene glycol (PEG400) and ethylene glycol (EG) additives have been reported to inhibit the formation and shuttling of I_3^- by complexing with I_2.[203,204] Additionally, Zhao *et al.* introduced vermiculite nanosheets (VS) into a 1 M $ZnSO_4$ solution to form a VS suspended electrolyte.[205] By leveraging the interaction between polyiodide and silica-oxygen bonds present in the VS, the dissolved polyiodide elegantly binds to the scattered VS particles in the bulk electrolyte, thus triumphantly alleviating the pernicious shuttle effect. For gel electrolytes, Soni's group found that the poly(ethylene oxide)–poly(propylene oxide)–poly(ethylene oxide) (FF7, PEO_{53}–PPO_{34}–PEO_{53}) gel electrolyte for Zn–I_2 cells could lead to future inhibition of iodine species migration and prevent self-discharge (Fig. 14e).[82] However, under such conditions, the battery had a short lifespan of only 500 cycles. Hence, they implanted a highly solubilized iodine-enriched metal–organic gel-enabled catholyte into PEO_{53}–PPO_{34}–PEO_{53}, since MOFs can provide strong adsorption properties for polyiodide.[81] Consequently, the cyclic life of Zn–I_2 cells was significantly improved to 1500 cycles with a superior capacity retention of 95.8% at 1C. Notably, gel electrolytes with abundant electronegative groups, such as hydroxyl,[206] carboxyl,[207] and sulfate groups,[88] are able to mitigate the shuttle effect through electrostatic repulsion. For example, Shang *et al.* achieved a long lifetime of 2000 cycles with a capacity retention of 66.8% at 2 A g^{-1} in a Zn–I_2 battery by virtue of abundant –COOH groups in the alginate-based polyanionic hydrogel electrolyte.[207] Benefiting from the flexible structure of gel electrolytes, Lin *et al.* recently employed the cross-linked polyacrylamide/2 M $ZnSO_4$/0.5 M 1-methyl-3-*n*-propylimidazolium iodide (CPAM-Zn-I-0.5) polyelectrolyte to construct Zn–I_2 microbatteries.[206] As a result, the as-fabricated microbattery showed unprecedented volumetric and areal energy densities of 1647.3 mW h cm^{-3} and 2339.1 μW h cm^{-2}, demonstrating the great potential of Zn–I_2 cells in the field of micro-batteries. Besides, a novel Zn–I_2 battery with fast overcharge self-protection capability could be obtained based on poly(2-vinylpyridine) (P2VP) additives (Fig. 14f).[208] As the pH changes in overcharged Zn–I_2 batteries can induce a reversible and fast transition of the P2VP-based aqueous electrolyte from a conductive soluble state to a gel state with high internal resistance, which in turn results in a rapid shutdown of the battery under overcharge conditions and prevents continued battery damage.

All in all, in developing electrolytes for zinc–iodine batteries, researchers have focused on three main areas: (1) activating and stabilizing the I^0/I^+ process to improve the battery energy density with the key points on stabilizing I^+ ions and inhibiting water activity; (2) inhibiting the formation of water-soluble polyiodide (*i.e.*, achieving I^-/I_2 conversion), which requires electrolytes capable of reducing the activity of I^- ions to prevent them from combining with I_2; and (3) mitigating the diffusion of water-soluble polyiodide through gel electrolytes and electrolyte additives (PEG400, EG). In addition, due to their flexibility, lack of liquid components, safety, and high energy density, Zn–I_2 batteries utilizing gel electrolytes offer potential for use in micro-batteries and flexible wearable devices.

2.4.1.3 Separators and interlayers

Separators. As one of the important constituents of batteries, the separator plays a crucial role in the performance of batteries. Table 12 in the modified separator section for Zn–I_2 batteries presents the relevant information and performance. Typically, the separators in Zn–I_2 batteries can assume the dual role of inhibiting polyiodide diffusion and protecting the zinc anode *via* their ion channel function. For instance, Yang *et al.* selected a Zn-BTC ($Zn_3(BTC)_2$) MOF that has high stability under aqueous conditions and a suitable porous structure, as the functional separator to realize high-performance Zn–I_2 batteries.[92] Attributed to the –COOH groups on the walls of Zn-BTC channels, the separator can selectively block the migration of I_3^- to the Zn anode through electrostatic repulsion.[207,209] Additionally, the Zn-BTC separator also suppressed H_2O-induced Zn corrosion by expelling out free water molecules from Zn^{2+} cations, thereby resulting in enhanced stability of the Zn anode (Fig. 15a and b). Therefore, the Zn–I_2 battery achieved a long cycling lifetime of

Table 12 Modified separators and interlayers in Zn–I_2 batteries

1	2	3	4	5	6	7	8	9	10	11
2020	$Zn_3(BTC)_2$ MOF membrane	Anolyte, 0.5 M $ZnSO_4$/0.5 M Li_2SO_4; catholyte 0.5 M $ZnSO_4$/1 M LiI/0.1 M I_2	KB/PTFE	0.2 (0.2)	3000	~9	8000	84.6	85.1	92
2022	Zeolite membrane of $Na_{12}(AlO_2)_{12}(SiO_2)_{12}\cdot xH_2O$	Anolyte, 0.5 M $ZnSO_4$/0.5 M Li_2SO_4; catholyte, 0.5 M $ZnSO_4$/1 M LiI/0.1 M I_2	KB/PTFE	1 (1)	~260	~19	30 000	91	44.5	90
2022	PEDOT:PSS interlayer	2 M $ZnSO_4$	I_2/active carbon	10 (5)	550	~47	20 000	~72	—	211
2023	KB modified cotton fiber separator	1 M $ZnSO_4$	I_2/MOF-5-derived mesoporous carbon	—	—	~4.7	2000	—	112	210

1, year; 2, anode; 3, electrolyte formula; 4, cathode. Evaluation of Zn‖Zn cell performance: 5, current density (mA cm^{-2}) and areal capacity (mA h cm^{-2}); 6, cycle time (h). Evaluation of Zn–I_2 cell performance: 7, current density (C, 1C = 211 mA h g^{-1}); 8, cycle number; 9, capacity retention (%); 10, reversible capacity (mA h $g^{-1}_{\text{iodine or LiI}}$). 11, reference. PEDOT, poly(3,4-ethylenedioxythiophene); PSS, polystyrene sulfonate.

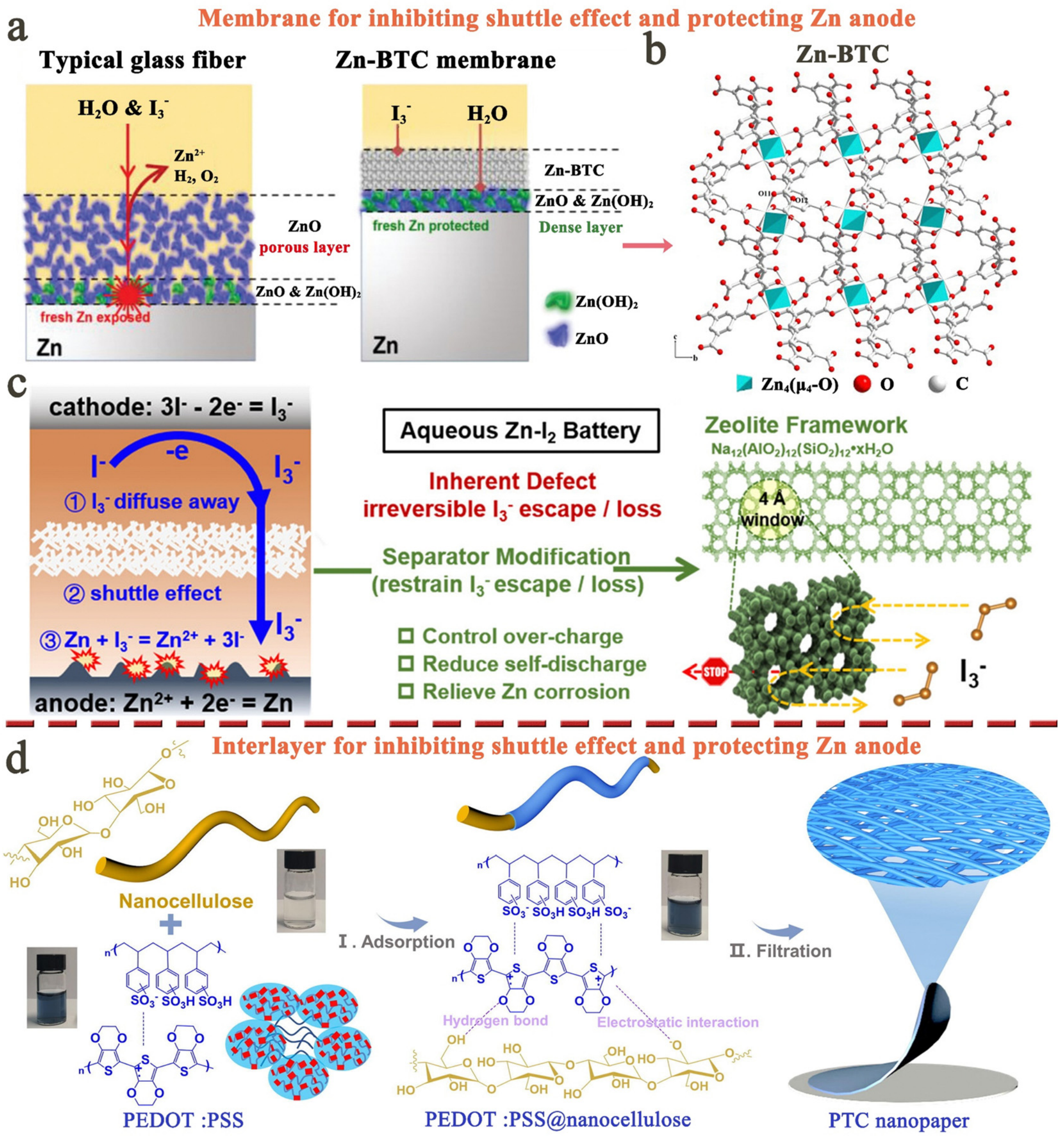

Fig. 15 (a) Schematic illustration for the component evolution of the Zn anode with glass fiber separator and Zn-BTC membrane after being corroded by iodine species and water. Reprinted with permission from ref. 92. Copyright 2020 Wiley. (b) Schematic diagram for the structure of Zn-BTC. Reprinted with permission from ref. 209. Copyright 2008 Elsevier. (c) Schematic illustration for the critical problems in Zn–I_2 batteries and the working mechanism of zeolite molecular sieve. Reprinted with permission from ref. 90. Copyright 2022 American Chemical Society. (d) Schematic diagram of the preparation process of PTC nanopaper. Reprinted with permission from ref. 211. Copyright 2022 Elsevier.

6000 cycles with a capacity retention of 84.6% at 1.92 A g^{-1}. Furthermore, Li *et al.* recently reported a zeolite separator based on a zeolite molecular sieve ($Na_{12}(AlO_2)_{12}(SiO_2)_{12}{\cdot}xH_2O$) to effectively confine the cross-over of soluble I_3^- (Fig. 15c).[90] Since the size of the porous framework (4 Å) inside the zeolite separator is smaller than that of I_3^- ions (5.14 Å), the as-prepared battery can effectively block the uncontrollable diffusion of I_3^-. As a result, the zeolite-based Zn–I_2 battery achieves over 30 000 cycles at 4.0 A g^{-1} with a capacity retention of 91.0%. The cost-effective and easy-to-operate preparation process of the multifunctional zeolite separator makes this work potentially valuable for the construction of advanced Zn–I_2 batteries. In addition, Hou's group also experimented with a single-sided ketone black modified cotton fiber separator, but its performance was relatively poor in a Zn–I_2 cell with 2000 cycles, corresponding to a reversible capacity of 112 mA h g^{-1}.[210] All in all, limited work has been carried out on the modification of Zn–I_2 battery separators. Currently, the design of separators mainly lies in the regulation of pores and surface chemistry. This requires that the separators can facilitate the desolvation of zinc ions (reducing free water molecules) and avoid the passage of polyiodide, while maintaining the high flux of ions.

Interlayers. In contrast to Li–I_2 batteries, research on the interlayer in Zn–I_2 cells is very scarce. Zhang *et al.* reported the first interlayer in Zn–I_2 batteries, namely, the poly(3,4-ethylenedioxythiophene): polystyrene sulfonate (PEDOT: PSS)@nanocellulose

(PTC) interlayer.[211] The advantages of the PTC interlayer are as follows: (1) 3D nanofiber networks with uniformly distributed mesopores allow rapid Zn^{2+} transfer; (2) the abundant polar groups ($-SO_3H$, –S, and –O) enable uniform Zn^{2+} flow, while suppressing polyiodide shuttling through the Coulomb repulsion and chemisorption effect; and (3) the inherent electrical conductivity facilitates homogeneous current distribution (Fig. 15d). Thus, the Zn–I_2 battery presented an ultralong lifespan (>20 000 cycles) at 10 A g^{-1} with a capacity retention of ~72%. It is worth noting that this interlayer does not provide as high of a pseudo-capacitance performance as that found in Li–I_2 batteries. This may be due to the difference in the nature of interlayers (mainly using carbon-based interlayers in Li–I_2 batteries) and cell systems. It is therefore desirable to perform more research on the different interlayers in Zn–I_2 cells to elucidate the working mechanisms and design principles of interlayers.

2.4.1.4 Anodes. It is well known that zinc anodes encounter issues of zinc dendrite growth and hydrogen evolution reaction (HER) in zinc-ion batteries. However, the occurrence of polyiodide shuttling in Zn–I_2 cell also tends to cause corrosion and passivation of the Zn anode, which further aggravates the instability of the Zn electrode.[42,90,92] As revealed by Zhang *et al.*, polyiodide can react with Zn to form water-soluble ZnI_2, which leads to the formation of a honeycomb and bumpy structure on the Zn surface and eventually promotes rampant dendrite growth, causing rapid cell failure.[212] Hence, appropriate strategies should be adopted to protect zinc anodes, such as those used in zinc-ion batteries (optimization of the intrinsic structure of Zn anodes, modification of the anode surface, and so on), for long-lasting Zn–I_2 batteries.[93] Table 13 lists the information and performance of modified anode for Zn–I_2 batteries. In optimizing the bulk structure of zinc anodes, Wang *et al.* first adopted the ZIF-8 MOF annealed at 500 °C (noted as ZIF-8-500) as the host material for zinc, enabling a Zn–I_2 battery to achieve over 1600 cycles (Fig. 16a).[213] However, this strategy focuses on regulating the transfer/reaction of Zn^{2+}, resulting in inadequate prevention of corrosion of the Zn anode by polyiodide, limiting cell stability. Therefore, more efforts have been made by modifying the Zn anode surface to realize high-performance Zn–I_2 cells, as the layer constructed on the Zn surface can serve a dual function of protecting the Zn anode from dendrite growth and HER, as well as inhibiting polyiodide corrosion. For instance, Su *et al.* reported a silicon-based anticorrosion film (Zn@Ts) prepared by the treatment of tetraethyl orthosilicate steam on a Zn disk, which can realize an ultra-long lifetime of 5000 h at 2 mA cm^{-2} (2 mA h cm^{-2}) in a symmetric cell, and 20 000 cycles with a high capacity retention of 93% in a Zn–I_2 full cell.[214] This can be attributed to the fact that the Zn@Ts layer can promote a homogeneous Zn^{2+} flux, protect the Zn anode from aqueous electrolytes, and limit the damage induced by polyiodide to Zn (Fig. 16b and c). Similarly, a series of artificial SEIs were prepared by *in situ* reactions, including Zn@Sn (Zn@tin, prepared using $SnCl_4$),[215] Zn@disordered zinc silicate (Zn@ZSO, prepared using Na_2SiO_3),[216] and phytic acid@Zn layer.[217] Among them, the

Table 13 Modified anodes in Zn–I_2 batteries

1	2	3	4	5	6	7	8	9	10	11
2019	Zn@ZIF-8-500	Anolyte, 0.5 M Li_2SO_4/0.5 M $ZnSO_4$; catholyte, 1 M LiI/0.1 M I_2/0.5 M $ZnSO_4$	KB/PTFE	1 (1)	50	~9.5	1600	97	~117	213
2022	Zinc citrate-derived porous carbon/Zn	2 M $ZnSO_4$	I_2/zinc citrate-derived porous carbon	2 (1)	400	12	3000	88.1	~108	222
2022	Biomass-based lignin layer	Anolyte, 0.5 M Li_2SO_4/0.5 M $ZnSO_4$; catholyte, 1 M LiI/0.1 M I_2/0.5 M $ZnSO_4$	KB/PTFE	2 (2)	650	~28	35 000	99.7	86.7	223
2022	Sn coating layer	2 M $ZnSO_4$	N,P co-doped porous carbon	1 (1)	900	5	1200	90.7	~178	215
2022	Zeolite-based cation-exchange protecting layer	1 M $ZnSO_4$	AC	2.5 (2.5)	460	~9.5	5600	~92	~141.8	219
2022	Disordered zinc silicate artificial SEI	2 M $ZnSO_4$ with 0.05 KI	—	1 (0.25)	2500	~9.5	10 000	—	—	216
2022	Silicon-based films based on tetraethyl orthosilicate	Anolyte, 0.5 M Li_2SO_4/0.5 M $ZnSO_4$; catholyte, 1 M LiI/0.1 M I_2/0.5 M $ZnSO_4$	KB/PTFE	2 (2)	5000	~28	20 000	93	89	214
2022	Phytic acid treated zinc	2 M $ZnSO_4$	N,P co-doped carbon	5 (1)	500	5	5000	93.6	187.7	217
2022	Zincophilic Cu nanocluster	5 mM ZnI_2/10 mM I_2/2 M $ZnSO_4$	ZnI_2/graphene/PVP heterostructure	20 (1)	800 (Zn‖modified Cu cell)	~4.7	200	63.8	~77	218
2023	Reduced graphene oxide	Anolyte, 1 M $ZnSO_4$/0.5 M Na_2SO_4; catholyte, 2 M KI/0.5 M Na_2SO_4	3D functionalized graphene	5 (1)	80	~24	2000	96.7	—	221
2023	Sulfonate-rich ion-exchange fiber layer	2 M $ZnSO_4$	GC-PAN/I	1 (1)	600	~15	6000	90.2	84.6	212
2023	Carboxymethyl chitosan crosslinked gel layer	2 M $ZnSO_4$/0.5 M KI	Adsorptive activated carbon on carbon fiber cloth	1.25 (~0.3)	1300	5 mA cm^{-2}	28 000	100	~1.04 mA h cm^{-2}	220

1, year; 2, anode; 3, electrolyte formula; 4, cathode. Evaluation of Zn‖Zn cell performance: 5, current density (mA cm^{-2}) and areal capacity (mA h cm^{-2}); 6, cycle time (h). Evaluation of Zn–I_2 cell performance: 7, current density (C, 1C = 211 mA h g^{-1}); 8, cycle number; 9, capacity retention (%); 10, reversible capacity (mA h g_{iodine}^{-1}). 11, reference. PTFE, poly tetra fluoroethylene; GC-PAN/I, *N*,*N*′-dimethyl-1,3-propanediamine-grafted, and triethylenetetramine-cross-linked acrylic fiber/iodide.

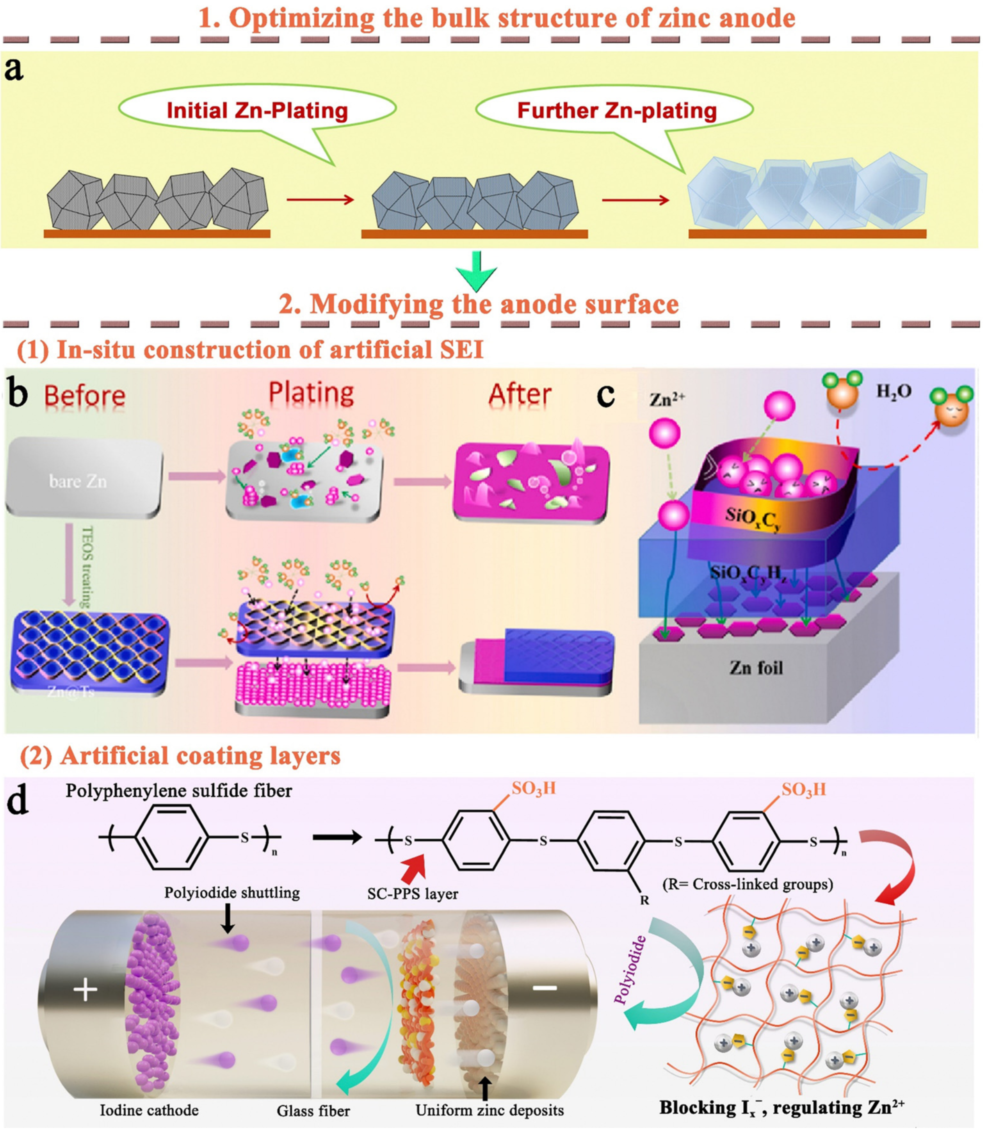

Fig. 16 (a) Schematic illustration for the Zn plating process in the ZIF-8-500@Zn electrode. Reprinted with permission from ref. 213. Copyright 2019 Elsevier. (b) Schematic diagram of the Zn plating/striping behavior on the bare Zn and Zn@Ts electrode, and (c) protection of Zn foil using a silicon-based corrosion protection film. Reprinted with permission from ref. 214. Copyright 2022 Elsevier. (d) Schematic diagram of the brief synthesis process of a sulfonate-rich ion-exchange fiber layer and its role in achieving high performance Zn–I_2 batteries. Reprinted with permission from ref. 212. Copyright 2023 Wiley.

performance of the Zn@ZSO coating layer is optimal, which may be due to the disordered and compact nature of the ZSO interfacial layer that can eliminate grain boundaries inside the interphases, and thus realize excellent plating/stripping reversibility of Zn^{2+} (2500 h at 1 mA cm^{-2} (0.25 mA h cm^{-2})).[216] In addition, Rei *et al.* proposed a novel approach for achieving uniform Zn deposition, that is, the utilization of Cu foil with *in situ* formed zincophilic Cu nanoclusters (prepared by treatment with trace amounts of I_3^- additives in the electrolyte) as an anode for current collection.[218] In fact, however, these Cu nanoclusters cannot prevent the corrosion of zinc by polyiodide, thus leading to the short lifetime of the as-fabricated Zn–I_2 cell (63.8% capacity retention after 200 cycles). Therefore, the protection strategies for Zn anodes should focus on improving the ability of Zn to resist polyiodide corrosion. On the other hand, some artificial coating layers, including zeolite-based cation-exchange,[219] sulfonate-rich ion-exchange fibers,[212] carboxymethyl chitosan cross-linked gel,[220] RGO,[221] zinc citrate-derived porous carbon,[222] and biomass-based lignin layers,[223] were also presented. Among them, the layers with ion exchange mechanisms generally had excellent properties (≥5000 cycles). This is because the negatively-charged groups/cavities in these materials can provide uniform and rapid flux of Zn^{2+}, while preventing the penetration of polyiodide into the Zn anode through electrostatic repulsion (Fig. 16d). Thus, the resulting Zn–I_2 battery by Lai's group can work over 6000 cycles with a high capacity retention of 90.2% at 3.2 A g^{-1}.[212] Apart from these methods, the aforementioned high-concentration salt electrolytes, gel electrolytes, and modified separators can not only effectively protect the zinc anode, but also avoid the free migration of polyiodide.

All in all, the protection of the zinc anode for Zn–I_2 batteries should include the following aspects: (1) inhibiting the growth of zinc dendrites; (2) avoiding hydrogen evolution reaction; and (3) preventing polyiodide from migrating to the zinc anode. Modification of the anode surface has been proven to be effective in achieving these objectives, which generally involves two strategies, namely, *in situ* construction of artificial SEIs and coating layers by spin/scrape-coating. The advantage of the former lies in the ability to form uniform and strongly adherent layers, while the latter is easier to prepare on a large scale.[224] Despite this, some design recommendations for modified layers can be described as follows: (1) rich in negative charges, which can regulate the transfer/reaction of Zn^{2+} and polyiodide through electrostatic interaction; (2) a uniform pore structure, which can result in a homogeneous and rapid Zn^{2+} flux; (3) zincophilic properties to reduce the overpotential of the Zn plating/stripping process; and (4) a disordered interphase to eliminate grain boundaries inside the interphases. Based on these guidelines, extensive efforts are desired in future to advance the Zn anode toward high stability.

2.4.2 Zinc–iodine flow batteries. While Zn–Br_2 flow battery systems are currently available for commercial use, there are also several unique advantages offered by Zn–I_2 flow batteries (ZIRFBs), including low vapor pressure and toxicity, a high solubility of ZnI_2 (∼7 M)/I_3^- (∼8 M), a suitable redox potential (1.3 V to avoid water decomposition), and excellent redox kinetics.[16,125,163] Therefore, the ZIRFB is a promising choice in developing high energy density, low-cost, eco-friendly, and large-scale grid energy storage devices. However, ZIRFBs still encounter various challenges, such as low utilization of iodine and the shuttle effect. Therefore, electrolyte engineering, cathode/separator modification strategies have been proposed to overcome these problems (see Table 14 for detailed battery performance), which will be discussed in detail, as follows.

2.4.2.1 Electrolyte. Electrolyte engineering has become a mainstream research interest in developing high-performance ZIRFBs, as the iodine-active species in ZIRFBs are stored in electrolytes. By using a near-neutral 5.0 M ZnI_2 electrolyte, Li *et al.* pioneered the preparation of high energy density ZIRFBs.[16] However, only two-third of iodine is utilized in this system, because one-third of I^- ions is coordinated to I_2 to form I_3^-, resulting in this portion of iodine not being utilized for energy conversion. To address this issue, various electrolyte additives such as NH_4Br,[225] NH_4Cl,[226] and $ZnBr_2$,[227] were introduced to promote the formation of I_2 and improve iodine utilization. This is because Br^- and Cl^- ions can stabilize free iodine by forming I_2Br^- and I_2Cl^- ($2I^- + Br^- \leftrightarrow I_2Br^- - 2e^-$, $E^0 = 0.594$ V *vs.* SHE; $2I^- + Cl^- \leftrightarrow I_2Cl^- - 2e^-$, $E^0 = 0.61$ V *vs.* SHE) respectively, thereby releasing iodide ions for charge storage (Fig. 17a).[226,227] Additionally, the introduction of NH_4^+ ions was also effective in mitigating the growth of zinc dendrites due to the electrostatic shielding effect formed by the

Table 14 Electrochemical performance, fabrication parameters, and cell-testing conditions for Zn–I_2 flow batteries from 2015 to 2023

1	2	3	4	5	6	7	8	9
2015	GF	3.5 M ZnI_2 (—)	3.5 M ZnI_2 (—)	Nafion 115	10	40	∼80	16
2016	MIL-125-NH_2-modified GF	2.5 M ZnI_2 (—)	2.5 M ZnI_2 (—)	Nafion 115	30	45	64	239
2016	UiO-66-CH_3-modified GF	2.5 M ZnI_2 (—)	2.5 M ZnI_2 (—)	Nafion 115	30	50	∼64	239
2017	GF	5 M ZnI_2 + 2.5 M $ZnBr_2$ (1 mL)	5 M ZnI_2 + 2.5 M $ZnBr_2$ (1 mL)	Nafion 117	10	20	—	227
2018	GF	6 M KI/3 M $ZnBr_2$ (50 mL)	6 M KI/3 M $ZnBr_2$ (50 mL)	Porous polyolefin membrane	80	1000	80	231
2018	Graphite foil	6 M KI/6 M I_2 (10 mL)	6 M KOH (—)	Nafion 117	10	70	80	164
2019	MoS_2-modified GF	2 M ZnI_2 (2.5 mL)	2 M ZnI_2 (2.5 mL)	Nafion 115	40	45	∼67.9	238
2019	Carbon felt	1.5 M NaI, 0.5 M $ZnCl_2$, 1.0 vol% PEG200, 0.15 vol% HCl, 20 vol% PC (—)	1.5 M NaI, 0.5 M $ZnCl_2$, 1.0 vol% PEG200, 0.15 vol% HCl, 20 vol% PC (—)	Durapore membrane	20	50	∼65	229
2019	GF	7.5 M KI/3.75 M $ZnBr_2$ (7.2 mL)	7.5 M KI/3.75 M $ZnBr_2$ (—)	Polyolefin separator with 250 μm Nafion layer	20	100	∼80	232
2020	Heat-treated GF	6.5 M NH_4I/1.5 M NH_4Cl (10 mL)	3.25 M $ZnCl_2$/1.5 M NH_4Cl (—)	Nafion 117	10	2500	80	226
2020	GF	0.5 M KI/0.5 M I_2 (15 mL)	1 M $ZnSO_4$ (15 mL)	CMC/PVA polyelectrolyte membrane	10	300	—	234
2021	GF	1 M NH_4Br/1 M ZnI_2 (—)	1 M NH_4Br/1 M ZnI_2 (—)	Nafion 115	40	100	85	225
2021	Heat-treated GF	5 M NH_4I/2.5 M NH_4Cl (—)	2.5 M $ZnCl_2$/2.5 M NH_4Cl (—)	Daramic microporous polyethylene separators	80	1100	—	237
2021	GF	6 M KI with 5.3 wt% PVP (—)	0.5 M $ZnCl_2$/3 M KCl (—)	Perfluorinated sulfonic acid membrane	20	600	70	230
2022	GF	2 M KCl/0.5 M $ZnBr_2$/1 M KI (10 mL)	2 M KCl/0.5 M $ZnBr_2$/1 M KI (10 mL)	Chitosan-starch composite membrane	80	200	77.4	233
2022	GF	1 M ZnI_2 + 7.5% ACN (—)	1 M ZnI_2 + 7.5% ACN (—)	Nafion 115	100	170	∼60	228
2023	CNT with iron particles	1 M KI/0.5 M $ZnBr_2$/1 M KCl (—)	1 M KI/0.5 M $ZnBr_2$/1 M KCl (—)	Nafion 212	17	60	∼60	240

1, year; 2, cathode; 3, catholyte (volume of electrolyte); 4, anolyte (volume of electrolyte); 5, membrane. Evaluation of Zn–I_2 cell performance: 6, current density (mA cm^{-2}); 7, cycle number; 8, energy efficiency (%); 9, reference. MIL-125-NH_2, $Ti_8O_8(OH)_4[(O_2C{-}C_6H_5{-}CO_2)]_6$; UiO-66-$CH_3$, $(Zr_6O_4(OH)_4[O_2C{-}C_6H_2(CH_3)_2{-}CO_2]_6$; ACN, acetonitrile; GF, graphite felt; CMC/PVA, carboxymethyl cellulose/polyvinyl alcohol.

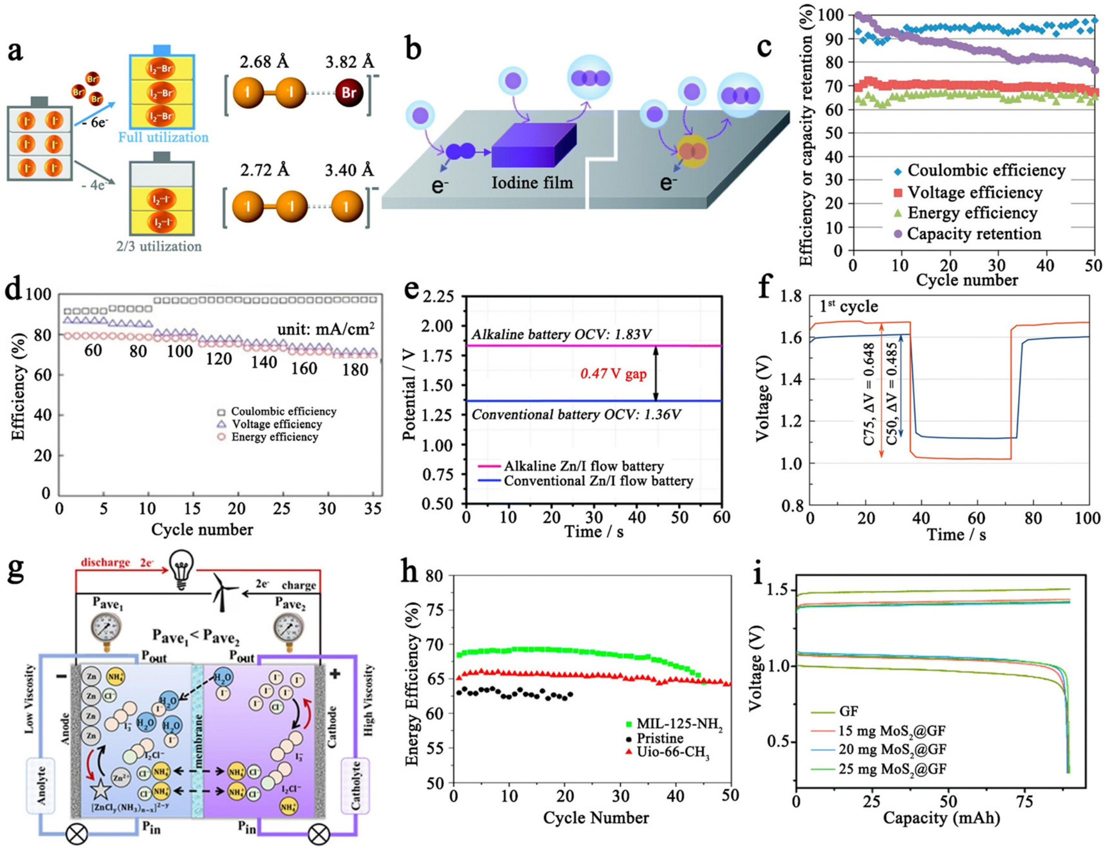

Fig. 17 (a) Schematic representation of Br^- ions as complexing agents for iodine stabilization. Reprinted with permission from ref. 227. Copyright 2017 Royal Society of Chemistry. (b) The working mechanisms of I^- to I_3^- transition without (left) and with (right) a cosolvent in an aqueous solution. Reprinted with permission from ref. 228. Copyright 2022 Royal Society of Chemistry. (c) Efficiencies of ZIRFB at 20 mA cm^{-2} with the electrolyte of 1.5 M NaI, 0.5 M $ZnCl_2$, 1.0 vol% PEG200 (polyethyleneglycoland), and 0.15 vol% HCl with 20 vol% propylene carbonate. Reprinted with permission from ref. 229. Copyright 2019 Elsevier. (d) Rate capability of ZIRFB with an electrolyte of 2 M KI + 1 M $ZnBr_2$. Reprinted with permission from ref. 231. Copyright 2018 Wiley. (e) Open-circuit voltage of conventional and designed alkaline ZIRFBs. Reprinted with permission from ref. 164. Copyright 2018 Royal Society of Chemistry. (f) Polarization voltage curves for C50 (CMC : PVA = 50 : 50 wt%) and C75 (CMC : PVA = 75 : 25 wt%) cells show decent performance and cycling stability)at 10 mA cm^{-2} for the first cycle. Reprinted with permission from ref. 220. Copyright 2022 Elsevier. (g) Schematic diagram of ion convection caused by unbalanced hydraulic pressure in a ZIRFB. Reprinted with permission from ref. 237. Copyright 2021 Elsevier. (h) Cycling performance of ZIRFBs with the pristine graphite felt and the MOF-modified graphite felt electrodes. Reprinted with permission from ref. 239. Copyright 2016 American Chemical Society. (i) Charge–discharge curves of the pristine graphite felt, and the MoS_2-modified graphite felt electrodes at 30 mA cm^{-2}. Reprinted with permission from ref. 238. Copyright 2019 Royal Society of Chemistry.

complexation of NH_4^+ ions with Zn^{2+} ions ($Zn^{2+} + xNH_4^+ + yCl^- \leftrightarrow [Zn(NH_3)_xCl_y]^{2-y} + xH^+$).[226] As a result, the ZIRFB with a catholyte of 6.5 M NH_4I/1.5 M NH_4Cl can achieve a long cycle life of 2500 cycles at 10 mA cm^{-3}, with an energy efficiency of ~80% and an energy density of 137 W h L^{-1}.[226] On the other hand, the insolubility and electrical insulating properties of solid I_2 in water can lead to the formation of iodine films during the cycling process, which not only blocks the pore structure of electrodes but also impedes the iodine redox process (Fig. 17b). As revealed by Zhao *et al.*, the rate constant for the transition from I_2 to I_3^- was only 10^{-6} mol (cm^{-2} s^{-1}).[228] To accelerate electrode kinetics, organic electrolyte additives such as propylene carbonate,[229] acetonitrile,[228] and polyvinylpyrrolidone[230] were added to solubilize the iodine film. Indeed, the current density of ZIRFBs can reach up to more than 100 mA cm^{-2} when 1 M ZnI_2 + 7.5 vol% acetonitrile is employed as the electrolyte.[228] Despite this, the introduction of these organic solvents increased the risk of electrolyte cross-contamination, leading to low cell Coulombic efficiency (Fig. 17c). An alternative to these organic additives is KI, which is able to promote iodine solubility and simultaneously supply iodine ions.[231,232] As shown in Fig. 17d, the ZIRFB can operate at a high current density of 180 mA cm^{-2} with an electrolyte of 2 M KI + 1 M $ZnBr_2$.[231] Furthermore, Zhang *et al.* attempted to increase the energy density of ZIRFBs by using an alkaline anolyte (containing 6 M KOH), which can lower the redox potential of zinc anodes to −1.26 V ($Zn + 4OH^- - 2e^- \rightarrow Zn(OH)_4^{2-}$, $E^0 = -1.260$ V), thereby increasing the overall voltage of the ZIRFB to 1.796 V ($Zn + I_3^- + 4OH^- \rightarrow Zn(OH)_4^{2-} + 3I^-$, $E^0 = 1.796$ V) (Fig. 17e).[164] Although the as-prepared ZIRFB exhibited a high-energy-density of 330.5 W h L^{-1}, the battery demonstrated a short life of 70 cycles at 10 mA cm^{-2} due to the cross-contamination of $Zn(OH)_4^{2-}$, I_3^-, and I^-, as well as severe zinc dendrite growth and corrosion. Besides, the irreversible disproportionation reaction of iodine with OH^- ($6OH^- + 3I_2 \rightarrow 5I^- + IO_3^- + 3H_2O$) should also be considered. Therefore, the feasibility of using alkaline anolytes still requires critical assessment. Overall, the current development of electrolyte engineering is centered on the following areas, including the realization of the I^- to I_2 process, the promotion of iodine film dissolution, and the exploration of alkaline anolytes.

2.4.2.2 Separators. The cross-diffusion of soluble iodine species between the cathode and anode is recognized as a key challenge that hampers the advancement of ZIRFBs, as it can lead to severe self-discharge in batteries. Therefore, cation exchange membranes (*e.g.*, Nafion membrane) have become an essential component of ZIRFBs to prevent cross-contamination of iodine species. Nonetheless, these ion exchange membranes are costly, typically accounting for 40% of the overall stack cost for flow batteries.[233] This leads to the necessity of developing economical, highly selective, high-flux, and stable ion exchange membranes. In this regard, Tangthuam's group has attempted to develop a polyelectrolyte membrane consisting of carboxymethyl cellulose compounded with polyvinyl alcohol.[234] Unfortunately, the membrane exhibited unsatisfactory performance, with a polarization voltage as high as 0.648 V (Fig. 17f). In view of this, Gao *et al.* successfully achieved a high-performance and low-cost ion-exchange membrane based on the "host–guest" chemistry between the membrane and iodine species.[233] Specifically, they utilized a starch–chitosan complex as a host to confine iodine species (guest). This choice was motivated by the following reasons: (1) starch is one of the most abundant natural polymers with a cheap price ($\sim$\$0.3 kg^{-1}); (2) starch possesses an internal hydrophobic cavity ($\sim$5 Å in diameter) that can interact with iodine species *via* host–guest chemistry; and (3) chitosan can prevent starch from dissolving in water through hydrogen bonding, while its rich –OH groups facilitate interaction with iodine species and inhibit the shuttle effect. Consequently, the proof-of-concept membranes enabled ZIRFBs to be cycled for 200 cycles at 60 mA cm^{-3} without a significant capacity loss. However, it should be noted that the method based on the adsorption of iodine species by the membrane to prevent cross-contamination may result in the accumulation of iodine species within the membrane and eventual blockage of the membrane. Therefore, Donnan exclusion and size exclusion strategies are two main strategies for achieving high-performance ion exchange membranes.[235,236] For example, in zinc–iodine static cells, long-cell cycling was often achieved by altering the charge properties of membranes and controlling their pore size.[90,92] Nevertheless, research on membranes for ZIRFBs remains limited due to the excellent performance of commercially available Nafion membranes, although their high cost is a consideration. In addition, Mousavi *et al.* found that the increased viscosity and density of catholytes during battery cycling can result in elevated pressure within the cathode chamber of ZIRFBs (Fig. 17g).[237] This will induce the transfer of iodine species from the cathode to the anode, leading to a significant decrease in cell capacity. An effective strategy to alleviate this problem is to maintain a balanced hydraulic pressure by adjusting the flow rate ratio of electrolytes (catholyte : anolyte = 1 : 7), thereby avoiding convection of iodine species.

2.4.2.3 Cathodes. Generally, ZIRFB cathodes are mainly composed of graphite felts due to their high porosity (>90%), low cost, and excellent conductivity. However, the ZIRFBs exhibit limited energy efficiency at high current densities due to the sluggish redox kinetics of the I_3^-/I^- process on the graphite felt surface. Therefore, some materials with electrocatalytic functions (*e.g.*, MOFs and MoS_2) have been employed to modify graphite felts.[238,239] Among them, MOFs have been considered promising candidates for advanced adsorbents and catalysts because of their extraordinary surface area, tunable pore geometries, and diverse chemical compositions. Therefore, Li *et al.* explored the use of two MOF materials, including MIL-125-NH_2 ($Ti_8O_8(OH)_4[(O_2C–C_6H_5–CO_2)]_6$) and UiO-66-$CH_3$ ($Zr_6O_4(OH)_4[O_2C–C_6H_2(CH_3)_2–CO_2]_6$), loaded on graphite felts as electrocatalysts to accelerate the I^-/I_3^- redox reaction.[239] As a result, both MIL-125-NH_2 and UiO-66-CH_3 modified graphite felts exhibited improved energy efficiency compared to pristine graphite felts, with energy efficiency values increasing by approximately 6.4% and 2.7%, respectively, at 30 mA cm^{-2}. This enhancement can be attributed to two factors: (1) the Lewis acid sites in the MOFs can act as catalytic sites to accelerate electron transfer and (2) the weaker Lewis acid sites in MIL-125-NH_2 compared to UiO-66-CH_3 facilitate the dissociation of electrons from the Ti atoms in MIL-125-NH_2, thus better facilitating the iodine conversion reaction. Nevertheless, the poor chemical stability of MOFs is the major obstacle limiting its development, as UiO-66-CH_3-modified graphite felts (good stability but poor catalytic performance) only proved to be stable for about 50 cycles (Fig. 17h). To overcome this limitation, Liu *et al.* sought to accelerate the iodine redox reaction using the defect engineering strategy. MoS_2, which possesses a unique layered structure and semiconducting properties, was chosen as the electrocatalyst and *in situ* grafted onto the graphite felt surface.[238] The resulting ZIRFB with a MoS_2-modified graphite felt electrode showed higher energy efficiency (10.2%) compared to pristine graphite felts at 30 mA cm^{-2} (Fig. 17i). The excellent catalytic performance of MoS_2 nanoplates can be attributed to three key factors: (1) the abundant defects (*e.g.*, S vacancies) on the MoS_2 nanoplates result in excellent catalytic activity; (2) the introduction of active S edges and S ligands in the MoS_2 nanoplates provides more active sites than in pristine MoS_2; and (3) the MoS_2 nanoplates have vertically aligned distributions on the graphite felt surface which facilitates electrolyte diffusion. In addition to the modified graphite felt, Williams *et al.* also utilized carbon nanotubes with redox-active iron particles as the electrode, which aligns with the single-atom catalytic strategy employed in static batteries.[240] However, this does not mean that the cathode strategies for static and liquid zinc–iodine batteries are highly generalizable. In static cells, the cathode needs to retain iodine species within the electrode as much as possible to avoid shuttle effects, whereas, in liquid-flow cells, the cathode requires high porosity for efficient iodine species mobility instead of high iodine retention ability. Nonetheless, the acceleration of the iodine conversion process by introducing electrocatalysts remains highly similar in both types of cells. Thus, the power density of a ZIRFB with an iron-functionalized carbon electrode can be increased by 66% compared to a ZIRFB with inert carbon. In general, the key to the cathode design of ZIRFBs lies in

Table 15 Fe–I_2 batteries

1	2	3	4	5	6	7	8	9	10
2020	Modified Fe powder with ascorbic acid	1 M $FeSO_4$	I_2/N-doped hierarchically porous carbon	~2	2 A g^{-1}	550	100	—	19
2022	Fe foil	5 M $FeCl_2$/1 M $ZnCl_2$	Polyaniline	—	8 mA cm^{-2}	1200	99.8	—	61

1, year; 2, anode; 3, electrolyte formula; 4, cathode; 5, iodine loading (mg cm^{-2}). Evaluation of Fe–I_2 cell performance: 6, current density; 7, cycle number; 8, capacity retention (%); 9, reversible capacity (mA h g_{iodine}^{-1}). 10, reference.

catalyzing the iodine conversion process for reducing battery polarization and promoting efficient utilization of iodine.

2.5 Iron–iodine batteries

The Fe–I_2 battery section of Table 15 provides the relevant battery information and performance. Fe metal is the most abundant transition metal in the Earth's crust, and the most mass-produced metal commodity.[241,242] Its two-electron transfer (Fe^{2+}/Fe, −0.447 V *vs.* SHE) can provide specific and volumetric capacities of 958 mA h g^{-1} and 7530 mA h cm^{-3}, respectively.[61] All these advantages lead to the emergence of Fe–I_2 batteries. In 2020, Bai *et al.* constructed a Fe–I_2 battery using a I_2@nitrogen-doped hierarchically porous carbon (N-HPC) composite as the cathode, modified Fe powder as the anode, and 1 M $FeSO_4$ in aqueous solution as the electrolyte.[19] The resulting battery exhibited 550 cycles with ~100% capacity retention at 2 A g^{-1}, demonstrating the feasibility of Fe–I_2 batteries. However, the sudden failure of the battery at high-capacity retention and short cycle life suggests serious instability issues like dendrite growth and side reactions with aqueous electrolytes in the Fe anode. Wu *et al.* further improved the reversibility and stability of the Fe plating/stripping process by doping Zn into the Fe anode.[61] In other words, the positively charged $[ZnI]^+$ complexes introduced by adding ZnI_2 to $FeCl_2$ electrolytes, can adsorb on the negatively charged surface of Fe metal, thereby realizing the doping of Zn into the Fe lattice during deposition (Fig. 18a). With Zn doping, Fe^{2+} will deposit as homogeneous small particles, since its (110) plane is preferably grown parallel to the substrate. Accordingly, the lifespan of the Fe anode is greatly extended to over 2500 h at 1 mA cm^{-2} (1 mA h cm^{-2}). When combined with the frequently used PANI cathode, the battery showed over 1200 cycles with a capacity retention of 99.8% at 8 mA cm^{-2}, which is promising for large-scale energy storage applications (Fig. 18b). However, a relatively low CE of the cell is also caused by the introduction of ZnI_2 additives. In addition, due to the relatively low potential of iron itself, the discharge plateau of the Fe–I_2 battery is below 0.9 V (Fig. 18c). Despite this, owing to the unique advantages of Fe metal in terms of cost and abundance, Fe–I_2 batteries have opportunities for large-scale energy storage applications. In general, research on Fe–I_2 batteries should place more emphasis on expanding the basic understanding of Fe plating/stripping chemistry in aqueous solution, as it occupies the "short slab" position in battery performance, particularly with the rapid advancements in iodine cathodes.

2.6 Aluminum–iodine batteries

The section on Al–I_2 batteries in Table 16 presents pertinent performance data. Al has been exploited as an electrode material for batteries since the 1850s. This can be ascribed to its abundant availability, low cost, high theoretical capacity of 2980 A h kg^{-1}, and deep standard electrode potential of 1.66 V (*vs.* SHE).[243] Despite its advantages, in aqueous systems, the formation of a passive oxide film, corrosion, and the hydrogen evolution reaction in an aqueous environment limit the electrochemical reversibility of Al, seriously retarding its practical wide application.[63,244] The development of novel electrolytes has historically been crucial for battery technology advancement.[77] Recent research has shown that Al anodes can show high reversibility in $Al_2Cl_7^-$-containing ionic liquids with apparently little dependence on solution composition.[63,244] In this regard, Tian *et al.* successfully created an initial rechargeable Al–I_2 battery using a PVP–I_2 complex as the cathode and a room-temperature ionic liquid-based electrolyte (mixing $AlCl_3$ with 1-ethyl-3-methylimidazolium chloride at a molar ratio of 1.3 : 1). The resulting Al–I_2 battery provided a high capacity of >200 mA h g^{-1} at 0.2C and over 150 cycles at 1C. Nevertheless, due to PVP's inadequate iodine species adsorption and low conductivity, battery capacity and lifespan were jeopardized. Therefore, Zhang *et al.* further integrated active carbon cloth and PVP–I in the cathode, resulting in a long-term life of Al–I_2 batteries with a capacity of 102.7 mA h g^{-1} after 1050 cycles at 1C (Fig. 18d).[78] These findings prove that Al–I_2 batteries hold promise for future development. Unfortunately, although the conversion-type iodine cathode is able to bypass the difficult dissociation and solid-state diffusion of Al^{3+} cations in intercalation-based electrode materials, the battery still suffers from sluggish electrochemical kinetics (<1C) and large battery polarization (>0.2 V) (Fig. 18e).[63] This may be due to the slow transport of Al^{3+} cations within the bulk electrode as well as in the electrolyte.[245] Meanwhile, the intense electrostatic interaction between the charge-rich Al^{3+} cation and iodine lattices could be another potential issue in limiting the rapid charging/discharging process.[246] All in all, in-depth research on viable electrolytes is urgently needed to achieve high reversibility of aluminum anodes while maintaining high migration rates of Al^{3+} cations.

2.7 Magnesium–iodine batteries

The Mg–I_2 battery section of Table 17 provides the relevant battery information and performance. Mg metal possesses a deep redox potential (−2.37 V *vs.* SHE), high abundance (1.5 wt% in Earth's crust), and high theoretical volumetric energy density (3833 mA h cm^{-3}).[66,247] Particularly, Mg does not deposit into detrimental morphologies in most electrolyte solutions, making Mg-based batteries safer than other batteries.[63,64] Similar to Al-based batteries, however, the fatal problem for Mg-based batteries is the Mg anode that has a strong tendency to form

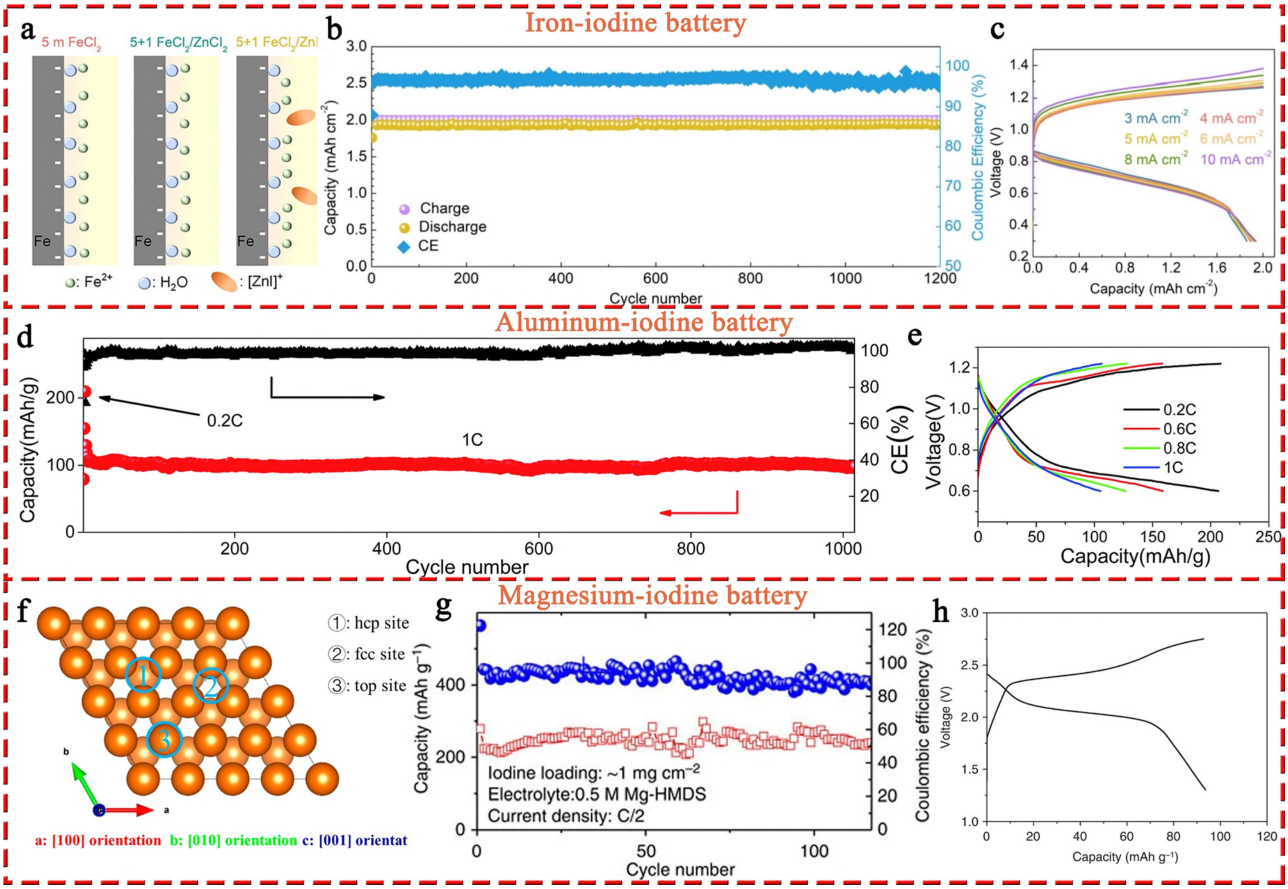

Fig. 18 (a) Schematic illustration for the surface species of Fe electrodes in 5 M $FeCl_2$, 5 M $FeCl_2$ + 1 M $ZnCl_2$, and 5 M $FeCl_2$ + 1 M ZnI_2 electrolytes. Electrochemical performance of the Fe–I_2 battery using the 5 M $FeCl_2$ + 1 M ZnI_2 aqueous electrolyte and the PANI@iodine cathode: (b) long-term cycling performance at 8 mA cm^{-2}, and (c) galvanostatic charge/discharge curves at different current densities. Reprinted with permission from ref. 61. Copyright 2021 Elsevier. Electrochemical performance of the Al–I_2 battery with an active carbon cloth@PVP cathode: (d) long-term cycling performance at 1C, and (e) typical galvanostatic charge/discharge curves at different current densities. Reprinted with permission from ref. 78. Copyright 2018 Royal Society of Chemistry. (f) The typical adsorption sites of iodine on the Mg(0001) surface. Reprinted with permission from ref. 249. Copyright 2018 American Chemical Society. (g) Cycling stability of the Mg–I_2 battery with the active carbon cloth@I_2 cathode at 0.5C. (h) The typical discharge/charge curves of the Mg–I_2 battery with a microporous carbon@iodine cathode at 0.25C. Reprinted with permission from ref. 66. Copyright 2017 Springer Nature.

Table 16 Al–I_2 batteries

1	2	3	4	5	6	7	8	9	10
2017	Al foil	$AlCl_3$/1-ethyl-3-methylimidazolium chloride (1.3 : 1, m/m)	PVP–I_2	1.2	1	150	100	—	25
2018	Al foil	$AlCl_3$/1-ethyl-3-methylimidazolium chloride (1.3 : 1, m/m)	Active carbon cloth/PVP–I_2	—	1	1050	—	102.7	78

1, year; 2, anode; 3, electrolyte formula; 4, cathode; 5, iodine loading (mg cm^{-2}). Evaluation of Al–I_2 cell performance: 6, current density (C, 1C = 211 mA g^{-1}); 7, cycle number; 8, capacity retention (%); 9, reversible capacity (mA h g_{iodine}^{-1}). 10, reference.

Table 17 Mg–I_2 batteries

1	2	3	4	5	6	7	8	9	10
2017	Mg foil	$(HMDS)_2Mg/AlCl_3/MgCl_2$ in TEGDME	Active carbon cloth/I_2	1	0.5	120	94.6	∼180	66
2022	Mg foil	$(HMDS)_2Mg/AlCl_3/MgCl_2$ in TEGDME	PVP–I_2	∼0.5	0.8	500	90	—	76

1, year; 2, anode; 3, electrolyte formula; 4, cathode; 5, iodine loading (mg cm^{-2}). Evaluation of Mg–I_2 cell performance: 6, current density (C, 1C = 211 mA g^{-1}); 7, cycle number; 8, capacity retention (%); 9, reversible capacity (mA h g_{iodine}^{-1}). 10, reference. $(HMDS)_2Mg$, magnesium bis(trimethylsilyl)amide.

insulating and passivating surface layers in most environments, which would block internal electrochemical reactions kinetically.[64,65,248] Based on simulations and calculations, Liu *et al.* revealed that the Mg(0001) surface can provide strong chemical bonding interaction for I_2 molecules, leading to the dissociation and reduction of I_2 to I^- anions under a low iodine coverage condition (Θ = 12.5%) (Fig. 18f).[249] However, in contrast to Li, when the iodine coverage is increased to 100%, the Mg surface exhibits good resistance to surface iodization without iodide exfoliation.[137] This indicates that the Mg anode could have good resistance to iodization-induced corrosion and self-discharge. Typically, the development of new-type electrolytes can effectively result a highly stable and reversible Mg anode. For example, Bertasi *et al.* proposed a new iodoaluminate ionic liquid-based electrolyte prepared by reacting 1-ethyl-3-methylimidazolium iodide with AlI_3 in a 1 : 1 molar ratio.[21] They suggested that a 2.9 V Mg–I_2 secondary battery could be realized by coupling the ionic liquid-based electrolyte with an Mg anode, although the performance of the relevant battery was not presented. Fortunately, Tian *et al.* realized a rechargeable Mg–I_2 battery by using activated carbon cloth@iodine as the cathode, and magnesium bis(trimethylsilyl)amide with aluminum chloride and magnesium chloride in tetraglyme as the electrolyte.[66] The resulting Mg–I_2 battery exhibited a high capacity retention of 94.6% after 120 cycles at a rate of 0.5C (Fig. 18g). In addition, Zhang *et al.* further realized over 500 cycles at 800 mA h g^{-1} with a decay rate of 0.18% per cycle in a Mg–I_2 cell based on a PVP–I cathode, as the shuttle effect was effectively mitigated by the chemical interaction between iodine and PVP.[76] The successful application of common iodine cathodes, such as PVP/I and carbon cloth@iodine, proves the feasibility of Mg–I_2 batteries. Among the multivalent MIBs, the Mg–I_2 battery holds a special position with the highest discharge plateau at ~2.4 V, indicating its high energy density (Fig. 18h). Considering the advantages of affordability and abundant resources of Mg metal, Mg–I_2 could have a broad application value in large-scale energy storage applications. Nonetheless, Mg–I_2 batteries are still in the early stages of development due to the issues of magnesium anodes. Normally, the passivation layer formed on the Mg surface during electrodeposition would block the associated electrochemical reactions and Mg^{2+} diffusion channels at room temperature. In addition, the strong electrostatic interaction generated by the high charge density of Mg^{2+} cation also leads to sluggish kinetics inevitably. However, with the development of novel electrolytes that can resolve the stability and reversibility issues of Mg anodes, Mg–I_2 batteries have high potential due to their advantages of cost-effectiveness, high energy density, and the absence of intercalation/deintercalation processes.

3 Advanced calculation and characterization in metal–iodine batteries

The primary focus of this review is on the material design of metal–iodine batteries (MIBs). However, it is also essential to provide a concise overview of advanced characterization and computational methods commonly employed in MIBs. These methods play a crucial role in bridging the gap between experimental findings and results, promoting the understanding and development of MIBs.

3.1 Advanced calculation methods

Throughout history, computational chemistry has emerged as an indispensable tool for interpreting experimental results, predicting intrinsic properties, and investigating new chemical phenomena.[250] In the realm of MIBs, various calculation methods have been developed, including density functional theory (DFT) calculations, molecular dynamics (MD) simulation, and finite element analysis. Here, we present a summary of their typical applications in the context of MIBs.

3.1.1 Density functional theory. (1) Adsorption energy calculation. This represents one of the fundamental applications of computational chemistry in MIBs. By calculating the adsorption energy between iodine species and different groups or conformations, the strength of the interaction between materials and iodine species can be assessed accurately. Furthermore, these results can provide explanations for experimental phenomena, facilitate optimization of material design, and help identify active sites. For instance, Sun *et al.* utilized DFT calculations to determine the adsorption energies of iodine at various adsorption sites (–F, –O, and –OH) on the surface of $Ti_3C_2T_x$ MXene.[23] The obtained results revealed that the binding energies of –F, –O, and –OH functional groups in $Ti_3C_2T_x$ MXene were −0.32, −0.97, and −3.68 eV, respectively. This implies that $Ti_3C_2T_x$ MXene interacts strongly with iodine, while the –OH group serves as the primary active site. (2) State of charge/electron analysis. An effective approach for investigating the electron transfer and charge distribution of iodine species within materials is through differential charge density analysis. This method enables the visualization of electron flow after the interaction between iodine species and individual fragments or groups in materials. Importantly, it is often employed in conjunction with adsorption energy calculations to understand the interactions between materials and iodine species comprehensively. Fig. 19a illustrates the charge-density-difference models, providing a clear insight into the interactions between the CH_6N^+ (methylamine hydroiodide) group and various iodine species (I^-, I_2, and I_3^-).[53] By considering the adsorption energies between iodine species and CH_6N^+ ($CH_6N^+I^-$: −5.38 eV; $CH_6N^+I_2$: −5.08 eV; and $CH_6N^+I_3^-$: −7.36 eV), the strong interactions between the materials and iodine species can be effectively demonstrated (Fig. 19b). On the other hand, the electron localization function (ELF) allows for an analysis of the bond type and distribution of lone pair electrons in iodine species, providing insights into the stability of redox products. Its upper limit of 1 indicates complete electron localisation, while the lower limit of 0 refers to complete electron delocalisation. As shown in Fig. 19c, the ELF model elucidated that the electrical coupling between Cl^- and I^+ is more stable in I–Cl compared to I–Cl_2.[18] Additionally, density of states (DOS) calculations are capable of examining the impact of active sites on the iodine electron orbitals. For example, Liu *et al.* employed partial DOS to evaluate the interaction between various active centers and iodine.[183] As shown in Fig. 19d, the d-band center of

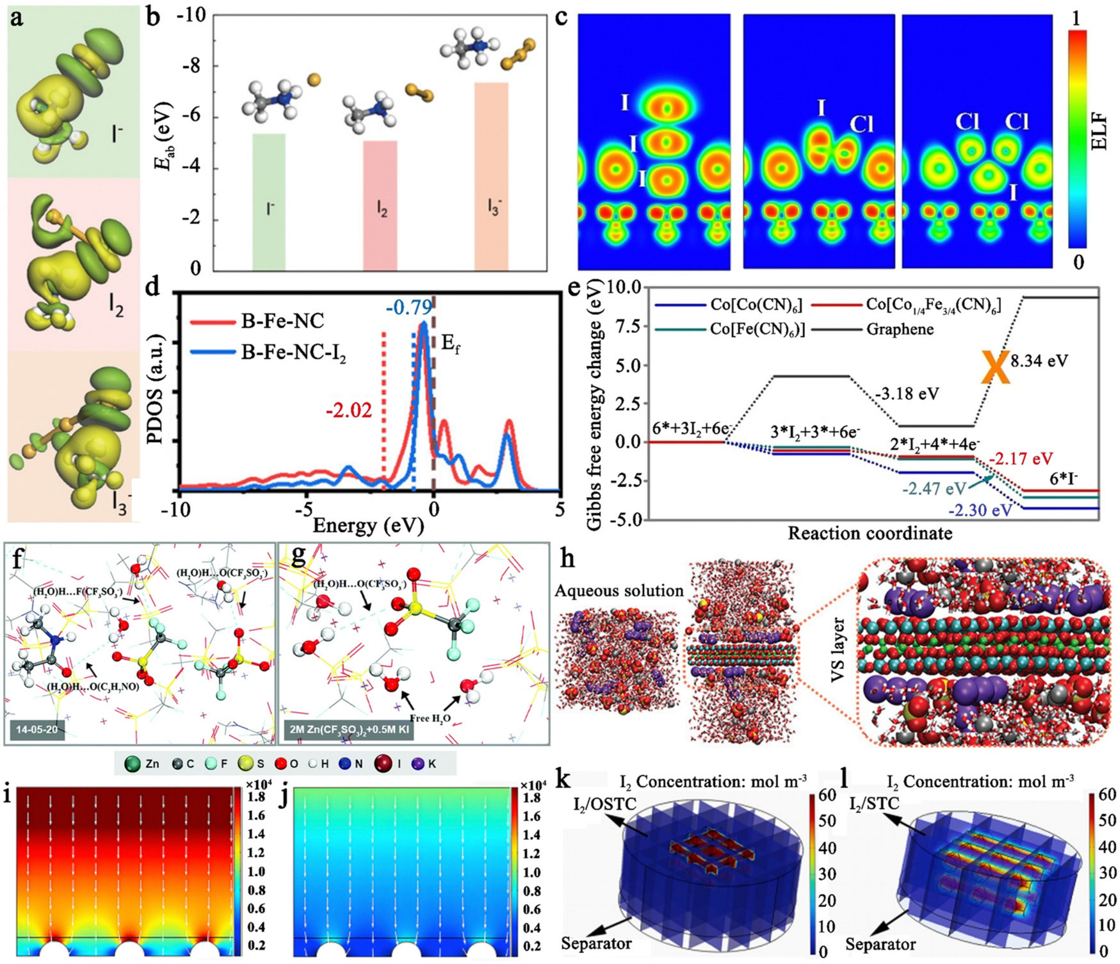

Fig. 19 (a) Optimized charge-density-difference patterns of I^-, I_2, and I_3^- on CH_6N^+. (b) The calculated adsorption energy of iodine species (I^-, I_2, and I_3^-) on CH_6N^+. Reprinted with permission from ref. 53. Copyright 2022 Wiley. (c) Electron localization function of iodine redox products. Reprinted with permission from ref. 18. Copyright 2021 Wiley. (d) Partial density of states analysis for the d-band of Fe in B–Fe–NC and B–Fe–NC–I_2. Reprinted with permission from ref. 183. Copyright 2022 American Chemical Society. (e) Gibbs free-energy diagrams of iodine reduction reactions on $Co[Co(CN)_6]$, $Co[Fe(CN)_6]$, $Co[Co_{1/4}Fe_{3/4}(CN)_6]$, and bilayer graphene. Reprinted with permission from ref. 190. Copyright 2020 Wiley. Local hydrogen bond distributions in (f) 14-05-20 eutectic solution, and (g) 2 M $Zn(CF_3SO_3)_2$ + 0.5 M KI. Reprinted with permission from ref. 85. Copyright 2022 Royal Society of Chemistry. (h) MD simulations of iodine in 1 M $ZnSO_4$ and vermiculite nanosheets electrolytes. I, Zn, S, O, H, Si, and Mg are represented by purple, gray, yellow, red, white, cyan, and green spheres, respectively. Reprinted with permission from ref. 205. Copyright 2023 Wiley. COMSOL Multiphysics simulations of the electric field distribution of (i) bare Zn and (j) Zn@ZSO anodes. Reprinted with permission from ref. 216. Copyright 2022 Elsevier. COMSOL Multiphysics simulations of I_2 concentration distribution in (k) I_2/OSTC, and (l) I_2/STC models during the discharge process. Reprinted with permission from ref. 251. Copyright 2023 Elsevier.

B-Fe-NC/I_2 (a porous carbon with atomic bridging of iron coordinated to nitrogen atoms/I_2) can reach the Fermi level through a narrow energy gap of −0.79 eV, indicating enhanced charge migration between iodine and carbon with atomic bridging of iron and nitrogen. (3) Investigation of iodine reaction pathways. By calculating the Gibbs free energy (ΔG) associated with the conversion of iodine on different active centers, one can evaluate the complexity of the reaction process; this helps to elucidate experimental observations like low polarization, enhanced rate capability, and efficient iodine utilization. For example, Ma *et al.* elucidated the role of Co and/or Fe metal species in the framework of Prussian blue analogues for the electrocatalysis of the I_2 reduction reaction by calculating the corresponding ΔG value.[190] Generally, a low ΔG value indicates a high degree of spontaneity and a fast reaction rate. As depicted in Fig. 19e, the substantial value of the reaction path ($I_3^- \rightarrow I^-$) suggests that the reduction of I_3^- is the rate-determining step for the whole reaction process. In this regard, the $Co[Co_{1/4}Fe_{3/4}(CN)_6]$ framework exhibits the lowest ΔG value of 2.17 eV at this step, indicating the fastest kinetic conversion of iodine on $Co[Co_{1/4}Fe_{3/4}(CN)_6]$. Consequently, the $Co[Co_{1/4}Fe_{3/4}(CN)_6]$ framework demonstrates superior rate capability.

3.1.2 Molecular dynamics simulation.

(1) Analysis of the solvation structure of electrolyte salts. This is one of the common applications of molecular dynamics simulation in MIBs. For example, Yang *et al.* utilized molecular dynamics simulations to clarify the structural differences between an aqueous solution (2 M $Zn(CF_3SO_3)_2$ + 0.5 M KI in H_2O) and a eutectic solution

(14-05-20, referred to as a solution of $Zn(CF_3SO_3)_2$ and *N*-methylacetamide (N-ACE) at a molar ratio of 1 : 4 with 0.5 M KI and 20% H_2O).[85] As shown in Fig. 19f and g, the F atoms of $CF_3SO_3^-$ and the carbonyl oxygen atoms of N-ACE in the eutectic solution offer additional sites capable of forming hydrogen bonds compared to the aqueous solution, indicating a low degree of free water in eutectic solution. Furthermore, by combining the radial distribution functions with the characterization results, they effectively demonstrated the double-shell structure of the eutectic solution, *i.e.*, a tight inner layer consisting of I^- and $CF_3SO_3^-$ and an outer layer including H_2O and $C_3H_7NO^-$. (2) Visualization of the affinity of materials for iodine species. The relatively macroscopic perspective provides insight into the adsorption of material towards iodide species. As illustrated in Fig. 19h, polyiodide is primarily concentrated near the vermiculite nanosheet layer, while showing a uniform distribution in a 1 M $ZnSO_4$ aqueous solution.[205] This effectively demonstrated that the vermiculite nanosheet layer can impede the shuttle effect of polyiodide in the electrolyte.

3.1.3 Finite element analysis. This is a mathematical rather than a chemical approach to show the effect of macroscopic physical properties (*e.g.*, pore size, heat transfer coefficient, and ion diffusion coefficient) on materials. MIBs are commonly used in this context to simulate two key aspects: the plating/stripping process of metal ions in anodes and the diffusion behavior of iodine species in materials. Peng *et al.* utilized COMSOL Multiphysics simulation to visualize the distribution of Zn^{2+} flux and the penetration behavior in bare Zn and Zn@zinc silicate (Zn@ZSO).[216] As depicted in Fig. 19i and j, the electric field concentration on the surface of bare Zn is highly uneven. However, the incorporation of the ZSO interphase effectively enhances the homogeneity of the electric field strength due to the optimization and homogenization of the Zn^{2+} flux by the interfacial ion transport channels of Zn@ZSO. Consequently, the restricted 2D diffusion of Zn^{2+} in Zn@ZSO contributes to the uniform Zn plating/stripping chemistry at the Zn anode. Moreover, Chen *et al.* demonstrated the impact of pore diameter in materials on the iodine adsorption capability using COMSOL Multiphysics simulation.[251] The results indicated that I_2/OSTC (I_2-loaded oxidized salt-templated carbon) with a smaller pore diameter facilitates the confinement of iodine inside the material (Fig. 19k and l).

3.2 Advanced *in situ* characterization techniques

In situ characterization techniques have advanced the monitoring of changes in physicochemical properties of electrode materials, electrolytes, and separators in real-time during the charging and discharging processes. This holds significant implications in elucidating the working mechanism of batteries, while providing crucial theoretical foundations and experimental strategies for developing innovative materials of MIBs. Various *in situ* characterization techniques have been developed in the field of MIBs, including *in situ* Raman spectroscopy, ultraviolet-visible (UV-vis) spectroscopy, X-ray diffraction (XRD), and optical microscopy (OM). In the following, we present an overview of the typical applications of these techniques in MIBs:

3.2.1 *In situ* Raman spectroscopy. (1) *In situ* monitoring of the iodine conversion process. This is the most common application of *in situ* Raman testing in MIBs. As early as 2015, Zhao *et al.* investigated the reaction mechanism of iodine cathodes in a rechargeable lithium-ion battery using *in situ* Raman testing.[95] As shown in Fig. 20a, the Raman signal of iodine cathodes can be captured using a custom device (*i.e.*, a hole in the cathode cover of an ordinary coin-type battery). As a result, the spectrum exhibited a symmetric stretching peak of I_3^- (located between 110 and 120 cm^{-1}), which undergoes a reversible shift during the charge/discharge process, corresponding to the reaction of I^-/I_2 with the formation of I_3^- as an intermediate product (Fig. 20b). Similarly, Li *et al.* demonstrated the presence of I_3^- as an intermediate product that appears and disappears during the cycling process.[53] Especially, complementary techniques such as X-ray photoelectron spectroscopy (XPS) and XRD techniques can be used to detect other iodine species (I^- and I_2) and further confirm the occurrence of the $I^-/I_3^-/I_2$ reaction process. It is worth mentioning that, due to a change in the iodine reaction mechanism, *in situ* Raman testing can detect the I_5^- peak in addition to the I_3^- peak. For example, when a polyvinylpyrrolidone–iodine (PVP–I_2) cathode was used, the chemical interaction between PVP and iodine led to a change in the mechanism ($I^- \leftrightarrow I_3^- \leftrightarrow I_5^-$), enabling *in situ* Raman spectroscopy to examine the I_5^- species (Fig. 20c).[98] Meanwhile, solid-state Li–I_2 batteries with poly(ethylene oxide) (PEO) acting as the dispersion layer to significantly dissolve polyiodide can also lead to the formation of I_5^-.[128] Moreover, in aqueous cells, where I_2 readily combines with I^- to form polyiodide (I_3^- and I_5^-), the $I^-/I_3^-/I_5^-$ mechanism can be detected using *in situ* Raman testing.[176,183] (2) *In situ* tracking of changes in the surface chemistry of materials (preferably inorganic materials). As shown in Fig. 20d, *in situ* Raman measurements reveal the transformation of the surface functional groups of I_2/HOF@$Ti_3C_2T_x$ (hydrogen-bonded organic framework linked to the $Ti_3C_2T_x$ MXene complex) during the cycling process.[146] Attributing to the formation of strong I–O bonds after incorporating I_2 into HOF@$Ti_3C_2T_x$, the signal of –OH groups at 265 cm^{-1} in $Ti_3C_2(OH)_2$ decreases gradually during the discharging process, while the –O groups at 208 cm^{-1} in $Ti_3C_2O_2$ show an increasing trend. This observation well demonstrated that the –OH functional groups in $Ti_3C_2T_x$ MXene play a crucial role in trapping iodine and preventing the shuttle effect.

3.2.2 *In situ* ultraviolet-visible spectroscopy. Compared to *in situ* Raman testing, the usage of *in situ* UV-vis testing is currently less common. It is mainly employed in aqueous cells due to their insensitivity to oxygen and water in the air. Consequently, it is able to conduct *in situ* UV-visible experiments using simple, open-ended, and homemade quartz electrochemical cells (Fig. 20e).[85] The primary purpose of *in situ* UV-vis testing is to monitor changes in ion concentration (I^-, I_3^-, I_2, and IO_3^-) in the electrolyte as a function of cell voltage. For instance, Wang *et al.* utilized *in situ* UV-visible testing to demonstrate that when the charging voltage of a Zn–I_2 battery reaches up to 1.85 V, excessive oxidation of I_2 will result in the production of IO_3^- (340 nm) (Fig. 20f).[208] Additionally, Yang *et al.* also proved that the 14-05-20 eutectic electrolyte can suppress the polyiodide shuttling better than the aqueous

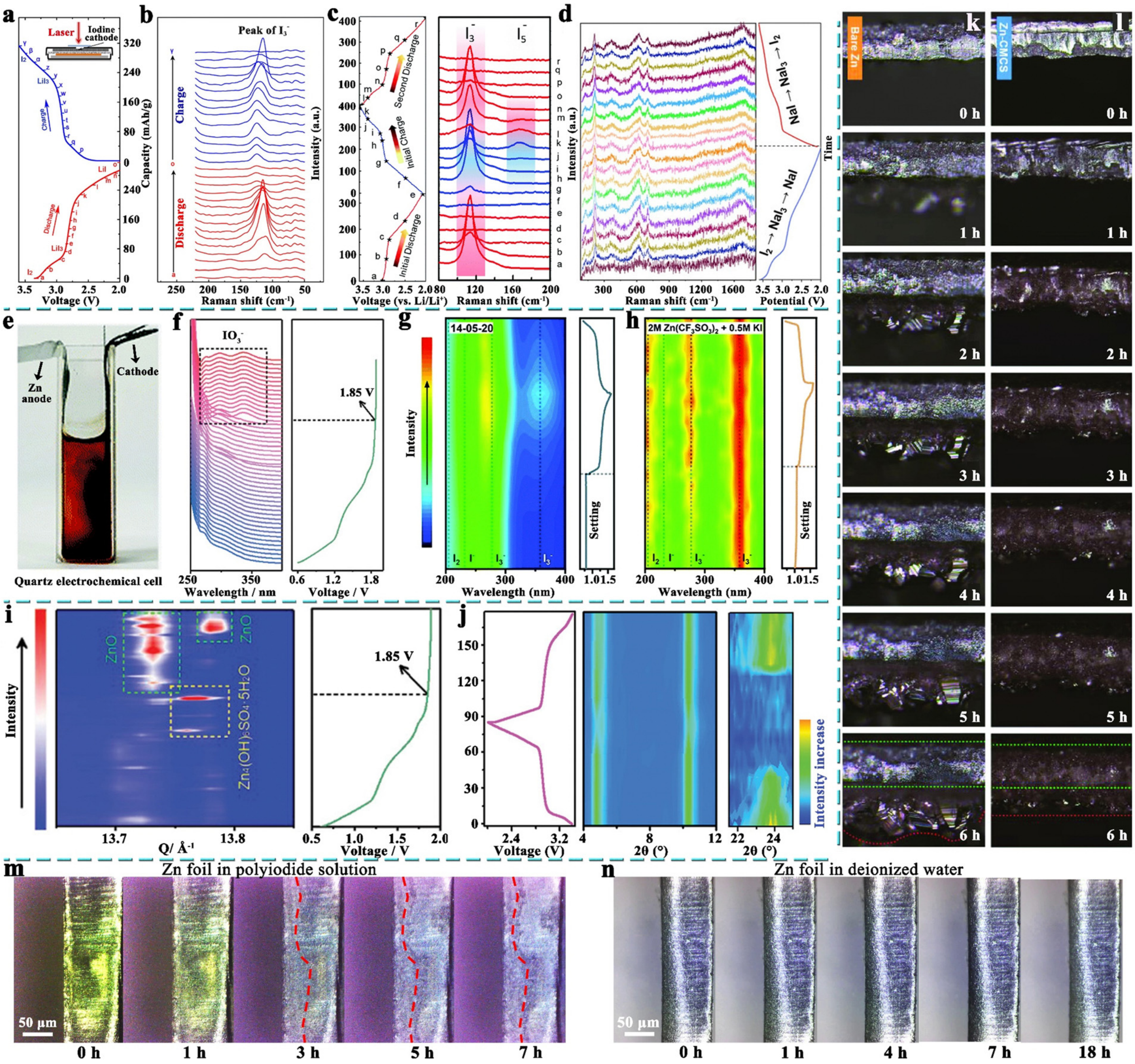

Fig. 20 Analysis of Li–I_2 batteries using *in situ* Raman with (a) corresponding charge and discharge curves (inset: schematic diagram of an *in situ* Raman cell), and (b) Raman spectra of a Li–I_2 battery at different voltages. Reprinted with permission from ref. 95. Copyright 2015 American Chemical Society. (c) Discharge and charge curves of an *in situ* Raman cell with ACC/PVP–I_2 as the cathode, and Raman spectra corresponding to the marked points in the curves. Reprinted with permission from ref. 98. Copyright 2018 Royal Society of Chemistry. (d) *In situ* Raman analysis of the I_2/HOF@$Ti_3C_2T_x$ cathode and corresponding charge/discharge curve. Reprinted with permission from ref. 146. Copyright 2022 Wiley. (e) Schematic of an *in situ* UV cell. Reprinted with permission from ref. 85. Copyright 2022 Royal Society of Chemistry. (f) The *operando* UV-vis spectroscopy of electrolyte in a Zn–I_2 cell with a I_2/N-doped carbon cathode during the charging process. Reprinted with permission from ref. 208. Copyright 2020 Wiley. *In situ* UV-vis absorption spectra of Zn–I_2 batteries using (g) 14-05-20 eutectic electrolyte, and (h) 2 M $Zn(CF_3SO_3)_2$ + 0.5 M KI electrolyte. Reprinted with permission from ref. 85. Copyright 2022 Royal Society of Chemistry. (i) The *operando* synchrotron XRD analysis of anode composition changes during charging of Zn–I_2 cells. Reprinted with permission from ref. 208. Copyright 2020 Wiley. (j) The *operando* XRD characterization of Fe_2–O_8–PcCu/I_2 electrode during the charge/discharge process. Reprinted with permission from ref. 24. Copyright 2019 Wiley. *In situ* OM observation of Zn^{2+} deposition behavior on (k) Zn-CMCS, and (l) bare Zn. Reprinted with permission from ref. 220. Copyright 2023 Wiley. Corrosion processes of Zn foil in (m) polyiodide solution, and (n) deionized water observed by *in situ* OM. Reprinted with permission from ref. 212. Copyright 2023 Wiley.

electrolyte, as the *in situ* UV spectra of the 14-05-20 eutectic electrolyte showed a significantly lower iodine species concentration (I^-, I_3^-, and I_2) during the cell cycling process (Fig. 20g and h).[85]

3.2.3 *In situ* X-ray diffraction patterns. (1) Detection of compositional changes of zinc anodes. Overcharging of Zn–I_2 batteries can accelerate irreversible processes in the Zn anode, leading to battery failure. With the *operando* synchrotron XRD technique, Wang *et al.* revealed the failure mechanism of Zn anodes in an overcharged Zn–I_2 cell. As shown in Fig. 20i, they demonstrated that overcharging will greatly facilitate the irreversible conversion of soluble $Zn_4(OH)_6SO_4{\cdot}5H_2O$ to non-reusable ZnO in the zinc anode, resulting in the irreversible loss of zinc.[208] (2) The study of structural changes in cathode materials during cycling. For example, Wang *et al.* conducted *in situ* XRD characterization to investigate the evolution of the Fe_2–O_8–PcCu (Fe_2[(2,3,9,10,16,17,23,24-octahydroxy phthalocyaninato)Cu])/I_2 cathode during the charge/discharge process (Fig. 20j).[24] They found that the characteristic (109) peak of I_2 at 25° changed reversibly during the cell cycling process, indicating the reversible iodine redox pathways. Besides, although both the (100) and (200) peaks of Fe_2–O_8–PcCu slightly shifted towards higher 2θ values during the discharging process due to the formation of I_3^-/Fe_2–O_8–PcCu intermediates, the layered structure of Fe_2–O_8–PcCu/I_2 remained intact during the cycling process, proving the high stability of Fe_2–O_8–PcCu cathodes.

3.2.4 *In situ* optical microscopy. Optical microscopy is one of the oldest, simplest, and most accessible microscopy techniques.[252] It has been widely used in MIBs (especially in Zn-based aqueous batteries) to observe the dendrites growth on metal anodes, as well as the occurrence of corrosion reactions. In a study conducted by Li *et al.*, the zinc deposition processes of Zn-carboxymethyl chitosan (Zn-CMCS) and bare zinc were observed using *in situ* optical microscopy in a 2 M $ZnSO_4$ + 0.5 M KI electrolyte.[220] As a result, bare Zn had a bulky and inhomogeneous galvanic coating, while Zn-CMCS demonstrated a uniform interface during zinc plating (Fig. 20k and l). This reflects the exceptional ability of CMCS to stabilize the zinc plating/stripping behavior. In addition, Zhang *et al.* investigated the effect of polyiodide on the zinc anodic corrosion process using *in situ* OM.[212] As shown in Fig. 20m and n, the Zn foil immersed in a polyiodide solution developed a noticeable bulge within 5 h, while the Zn foil in deionized water displayed negligible change even after 18 h. This suggests that polyiodide accelerates the zinc anodic corrosion process.

4 Summary and outlook

4.1 A full retrospective for metal–iodine batteries

So far, we have thoroughly reviewed the current development status of various metal–iodine batteries (MIBs) comprehensively. Some problems are commonly faced by MIBs, including the shuttling of iodine species and the irreversibility of metal anodes. Focusing on these questions, a great deal of work has been carried out based on iodine hosts, electrolytes, separators/interlayers, and anodes. Therefore, we further summarize the key innovations and design guidelines of these strategies in implementing advanced MIBs (Fig. 21), which will be discussed in detail below.

4.1.1 Iodine hosts. Presently, there are four main classes of materials used as the host of iodine, namely, carbon-based materials, organic materials, organic/inorganic composites, and others with transition metal elements (*e.g.*, MXenes and Prussian blue analogues (PABs)). For carbon-based materials, the following basic design rules should be considered: (1) a large surface area that can provide ample active sites to store and anchor iodine species; (2) controllable pore size

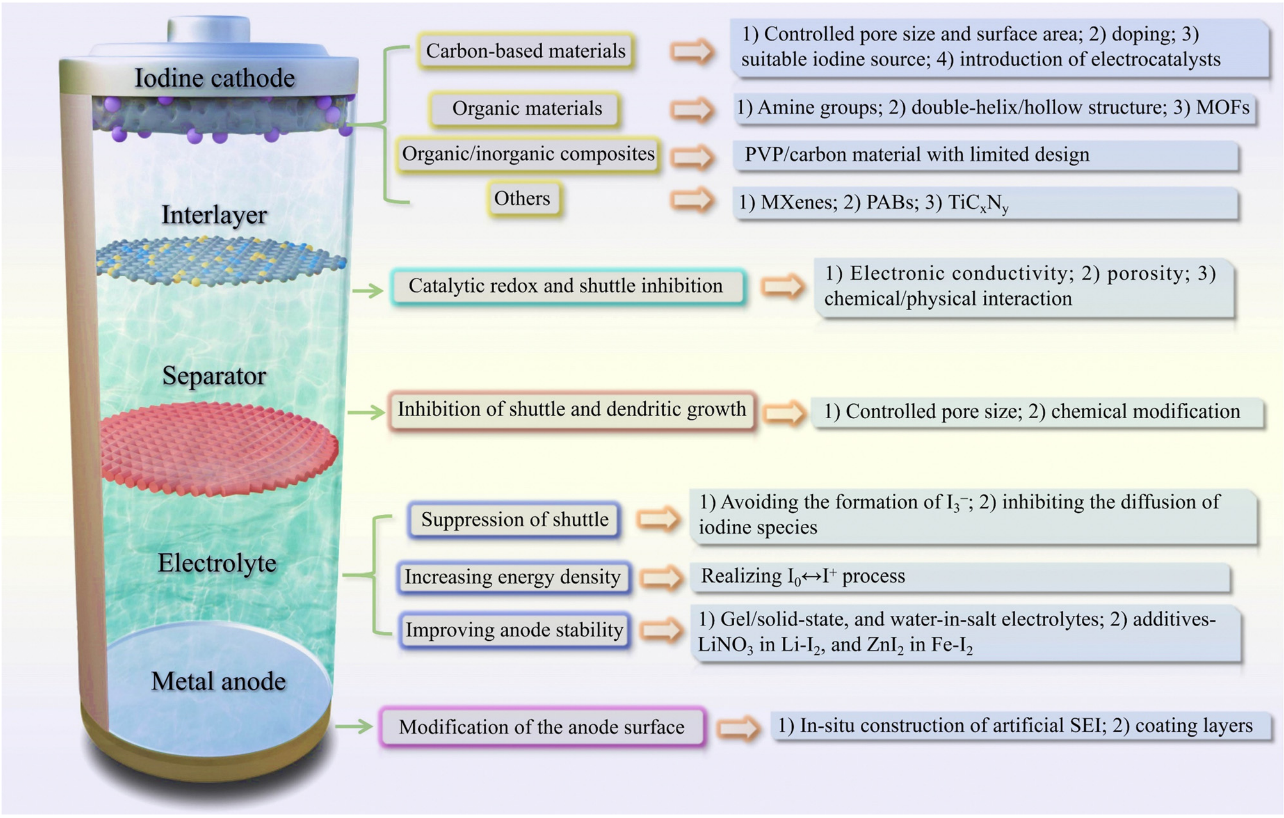

Fig. 21 Summary of strategies for implementing advanced metal–iodine batteries.

(<metal polyiodide size), which can effectively block the formation of highly soluble polyiodide through the pore size effect and prevent the free diffusion of iodine species;[72] (3) incorporation of the elemental doping strategy to enhance the interaction between inert carbon and iodine species;[174] (4) modulation of the graphite-N/pyridine-N value to optimize the adsorption and catalytic capacity of materials for iodine species;[170,172] (5) the introduction of electrocatalysts that can effectively catalyze iodine conversion, resulting in high battery rates and capacity;[183] (6) a suitable iodine source, that can avoid electrode volume expansion (LiI), increase the stability of iodine species (polyvinylpyrrolidone–I), and enhance the rate performance (two-dimensional few-layer iodine nanosheets).[107,109,110] For organic materials, amine structures (*e.g.*, primary/secondary amines and quaternary ammonium) generally exhibit excellent adsorption for iodine species through Lewis acid–base or electrostatic interactions.[27,53,186] In particular, quaternary ammonium cations demonstrate the best performance in iodine species adsorption. Some unique natural macromolecular structures, such as the double-helix structure of starch and the hollow structure of β-cyclodextrin, also show adsorption to iodine species.[42,80] But the double-helix structure facilitates superior performance of batteries compared to the hollow structure due to its superior binding force on polyiodide. When developing polymer-based iodine hosts in future work, therefore, it may be considered to introduce relevant amine groups and design suitable structures (*e.g.*, double-helix structure) to improve the performance of polymers in restricting iodine species. In addition, hydrogen-bonded organic frameworks (HOFs) and metal–organic framework (MOFs) have been explored as iodine hosts, with MOFs exhibiting superior properties over HOFs. This may be attributed to the unique advantages of MOFs in terms of atomically dispersed metal centers, rich pore structure, and extended π-conjugation, making it more suitable as an ideal host for iodine. On the other hand, research on organic/inorganic composites is generally limited in depth. Nonetheless, the unique advantages of PVP@carbon composites, including feasible preparation methods, low price, and moderate performance, have led to their extensive usage as cathodes for basic investigations on emerging MIBs (*e.g.*, Mg/Al/Fe–I_2 batteries).[76,78] Finally, some transition metal-containing materials, including MXenes, PABs, and TiC_xN_y compositions, can offer unique advantages in enabling fast battery charging.[83,111,190] This can be attributed to the active outer electron orbitals of transition metals, which can effectively catalyze the iodine redox reaction. Besides, adequate porosity and electrical conductivity are necessary for these materials to suppress the free migration of iodine species and enable efficient utilization of insulating iodine. It is expected that more attention will be devoted to the exploration of these new materials in the future.

4.1.2 Electrolyte. Electrolytes in MIBs perform complex and diverse functions, unlike iodine host materials whose primary role is to inhibit polyiodide shuttling. Therefore, we classify electrolytes in MIBs into the following three categories according to their functions:

(1) Suppression of polyiodide shuttling to improve battery stability. This can be achieved in two ways, *i.e.*, avoiding the formation of polyiodide, and inhibiting the diffusion of iodine species in electrolytes. In theory, the first method is only applicable for aqueous batteries because iodine hardly dissolves in water but has high solubility in organic solvents, which will lead to shuttle effects. Typically, electrolyte systems, including PEG400-containing electrolytes, *N*-methylacetamide-containing eutectic electrolytes, and high-concentration chloride-containing salt electrolytes, are capable of fulfilling the former function, where the key to the success of these electrolytes is to prevent the bonding of iodine and iodide ions.[85,86,203] For instance, with the formation of the $[ZnI_x(OH_2)_{4-x}]_{2-x}$ superhalide ions or double-shell solvated structure (the inner layer consists of I^- and $CF_3SO_3^-$, and the outer layer includes H_2O and C_3H_7NO), the electrostatic interaction between iodide ions and surrounding ions/molecules will be greatly reduced, thereby resulting in the low concentration of polyiodide.[85,86] Especially, with a high concentration of $ZnCl_2$ electrolyte (5 M KI/20 M $ZnCl_2$), Ji *et al.* achieved an advanced Zn–I_2 battery with 2000 cycles without capacity decline, even under an ultra-high iodine load of 25.33 mg cm^{-2}.[202] Besides, the complexation between PEG400 and iodine can also inhibit the reaction of iodine with I^- to form polyiodide.[203] On the other hand, both solid-state and gel electrolytes exhibit the function of restricting the shuttle effect of iodine species due to the restricted solubility of iodine species in these electrolytes. In terms of solid-state electrolytes, it is a key factor to achieve high battery performance by keeping iodine species in the liquid state, since solid-phase transformation would lead to sluggish reaction kinetics and poor battery rechargeability. For example, by introducing a polyethylene oxide layer to dissolve a large amount of polyiodide, more than 6000 cycles were achieved in $Li_{1.5}Al_{0.5}Ge_{1.5}(PO_4)_3$ solid-state electrolyte at a relatively low temperature of 60 °C.[128] For gel electrolytes, there are two approaches to achieve efficient shuttling inhibition, including integration with other materials capable of polyiodide confinement (*e.g.*, MXenes, MOFs, and carbon cloth) and structural modification. Tang *et al.* integrated $Ti_3C_2T_x$ MXene-wrapped carbon cloth–iodine with a composite gel polymer electrolyte to obtain a Li–I_2 battery with 85% capacity retention after 1000 cycles.[70] By immobilizing negatively charged polyanionic chains on the hydrogel skeleton, Shang *et al.* effectively blocked I_3^- from shuttling and resulted in a capacity retention of 66.8% after 2000 cycles in a Zn–I_2 battery.[207]

(2) Improvement of battery energy density. Commonly, chloride-containing salt electrolytes can achieve this purpose by I^0/I^+ conversion (theoretical capacity up to 422 mA h g^{-1}). One of the key factors in such a system is the formation of I^+Cl^- complexes to achieve the stabilization of I^+. Also, inert organic solvents (*e.g.*, acetonitrile) can be added to aqueous electrolytes to reduce the activity of water for alleviating irreversible reactions of I^+ ions in aqueous solutions.[40] Notably, the difference in iodine cathode composition seems to determine the complexity and reversibility of I^0/I^+ conversion. For example, when the $Ti_3C_2I_2$ MXene cathode was used, the concentration of $ZnCl_2$ rapidly decreased from 19 M (PAC carbon@I_2 cathode) to 2 M, although the high-concentration $ZnCl_2$ was more favorable for I^+ stabilization.[40,74] However, there is still a lack of systematic studies on how to exploit the synergy between the

cathode and electrolyte to achieve highly stable I^+ ions. On the other hand, the energy density of Li–I_2 batteries can be improved by using aqueous electrolytes due to the enhanced charge–discharge voltage platform (~3.5 V).[125] The high cost, high complexity, short lifespan, and low safety of this system, however, are significantly hindering its further development. In the case of the Zn–I_2 flow battery, the electrolyte containing Br^- and Cl^- ions can release I_3^- into I_2 by forming I_2Br^- and I_2Cl^-, thereby increasing iodine utilization and boosting battery capacity.[226,227] It is worth noting that Br^- ions are preferred over Cl^- ions due to the higher corrosiveness of the latter. Additionally, the adoption of an alkaline anolyte, containing 6 M KOH, allows for the reduction of the redox potential of the zinc anode to −1.26 V, leading to an increase in the total voltage of the Zn–I_2 flow cell to 1.796 V.[164] However, the feasibility of using an alkaline anolyte still needs to be evaluated critically due to the shortened battery life cause by cross-contamination ($Zn(OH)_4^{2-}$, I_3^-, and I^-), severe zinc dendrite growth, and irreversible disproportionation reaction ($6OH^- + 3I_2 \rightarrow 5I^- + IO_3^- + 3H_2O$).

(3) Improvement of anode stability. Gel/solid-state electrolytes and water-in-salt electrolytes are generally accompanied by positive functions to improve the stability of metal anodes. In addition, some electrolyte additives, such as $LiNO_3$, are also considered to be effective in improving anode stability since they can form stable passive films on the anode surface. Particularly, given the introduction of ZnI_2 in aqueous $FeCl_2$ electrolyte, the formation of $[ZnI]^+$ species allows the doping of Zn into the Fe lattice during the reduction process, resulting in uniform deposition of Fe anodes.[61] Besides, NH_4^+ ions are also considered to be effective in slowing down the growth of zinc dendrites due to the electrostatic shielding effect caused by the complexation of NH_4^+ ions with Zn^{2+} ions.[226] For Mg/Al–I_2 batteries, the properties of electrolytes are particularly important as they greatly determine the degree of reversibility of the metal anodes. At present, Mg–I_2 batteries use magnesium bis(trimethylsilyl)amide/$AlCl_3$/$MgCl_2$ in a tetraethylene glycol dimethyl ether electrolyte, while Al–I_2 batteries employ a $AlCl_3$/1-ethyl-3-methylimidazolium chloride electrolyte.

4.1.3 Separators and interlayers. There is a lack of research on these types of materials in MIBs. The research on separators primarily focuses on Zn–I_2 batteries, considering MOFs and zeolites as separators.[90,92] They are capable of playing a dual role in inhibiting polyiodide shuttling and dendrite growth. The common denominator of their designs is the control of pore size. For instance, a zeolite membrane with a porous framework (4 Å) can effectively confine the cross-over/shuttling of soluble I_3^- (5.14 Å).[90] By further introducing functional groups that can coordinate with Zn ions (*e.g.*, –COOH) in the porous framework, a highly aggregated electrolyte layer can be formed on the surface of the Zn anode for uniform electroplating/stripping of the Zn anode.[92] For the Zn–I_2 flow battery, a composite membrane consisting of starch and chitosan was developed, leveraging the "host–guest" chemistry between the membrane and iodine species.[233] Nevertheless, this design may result in the build-up of iodine species within the membrane, potentially obstructing its functionality due to the adsorption of iodine species by the membrane. On the other hand, materials such as B_2O_3-modified CNTs,[115] N-doped graphene,[43] and $Ti_3C_2T_x$ MXenes,[23] have been successively reported as interlayers in Li–I_2 batteries due to their outstanding advantages of the remarkable pseudo-capacitive effects with accelerated kinetic processes. Nevertheless, the poly(3,4-ethylenedioxythiophene):polystyrene sulfonate (PEDOT:PSS) interlayer does not show an obvious pseudo-capacitance behavior in aqueous Zn–I_2 batteries.[211] The in-depth reasons need to be explored, but one speculation is that the latter is due to the distinction in interlayers between inorganic materials (based on physisorption) and organic compounds (based on chemisorption), together with the variation in the solubility of iodine in aqueous and organic electrolytes. Regardless, they shall be able to exhibit excellent chemical/physical interactions with iodine species for inhibiting the shuttle effect. Meanwhile, electronic conductivity and high porosity that enable adsorption of dissolved iodine redox couples and catalyze the fast iodine conversion reaction are also required.[113,211]

4.1.4 Modified anodes. The issues faced by metal anodes in MIBs, while varying, are generally related to dendritic growth (except for Mg–I_2 batteries) and polyiodide corrosion. Modification of the anode surface is regarded as a more efficient way to achieve a highly reversible deposition/stripping process of metal anodes in MIBs than optimizing the intrinsic structure of the anode. This is because the modified anode surface can promote the plating/stripping process of metal anodes, and inhibit the damage of anodes by polyiodide shuttling.[223] On this basis, two strategies, *i.e.*, *in situ* construction of an artificial SEI and coating layers constructed by spin/scrape-coating, were proposed. The former has the advantage of forming a uniform and strongly adherent layer, while the latter is easier to prepare on a large scale. In any case, the recommended design features for modified layers are as follows: (1) capable of forming a stable, high mechanical strength, and high adhesion layer by reacting *in situ* or coating on the metal surface; (2) highly inert (In, Sn)/resistant (negative charge groups) to iodine and polyiodide to shield the anode from side reactions; (3) suitable pore size and a uniform pore structure to allow rapid and homogeneous transfer of metal ions but avoid penetration of polyiodide and iodine; and (4) low electrical conductivity but high ionic conductivity, which enable metal ions to migrate quickly through the layer rather than being deposited on it. To be noted, the materials currently used for anode protection in MIBs are almost all derived from other well-developed batteries, such as Zn/Li-ion and Li–S batteries. Therefore, the anode part of MIBs should be combined with its own problems (polyiodide shuttle) and introduce the advanced concepts of other battery systems to give full play to the late-mover advantage.

4.2 Existing bottlenecks and solutions

Despite most MIBs being in their infancy, Li/Zn–I_2 batteries have been developed for a long time. As the fundamental issues of batteries (*e.g.*, stability and rate performance) are continuously improved, some bottlenecks are gradually exposed that will be discussed below.

4.2.1 Cathode. (1) Iodine is generally more expensive than other elements (such as S, Cl, and Br) due to its relatively scarce resource (Table 1), despite the high stability and excellent rate performance of iodine-based batteries. In light of this, it is necessary to investigate the recycling processes of iodine, as in the case of lithium-ion batteries, to recover valuable metals such as nickel, cobalt, manganese, copper, aluminum, and lithium.[253] Thanks to the volatility and reactivity of iodine, efficient recycling methods could potentially be developed through thermal or chemical treatment of the electrodes. Despite this, research in this area has not yet been conducted using MIBs. It is worth exploring the possibilities of iodine recycling in MIBs. (2) Iodine is corrosive to current collectors (*e.g.*, copper, aluminum, and nickel) and stainless steel, especially in flow cells, where iodine is contained in the electrolyte. Thus, in terms of practical MIBs, it is important to design the cell structures, including the use of corrosion-resistant materials like titanium, carbon felts, and carbon paper as current collectors, as well as affordable plastics for battery packaging. Additionally, it may be beneficial to referr to the cell materials and stack sealing technology used in practical applications of zinc-bromine flow batteries, as bromine shares similarities with iodine and is even more corrosive. (3) Typically, thermal deposition and melt impregnation are the most widely used methods for loading with iodine. However, one often overlooked issue is the tendency of iodine to sublimate during the preparation process (sublimation temperature of $\sim$40 °C),[180] leading to iodine wastage and environmental pollution, particularly in the manufacturing of scale-up iodine cathodes. Therefore, novel approaches for iodine electrode preparation are recommended, such as electrochemical deposition, *in situ* chemical deposition of iodine ($3I_2 + 6OH^- \rightarrow IO_3^- + 5I^- + 3H_2O$; $IO_3^- + 5I^- + 6H^+ \rightarrow 3I_2 + 3H_2O$), and impregnation adsorption. (4) The low electric-ionic conduction of iodine poses challenges, especially in the formation of iodine films during the oxidation process in the cell, which significantly impedes the iodine redox process.[228] One possible approach to mitigate this issue is to introduce electrolyte additives (such as acetonitrile, PVP, and KI) that promote the dissolution of the iodine film, along with electrocatalysts to accelerate the iodine conversion process.

Numerous efforts also have been undertaken to develop high-performance iodine hosts, including carbon-based/organic materials, MXenes, and PABs. Regardless of this, the content (unit: wt%) and loading (unit: mg cm^{-2}) of iodine on the cathode jointly determine the areal capacity and energy density of battery devices. For instance, in lithium-ion batteries, an areal capacity of over 4 mA h cm^{-2} is required to power an electric vehicle.[8,254–256] However, most Li–I$_2$ batteries operate at around 3.0 V, which is lower than the 3.5 V of Li-ion batteries and results in an urgent requirement for Li–I$_2$ batteries to have higher areal capacities ($>$5 mA h cm^{-2}) in order to compete with state-of-the-art lithium-ion batteries. In this regard, the loading of iodine on the cathode must be as high as $\sim$24 mg cm^{-2} based on the theoretical capacity of iodine (211 mA h g^{-1}). When assuming a total iodine content of 50 wt% in the cathode, an unachievable value of iodine loading of 48 mg cm^{-2} would be observed. Therefore, there is an urgent need to investigate and develop highly loaded and high-content iodine cathodes. However, despite great strides in lifetime made by Li/Zn–I$_2$ batteries, their iodine content and loading are typically below 50 wt% and 3 mg cm^{-2} (Fig. 22a and b), respectively, which are far below the practical requirements. Encouragingly, on the way to achieving high iodine-containing cathodes, organic iodized salts and Nb-based MXene (Nb_2CT_x) materials have been able to achieve an iodine content of more than 80 wt%.[53,83] Combining a hydrothermal reduced graphene oxide cathode with a high concentration of $ZnCl_2$ electrolyte (5 M KI/20 M $ZnCl_2$), Li *et al.* also realized 2000 cycles without capacity decline even under an ultra-high iodine load of 25.33 mg cm^{-2}.[202] These works could contribute significantly to the commercialization of Li/Zn–I$_2$ batteries. Besides, Li/Zn–I$_2$ batteries, as an emerging technology, may draw valuable insights and research approaches from the relatively mature research field of metal-sulfur batteries due to their high similarity.[8] On another note, photo-assisted chargeable MIBs have been reported under the concept of "all-in-one".[73,100] However, these self-powered devices are generally at the proof-of-concept stage with poor performance. Although most studies demonstrated the synchronous conversion and storage of energy, they lacked insights into the ion and electron migration and storage involved in the process, as well as the investigations into battery failures. Relying on advanced characterization techniques, calculations, and simulations, in-depth and detailed working/failure mechanisms for MIBs batteries-contained practical "all-in-one" devices are expected to be explored in the future (Fig. 22c).

4.2.2 Electrolytes. The development of electrolytes for MIBs is relatively immature compared to cathodes due to the diversification of electrolyte functions. Despite this, we also highlight some key points of electrolyte development in MIBs (Fig. 22d). Typically, iodine loading can be categorized into two types: one involves the cathodic loading of iodine, while the other involves the use of a cathodic electrolyte for iodine loading. For the former one, although a high E/I ratio (E/I, unit: μL mg^{-1}) can enhance the discharge capacity and cycle stability of MIBs significantly, an excessive amount of electrolyte will inevitably lead to a decrease in the actual energy density.[257] Therefore, it is crucial to highlight the importance of maintaining a lean electrolyte condition for practical MIBs. However, the development of lean-electrolyte MIBs has not received sufficient attention and corresponding battery performance is lacking. Urgent investigations, involving E/I ratios, are expected in future work. For the latter type, the iodine concentration in the catholyte determines the energy density of battery directly. Tables 2–17 demonstrate that the concentration of I$^-$ ions in iodine-based static batteries typically ranges from 1–2 M, while it is generally between 2–7 M in Zn–I$_2$ flow batteries. However, these concentrations are still below the limiting solubility of polyiodide in the electrolyte (7–12 M). Therefore, further works, such as separator modification, electrolyte engineering, and the introduction of electrocatalysts, are required to increase the iodine concentration in electrolytes. Additionally, in this system, the formation of iodine films and incomplete conversion of iodine (I$^-$/I$_3^-$) can result in slow cathodic reactions and unsatisfactory battery energy density, respectively.[227,228] These issues

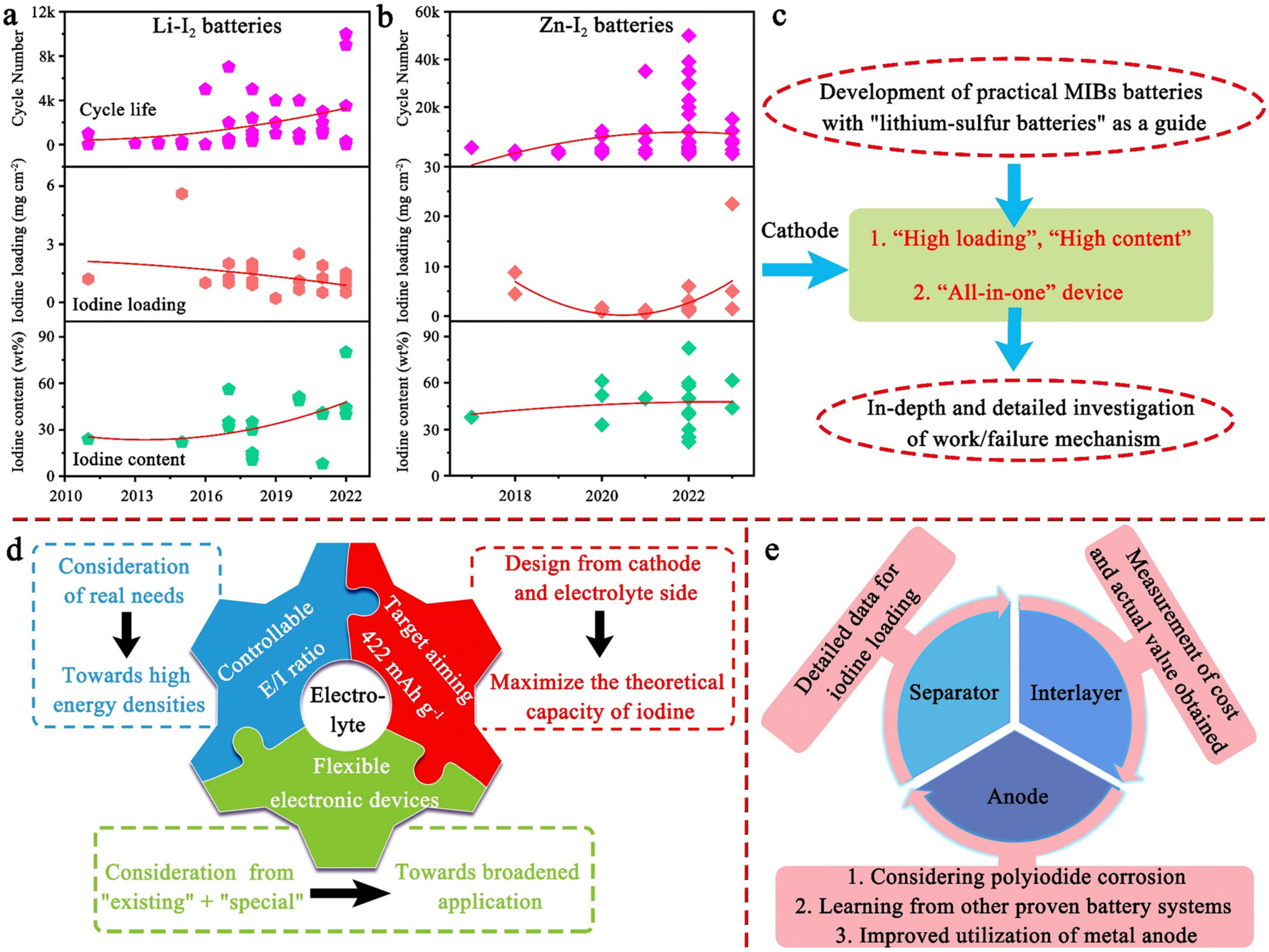

Fig. 22 Plot of cycle life, iodine load, and iodine content *versus* time in (a) Li–I_2 and (b) Zn–I_2 batteries. Recommended guidelines for the development of (c) cathode, (d) electrolyte, and (e) separator/interlayer/anode in MIBs.

can be mitigated by introducing additives (*e.g.*, acetonitrile, PVP, and KI) to promote iodine film dissolution, as well as by incorporating Cl^- and Br^- ions to enhance iodine utilization. During battery cycling, the increased viscosity and density of catholyte can lead to increased pressure within the cathode chamber, which induces the transfer of iodine species from the cathode to the anode, thereby accelerating battery capacity degradation.[237] A viable strategy to address this problem is to maintain a balanced hydraulic pressure by adjusting the flow rate ratio of electrolytes (catholyte : anolyte = 1 : 7), thereby preventing the convection of iodine species. However, this is clearly not suitable for static cells. Moreover, static cells also need to consider the tap density of cathodes and cannot hold a large amount of catholyte. Therefore, practical metal–iodine static batteries may not be compatible with an iodine-containing catholyte. It is more desirable to incorporate a significant amount of iodine into the cathode uniformly, to achieve high energy densities.

On the other hand, some electrolytes, such as chlorine-containing electrolytes, have been reported to achieve I^0/I^+ conversion, which substantially increases the theoretical capacity of iodine-based batteries to 422 mA h g^{-1}.[18,40] Such an ideal capacity is highly desirable in MIBs, as it can effectively reduce the iodine loading required in Li–I_2 batteries to ∼10 mg cm^{-2}. However, maintaining high reversibility of I^+ ions while suppressing the shuttle of polyiodide under high iodine loading remains problematic. Although the use of high concentration of chloride salts can stabilize I^+ ions, this approach not only greatly increases battery costs, but also demands high corrosion resistance of the cell structure. One feasible method may be to modify the iodine host so that the cathode is also conducive to the stabilization of I^+ ions, thereby reducing the need for electrolytes.[74] In Mg/Al–I_2 batteries, the high charge density of Mg^{2+}/Al^{3+} makes it challenging for chloride ions to dissociate in electrolytes, resulting in the low activity of chloride ions.[63] This could make I^0/I^+ conversion difficult to implement in these batteries even with a high concentration of chlorine salts. Therefore, an objective and comprehensive understanding of I^0/I^+ conversion is required in future work on MIBs. Solid-state/gel electrolytes generally provide higher security than liquid electrolytes. Besides, they can inhibit the shuttle of iodine species effectively and be used to develop a variety of flexible electronic devices. However, they often suffer from short cycle life and poor rate performance.[134,258] A good solution is a combination of "existing" + "special", *i.e.*, using other proven battery system solutions, such as Li/Zn-ion batteries, with due consideration to improving iodine utilization and suppressing polyiodide shuttling in MIBs. A vivid example is the "confined dissolution" strategy proposed by Chen and co-workers, who used the traditional NASICON-type ceramic electrolyte in combination with a polyethylene glycol layer (dissolving iodine species) to achieve a high-performance all-solid-state Li–I_2 battery with over 9000 cycles.[128]

4.2.3 Separators, interlayers, and anodes. A brief illustration of the separator, interlayer, and anode is given in Fig. 22e. Typically, catholytes containing iodized salts are used as active materials while studying separators to avoid an unobjective assessment of the separator performance caused by the absorption of polyiodide by modified cathodes. However, this also results in generally low actual iodine content, as well as a lack of true judgment on iodine loading. One suggestion for the authors is to provide iodine loading data so that the battery can be evaluated objectively. On the other hand, interlayers can utilize iodine species to afford a remarkable pseudo-capacitive effect for energy storage and greatly accelerate the kinetic process even up to 100C.[43,114] However, similar problems to those faced by separators, in this case, remain with low iodine loading in cathode electrochemical tests. Besides, the introduction of interlayers increases the battery's inactive component, which may lead to a decrease in energy density and an increase in cost. Despite this issue, recent studies have shown that the utilization of interlayers can confer MIBs with high stability (over 20 000 cycles in Zn–I_2 batteries) and rate capability (up to 100C). Therefore, they should further move towards practicality while considering the relationship between cost and performance.

The stability of metal anodes usually plays a vital role in battery performance during the long cycling process. Maintaining anode stability has become a common problem in metal-based batteries, and several effective solutions have emerged, including anode internal structure optimization,[259] anode surface coating modification,[260] multifunctional separator designs,[92] and electrolyte modification,[261] which can also be applied to MIBs. It is important to note that the adopted strategy should be able to protect anodes from iodine species and avoid problems such as polyiodide corrosion and battery self-discharge. For example, Ren *et al.* used a Li–In alloy layer to promote the stability of the Li anode while also imparting a graphene paper layer on the anode to inhibit polyiodide shuttling.[138] Besides, improving the utilization of used metal anodes is necessary to speed up the practical application of MIBs. In this regard, the authors should provide key information in detail, including the amount of metal anode, electrolyte usage, and iodine loading, which would be beneficial for the objective evaluation of the actual battery performance.

4.3 Future prospects and recommendations

Reviewing the state-of-the-art rechargeable MIBs, it can be found that MIBs are on the rise as novel energy storage systems, especially Li/Zn–I_2 batteries. In order to achieve the continued rapid development of MIBs, it is necessary to accurately understand the placement of different MIBs. Given the commonality of iodine cathodes, MIBs differ more significantly in terms of the anode. Therefore, Fig. 23a provides an intuitive insight into the advantages and disadvantages of MIBs by counting the differences in anodes (price, abundance, specific capacity, volumetric capacity, and redox potential) as well as the overall performance of MIBs (stability and rate). The data are typically processed by percentage conversion based on the obtained maximum value of a certain condition. For example, given that the prices of lithium and iron are ~19.2 $ $\mathrm{kg^{-1}}$ (the highest value in terms of cost) and ~2.4 $ $\mathrm{kg^{-1}}$, respectively, the obtained equivalent values for lithium and iron are thus 100 and 12.5, respectively. Unsurprisingly, Li–I_2 batteries show a huge advantage in energy density due to the high redox potential and specific capacity of Li metal anodes. Currently, the state-of-the-art Li–I_2 battery can possess an energy density of ~1324 W h $\mathrm{kg^{-1}_{iodine}}$ (based on I^-/I^+ conversion) and a discharge voltage plateau of 3.42 V.[18] As a class of conversion-type batteries, Li–I_2 batteries have faster rates than Li-ion batteries, with a capability of up to 100C.[43] Meanwhile, owing to the highly reversible iodine conversion reaction and few intermediates, Li–I_2 batteries generally have long lifetimes of thousands of cycles (even up to 10 000 cycles) and high capacity retention.[53] These merits make Li–I_2 batteries fully complementary to LIBs for alleviating problems associated with the shortage of battery resources such as Co and Ni. However, the low abundance and high price of Li metal make Li-based batteries theoretically unsuitable for the future large-scale energy storage market. Alternatively, Na–I_2 batteries may be a promising system to compensate for the deficiencies of lithium-based batteries. Na–I_2 batteries can possess a discharge plateau of ~2.7 V and long lifetimes (up to 5000 cycles) with outstanding rate capability.[110,151] As the commercialization of sodium-ion batteries continues and results in the gradual maturation of the sodium-based battery industry, Na–I_2 batteries are demonstrating promising applications in a wide range of batteries. On the other hand, the advantages of K–I_2 batteries lie in their high abundance and deep redox potential. However, their short lifespan and low safety, caused by own defects (K metal is too reactive), could seriously limit their wide application like Li/Na–I_2 batteries, making research on them likely to remain in a long-term fundamental state.[68,154] In terms of multivalent MIBs, Zn–I_2 batteries are currently the most promising battery system. Typically, Zn–I_2 batteries have demonstrated a durable life of over 10 000 cycles and an outstanding rate performance of over 10C.[27,42,83,175] With the realization of I^0/I^+ conversion, the Zn–I_2 cell is able to deliver an energy density of ~750 W h $\mathrm{kg^{-1}}$ (based on iodine) with two discharge plateaus of 1.83 V (I^0/I^+) and 1.29 V (I^-/I^0), demonstrating its sufficient advantages over manganese/vanadium-based Zn-ion batteries.[40] By combining the advantages of safety, environmental friendliness, low cost, and high operability, Zn–I_2 batteries show significant promise as one of the lead-acid battery replacements, and are applied in large-scale energy storage systems. Moreover, Zn–I_2 flow batteries, with a remarkable theoretical capacity of 268 A h $\mathrm{L^{-1}}$, hold significant potential for practical applications.[232] On the other hand, the high abundance and ultra-low cost of Fe/Mg/Al–I_2 batteries have also aroused a passion for research.

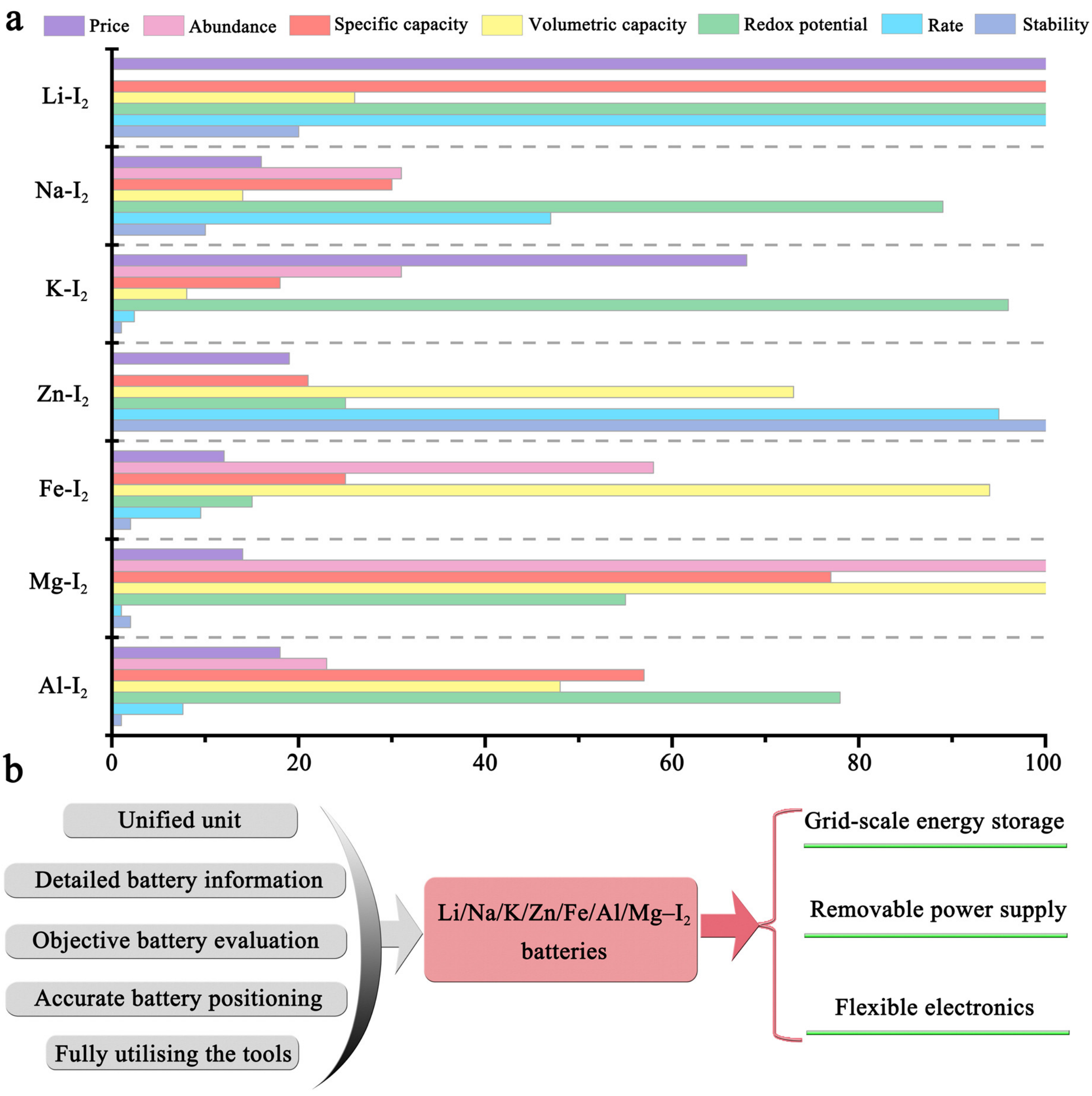

Fig. 23 (a) Schematic diagram for visual comparison of different MIBs in terms of price, abundance, specific capacity, volumetric capacity, redox potential, rare, and stability. (b) Proposed suggestions and prospects for the continuous high-quality and rapid development of MIBs in the future.

However, the intrinsic nature of these metals also severely limits the performance of the as-fabricated metal–iodine batteries. Although, Fe–I$_2$ batteries can show over 1200 cycles and a rate of ∼7.6C, their low discharge plateau (<0.9 V) and the instability of the Fe anode in aqueous electrolytes may hinder their further investigation. For Mg/Al–I$_2$ batteries, the anodes commonly tend to form insulating and passivation layers during the cycling process, resulting in short battery life and slow plating/stripping processes. In addition, the high charge density of Mg^{2+}/Al^{3+} further inevitably leads to sluggish battery kinetics. As a result, the cycle life of Mg/Al–I$_2$ batteries is inferior with a rate performance generally lower than 1C.[25,76] On account of this, for these types of iodine batteries, extensive research should continue to focuson addressing the inherent problems of metal anodes.

In order to maintain the rapid development of metal–iodine batteries, Fig. 23b presents some recommendations. (1) Uniform unit should be used (1C = 211 mA g^{-1} as the rate unit). Detailed cell information, including the amount of metal anodes, electrolyte usage, E/I ratio, iodine loading, negative/positive ratio, needs to be provided. These are helpful for readers to evaluate the actual working conditions of the battery and avoid misplaced guidance. (2) The overall volumetric energy density of iodine cathodes should be provided. According to the iodine content and the associated percentage of inactive material, the gravimetric energy density of iodine cathodes is easily obtained. However, despite the importance of volumetric energy densities of batteries in practical applications (*e.g.*, it is impractical to install batteries with low volumetric energy density for space-constrained electric vehicles), studies (except for flow batteries) seldom refer to the volumetric energy density of iodine cathodes. Thus, it is necessary to provide relevant volumetric energy density of iodine cathodes, for driving enthusiasm in pursuing practically usable metal–iodine batteries. (3) Cell lifespan should be evaluated at low current rates below 2C. Because the high C-rate implies a fast charging and discharging process that constrains the diffusion of polyiodide dissolved in the electrolyte (electric field effect), which in turn will cover up the inhibitory effect of materials on the shuttle effect.[262,263] (4) The performance of materials should be evaluated from both the ''local'' and ''system'' perspective. For example, when attempting to build a separator to inhibit polyiodide shuttling and achieve highly stable MIBs, tests should first be performed using a catholyte containing iodide, as well as a cathode that does not adsorb polyiodide; this can be a good reflection of the electrochemical performance of the material from the ''local'' perspective. Then, from the ''system'' aspect, the application of common (carbon cloth and active carbon) or state-of-the-art cathode materials to test the cells gives a good indication of the progressiveness of this work. Benefiting from this, readers can effectively understand the advancement of the work through literature review. (5) Accurate battery placement is essential to ensure that the batteries can meet market demand during the process of development, instead of accumulating useless data. For example, when defining the $Zn–I_2$ battery as a safe, green alternative to the ''lead-acid battery'' system, we should also design $Zn–I_2$ batteries according to ''lead-acid battery'' specifications, rather than positioning them to compete with the existing lithium-ion batteries. (6) Taking advantage of late movers. As different battery systems have both differences and commonalities, the development of MIBs should not be restricted to itself. For instance, the design of anodes and cathodes of $Li–I_2$ batteries can draw upon some advanced concepts and methods from lithium-ion batteries and Li–S batteries, to reduce unnecessary ''detours''. (7) Development of advanced characterization technologies, such as *in situ* Raman, X-ray diffraction, and ultraviolet-visible spectroscopy. These methods would help to discover the real working mechanism, reaction process, and existing problems of batteries, so as to design materials with advanced properties. (8) The utilization of systematic theoretical calculations, such as density functional theory calculation, molecular dynamics simulation, and COMSOL Multiphysics simulation, which allows us to establish theoretical foundations and provide guidance for experiments. (9) Combination with artificial intelligence (*e.g.*, machine learning). This allows us to access knowledge quickly, enable interdisciplinarity, and bring more innovation to our work. All these would drive the rapid development of MIBs with continuous improvement of competitiveness. Desirably, by matching different anodes, iodine-based batteries can adapt to various complex and changeable application environments, that is, high-safety and green zinc–iodine batteries can be applied to smart home energy storage and flexible electronic devices; cheap and resourceful iron/aluminum/magnesium–iodine batteries can be used for grid-scale energy storage; and high-energy-density lithium–iodine batteries can power electric-driven vehicles. All in all, we believe that metal–iodine batteries will occupy a prominent place in a variety of battery systems in the future.

Conflicts of interest

The authors declare no conflict of interest.

Acknowledgements

The authors sincerely acknowledge the financial support from the National Natural Science Foundation of China (no. 52161135302, no. 52233006, and no. 52211530489). F. L. acknowledges the financial support from the Research Foundation-Flanders (FWO, grant no. 1298323N). J. H. acknowledges the financial support from the Research Foundation-Flanders (FWO, grant no. G0F2322N, G983.19N, G0A5817N, and ZW15_09-G0H6316N, VS06523N), from the Flemish government through long-term structural funding Methusalem (CASAS2, Meth/15/04), and from the MPI as an MPI fellow.

Notes and references

1 E. C. Evarts, *Nature*, 2015, **526**, S93–S95.
2 D. G. Kwabi, Y. Ji and M. J. Aziz, *Chem. Rev.*, 2020, **120**, 6467–6489.
3 B. Steffen and A. Patt, *Energy Res. Soc. Sci.*, 2022, **91**, 102758.
4 U.S. Energy Information Administration, International Energy Outlook 2021, **https://www.eia.gov/outlooks/ieo/climate.php**.
5 A. Azizivahed, A. Arefi, S. Ghavidel, M. Shafie-khah, L. Li, J. Zhang and J. P. S. Catalao, *IEEE Trans. Sustain. Energy*, 2020, **11**, 662–673.
6 F. Cebulla, J. Haas, J. Eichman, W. Nowak and P. Mancarella, *J. Cleaner Prod.*, 2018, **181**, 449–459.
7 H.-F. Wang and Q. Xu, *Matter*, 2019, **1**, 565–595.
8 S. H. Chung and A. Manthiram, *Adv. Mater.*, 2019, **31**, e1901125.
9 P. Li, C. Li, X. Guo, X. Li and C. Zhi, *Bull. Chem. Soc. Jpn.*, 2021, **94**, 2036–2042.
10 K. Chen, D. Y. Yang, G. Huang and X. B. Zhang, *Acc. Chem. Res.*, 2021, **54**, 632–641.
11 Q. Pang, X. Liang, C. Y. Kwok and L. F. Nazar, *Nat. Energy*, 2016, **1**, 16132.
12 J. Ma, M. Liu, Y. He and J. Zhang, *Angew. Chem., Int. Ed.*, 2021, **60**, 12636–12647.
13 V. Viswanathan, A. H. Epstein, Y.-M. Chiang, E. Takeuchi, M. Bradley, J. Langford and M. Winter, *Nature*, 2022, **601**, 519–525.
14 G. L. Soloveichik, *Chem. Rev.*, 2015, **115**, 11533–11558.
15 H. Lim, A. Lackner and R. Knechtli, *J. Electrochem. Soc.*, 1977, **124**, 1154.
16 B. Li, Z. Nie, M. Vijayakumar, G. Li, J. Liu, V. Sprenkle and W. Wang, *Nat. Commun.*, 2015, **6**, 6303.
17 P. Bai and M. Z. Bazant, *Electrochim. Acta*, 2016, **202**, 216–223.

18 X. Li, Y. Wang, Z. Chen, P. Li, G. Liang, Z. Huang, Q. Yang, A. Chen, H. Cui, B. Dong, H. He and C. Zhi, *Angew. Chem., Int. Ed.*, 2022, **61**, e202113576.

19 C. Bai, H. Jin, Z. Gong, X. Liu and Z. Yuan, *Energy Storage Mater.*, 2020, **28**, 247–254.

20 D. Lin and Y. Li, *Adv. Mater.*, 2022, **34**, e2108856.

21 F. Bertasi, F. Sepehr, G. Pagot, S. J. Paddison and V. Di Noto, *Adv. Funct. Mater.*, 2016, **26**, 4860–4865.

22 K. Jayaramulu, D. P. Dubal, B. Nagar, V. Ranc, O. Tomanec, M. Petr, K. K. R. Datta, R. Zboril, P. Gómez-Romero and R. A. Fischer, *Adv. Mater.*, 2018, **30**, 1705789.

23 C. Sun, X. Shi, Y. Zhang, J. Liang, J. Qu and C. Lai, *ACS Nano*, 2020, **14**, 1176–1184.

24 F. Wang, Z. Liu, C. Yang, H. Zhong, G. Nam, P. Zhang, R. Dong, Y. Wu, J. Cho, J. Zhang and X. Feng, *Adv. Mater.*, 2020, **32**, 1905361.

25 H. Tian, S. Zhang, Z. Meng, W. He and W.-Q. Han, *ACS Energy Lett.*, 2017, **2**, 1170–1176.

26 C. Liang and C. Holmes, *J. Power Sources*, 1980, **5**, 3–13.

27 L. Zhang, M. Zhang, H. Guo, Z. Tian, L. Ge, G. He, J. Huang, J. Wang, T. Liu, I. P. Parkin and F. Lai, *Adv. Sci.*, 2022, **9**, 2105598.

28 Y. Zhao, L. Wang and H. R. Byon, *Nat. Commun.*, 2013, **4**, 1896.

29 S. G. Bratsch, *J. Phys. Chem. Ref. Data*, 1989, **18**, 1–21.

30 D. E. Harlov and L. Aranovich, *The Role of Halogens in Terrestrial and Extraterrestrial Geochemical Processes: Surface, Crust, and Mantle*, Springer International Publishing, Cham, 2018, pp. 1–19, DOI: 10.1007/978-3-319-61667-4_1.

31 S. Hou, L. Chen, X. Fan, X. Fan, X. Ji, B. Wang, C. Cui, J. Chen, C. Yang, W. Wang, C. Li and C. Wang, *Nat. Commun.*, 2022, **13**, 1281.

32 Y. Li and H. Dai, *Chem. Soc. Rev.*, 2014, **43**, 5257–5275.

33 X. Gu, T. Tang, X. Liu and Y. Hou, *J. Mater. Chem. A*, 2019, **7**, 11566–11583.

34 Y. Chen, J. Xu, P. He, Y. Qiao, S. Guo, H. Yang and H. Zhou, *Sci. Bull.*, 2022, **67**, 2449–2486.

35 G. Li, T. An, J. Chen, G. Sheng, J. Fu, F. Chen, S. Zhang and H. Zhao, *J. Hazard. Mater.*, 2006, **138**, 392–400.

36 Y. Jung, E. Hong, M. Kwon and J.-W. Kang, *Chem. Eng. J.*, 2017, **312**, 30–38.

37 X. Li, N. Li, Z. Huang, Z. Chen, Y. Zhao, G. Liang, Q. Yang, M. Li, Q. Huang, B. Dong, J. Fan and C. Zhi, *ACS Nano*, 2021, **15**, 1718–1726.

38 A. A. Yaroshevsky, *Geochem. Int.*, 2006, **44**, 48–55.

39 L. Zhang, M. Zhang, H. Guo, Z. Tian, L. Ge, G. He, J. Huang, J. Wang, T. Liu and I. P. Parkin, *Adv. Sci.*, 2022, **9**, 2105598.

40 Y. Zou, T. Liu, Q. Du, Y. Li, H. Yi, X. Zhou, Z. Li, L. Gao, L. Zhang and X. Liang, *Nat. Commun.*, 2021, **12**, 170.

41 S. H. Chung and A. Manthiram, *Adv. Mater.*, 2019, **31**, 1901125.

42 S. J. Zhang, J. Hao, H. Li, P. F. Zhang, Z. W. Yin, Y. Y. Li, B. Zhang, Z. Lin and S. Z. Qiao, *Adv. Mater.*, 2022, **34**, 2201716.

43 Z. Su, Z. Wei, C. Lai, H. Deng, Z. Liu and J. Ma, *Energy Storage Mater.*, 2018, **14**, 129–135.

44 N. Chen, W. Wang, Y. Ma, M. Chuai, X. Zheng, M. Wang, Y. Xu, Y. Yuan, J. Sun, K. Li, Y. Meng, C. Shen and W. Chen, *Small Methods*, 2023, 2201553, DOI: 10.1002/smtd.202201553.

45 L. Rosenfeld, *J. Chem. Educ.*, 2000, **77**, 984.

46 A. McKeown, *Trans. Faraday Soc.*, 1922, **17**, 517–521.

47 A. A. Schneider, D. E. Harney and M. J. Harney, *J. Power Sources*, 1980, **5**, 15–23.

48 F.-C. Liu, W.-M. Liu, M.-H. Zhan, Z.-W. Fu and H. Li, *Energy Environ. Sci.*, 2011, **4**, 1261–1264.

49 J. Wiaux and R. Bannehr, *J. Power Sources*, 1987, **19**, 37–43.

50 B. Scrosati and B. Owens, *Solid State Ionics*, 1987, **23**, 275–278.

51 M.-L. Lin, Y.-X. Jin, Y.-Z. Zhang and Y.-F. Hou, *J. Power Sources*, 1985, **14**, 173–177.

52 L. Weinstein, W. Yourey, J. Gural and G. Amatucci, *J. Electrochem. Soc.*, 2008, **155**, A590.

53 P. Li, X. Li, Y. Guo, C. Li, Y. Hou, H. Cui, R. Zhang, Z. Huang, Y. Zhao, Q. Li, B. Dong and C. Zhi, *Adv. Energy Mater.*, 2022, **12**, 2103648.

54 M. Holzapfel, D. Wilde, C. Hupbauer, K. Ahlbrecht and T. Berger, *Electrochim. Acta*, 2017, **237**, 12–21.

55 D. Gong, B. Wang, J. Zhu, R. Podila, A. M. Rao, X. Yu, Z. Xu and B. Lu, *Adv. Energy Mater.*, 2017, **7**, 1601885.

56 K. Lu, H. Zhang, F. Ye, W. Luo, H. Ma and Y. Huang, *Energy Storage Mater.*, 2019, **16**, 1–5.

57 T. Yamamoto, *J. Chem. Soc., Chem. Commun.*, 1981, 187–188.

58 T. Yamamoto, M. Hishinuma and A. Yamamoto, *Inorg. Chim. Acta*, 1984, **86**, L47–L49.

59 H. Pan, B. Li, D. Mei, Z. Nie, Y. Shao, G. Li, X. S. Li, K. S. Han, K. T. Mueller, V. Sprenkle and J. Liu, *ACS Energy Lett.*, 2017, **2**, 2674–2680.

60 A. K. Manohar, S. Malkhandi, B. Yang, C. Yang, G. K. Surya Prakash and S. R. Narayanan, *J. Electrochem. Soc.*, 2012, **159**, A1209–A1214.

61 W. Wu, X. Yang, K. Wang, C. Li, X. Zhang, H.-Y. Shi, X.-X. Liu and X. Sun, *Chem. Eng. J.*, 2022, **432**, 134389.

62 F. Gutmann, A. M. Hermann and A. Rembaum, *J. Electrochem. Soc.*, 1967, **114**, 323.

63 Y. Liang, H. Dong, D. Aurbach and Y. Yao, *Nat. Energy*, 2020, **5**, 646–656.

64 Z. Guo, S. Zhao, T. Li, D. Su, S. Guo and G. Wang, *Adv. Energy Mater.*, 2020, **10**, 1903591.

65 R. Attias, M. Salama, B. Hirsch, Y. Goffer and D. Aurbach, *Joule*, 2019, **3**, 27–52.

66 H. Tian, T. Gao, X. Li, X. Wang, C. Luo, X. Fan, C. Yang, L. Suo, Z. Ma, W. Han and C. Wang, *Nat. Commun.*, 2017, **8**, 14083.

67 M. Li, J. Lu, X. Ji, Y. Li, Y. Shao, Z. Chen, C. Zhong and K. Amine, *Nat. Rev. Mater.*, 2020, **5**, 276–294.

68 L. Deng, M. Feng, R. Wang, Y. Yang, X. Niu, J. Zhang, L. Tan, J. Zhang, Y. Chen, L. Zeng, Y. Zhu and L. Guo, *Energy Storage Mater.*, 2021, **41**, 798–804.

69 T. Yamamoto, *J. Chem. Soc., Chem. Commun.*, 1981, 187–188.

70 X. Tang, D. Zhou, P. Li, X. Guo, C. Wang, F. Kang, B. Li and G. Wang, *ACS Cent. Sci.*, 2019, **5**, 365–373.

71 O. N. Srivastava and R. A. Singh, *Bull. Electrochem.*, 1999, **15**, 372–375.

72 Y. Li, L. Liu, H. Li, F. Cheng and J. Chen, *Chem. Commun.*, 2018, **54**, 6792–6795.

73 Y. Man, Q. Hao, F. Chen, X. Chen, Y. Wang, T. Liu, F. Liu and N. Li, *ChemElectroChem*, 2019, **6**, 5872–5875.

74 X. Li, M. Li, Z. Huang, G. Liang, Z. Chen, Q. Yang, Q. Huang and C. Zhi, *Energy Environ. Sci.*, 2021, **14**, 407–413.

75 C. Johnson, R. J. Latham and R. G. Linford, *Solid State Ionic*, 1982, **7**, 331–334.

76 Y. Zhang, D. Tao, F. Xu and T. Li, *Chem. Eng. J.*, 2022, **427**, 131592.

77 B. Xue, Z. Fu, H. Li, X. Liu, S. Cheng, J. Yao, D. Li, L. Chen and Q. Meng, *J. Am. Chem. Soc.*, 2006, **128**, 8720–8721.

78 S. Zhang, X. Tan, Z. Meng, H. Tian, F. Xu and W.-Q. Han, *J. Mater. Chem. A*, 2018, **6**, 9984–9996.

79 Q. Zhang, Z. Wu, F. Liu, S. Liu, J. Liu, Y. Wang and T. Yan, *J. Mater. Chem. A*, 2017, **5**, 15235–15242.

80 F.-s Cai, Y.-q Duan and Z.-h Yuan, *J. Mater. Sci.: Mater. Electron.*, 2018, **29**, 11540–11545.

81 H. K. Machhi, K. K. Sonigara, S. N. Bariya, H. P. Soni and S. S. Soni, *ACS Appl. Mater. Interfaces*, 2021, **13**, 21426–21435.

82 K. K. Sonigara, J. Zhao, H. K. Machhi, G. Cui and S. S. Soni, *Adv. Energy Mater.*, 2020, **10**, 2001997.

83 X. Li, N. Li, Z. Huang, Z. Chen, G. Liang, Q. Yang, M. Li, Y. Zhao, L. Ma, B. Dong, Q. Huang, J. Fan and C. Zhi, *Adv. Mater.*, 2021, **33**, e2006897.

84 C. Prehal, H. Fitzek, G. Kothleitner, V. Presser, B. Gollas, S. A. Freunberger and Q. Abbas, *Nat. Commun.*, 2020, **11**, 4838.

85 Y. Yang, S. Liang, B. Lu and J. Zhou, *Energy Environ. Sci.*, 2022, **15**, 1192–1200.

86 J. J. Hong, L. Zhu, C. Chen, L. Tang, H. Jiang, B. Jin, T. C. Gallagher, Q. Guo, C. Fang and X. Ji, *Angew. Chem., Int. Ed.*, 2019, **58**, 15910–15915.

87 P. Beran and S. Bruckenstein, *Anal. Chem.*, 1968, **40**, 1044–1051.

88 Y. Tian, S. Chen, S. Ding, Q. Chen and J. Zhang, *Chem. Sci.*, 2023, **14**, 331–337.

89 Q. Zhang, Y.-H. Zeng, S.-H. Ye and S. Liu, *J. Power Sources*, 2020, **463**, 228212.

90 Z. Li, X. Wu, X. Yu, S. Zhou, Y. Qiao, H. Zhou and S. G. Sun, *Nano Lett.*, 2022, **22**, 2538–2546.

91 M. Xing, Z. Z. Zhao, Y. J. Zhang, J. W. Zhao, G. L. Cui and J. H. Dai, *Mater. Today Energy*, 2020, **18**, 100534.

92 H. Yang, Y. Qiao, Z. Chang, H. Deng, P. He and H. Zhou, *Adv. Mater.*, 2020, **32**, e2004240.

93 W. Du, E. H. Ang, Y. Yang, Y. Zhang, M. Ye and C. C. Li, *Energy Environ. Sci.*, 2020, **13**, 3330–3360.

94 Y. L. Wang, Q. L. Sun, Q. Q. Zhao, J. S. Cao and S. H. Ye, *Energy Environ. Sci.*, 2011, **4**, 3947–3950.

95 Q. Zhao, Y. Lu, Z. Zhu, Z. Tao and J. Chen, *Nano Lett.*, 2015, **15**, 5982–5987.

96 H. Wang, G. Zhang, L. Ke, B. Liu, S. Zhang and C. Deng, *Nanoscale*, 2017, **9**, 9365–9375.

97 K. Li, S. Chen, S. Chen, X. Liu, W. Pan and J. Zhang, *Nano Res.*, 2018, **12**, 549–555.

98 Z. Meng, X. Tan, S. Zhang, H. Ying, X. Yan, H. Tian, G. Wang and W. Q. Han, *Chem. Commun.*, 2018, **54**, 12337–12340.

99 Y. Lai, L. Wang and W. Chen, *ChemElectroChem*, 2022, **9**, e202200022.

100 J. Li, H. Liu, K. Sun, R. Wang, C. Qian, F. Yu, L. Zhang and W. Bao, *J. Mater. Chem. A*, 2022, **10**, 7326–7332.

101 K. Lu, Z. Hu, J. Ma, H. Ma, L. Dai and J. Zhang, *Nat. Commun.*, 2017, **8**, 527.

102 K. Li, B. Lin, Q. Li, H. Wang, S. Zhang and C. Deng, *ACS Appl. Mater. Interfaces*, 2017, **9**, 20508–20518.

103 G. Zhang, H. Wang, S. Zhang and C. Deng, *J. Mater. Chem. A*, 2018, **6**, 9019–9031.

104 G. Zheng, Q. Zhang, J. J. Cha, Y. Yang, W. Li, Z. W. Seh and Y. Cui, *Nano Lett.*, 2013, **13**, 1265–1270.

105 L. Chai, X. Wang, Y. Hu, X. Li, S. Huang, J. Pan, J. Qian and X. Sun, *Adv. Sci.*, 2022, **9**, e2105063.

106 Y. Xu, Y. Wen, Y. Zhu, K. Gaskell, K. A. Cychosz, B. Eichhorn, K. Xu and C. Wang, *Adv. Funct. Mater.*, 2015, **25**, 4312–4320.

107 Z. Wu, J. Xu, Q. Zhang, H. Wang, S. Ye, Y. Wang and C. Lai, *Energy Storage Mater.*, 2018, **10**, 62–68.

108 C. Kuang, W. Zeng, M. Qian and X. Liu, *ChemPlusChem*, 2021, **86**, 865–869.

109 Z. Meng, H. Tian, S. Zhang, X. Yan, H. Ying, W. He, C. Liang, W. Zhang, X. Hou and W. Q. Han, *ACS Appl. Mater. Interfaces*, 2018, **10**, 17933–17941.

110 M. Qian, Z. Xu, Z. Wang, B. Wei, H. Wang, S. Hu, L. M. Liu and L. Guo, *Adv. Mater.*, 2020, **32**, e2004835.

111 V. G. Anju, M. P. Austeria and S. Sampath, *Adv. Mater. Interfaces*, 2017, **4**, 1700151.

112 G. Li, F. Lu, X. Dou, X. Wang, D. Luo, H. Sun, A. Yu and Z. Chen, *J. Am. Chem. Soc.*, 2020, **142**, 3583–3592.

113 Z. Su, Z. Wei, C. Lai, H. Deng, Z. Liu and J. Ma, *Energy Storage Mater.*, 2018, **14**, 129–135.

114 Z. Z. Wu, S. Y. Wang, R. Y. Wang, J. Liu and S. H. Ye, *J. Electrochem. Soc.*, 2018, **165**, A1156–A1159.

115 Z. Su, C.-J. Tong, D.-Q. He, C. Lai, L.-M. Liu, C. Wang and K. Xi, *J. Mater. Chem. A*, 2016, **4**, 8541–8547.

116 C. Gao, X. Li, G. Wei, S. Wang, X. Zhao and F. Kong, *Compos. Commun.*, 2022, **33**, 101226.

117 J. Chen, J. Ma, B. Liu, Z. Li, X. Zhang, S. Sun, K. Lu, J. Yin, S. Chen, X. Zu, Z. Zhang, X. Qiu, Y. Qin and W. Zhang, *Compos. Commun.*, 2023, **38**, 101524.

118 J. Yu, S. Liu, G. Duan, H. Fang and H. Hou, *Compos. Commun.*, 2020, **19**, 239–245.

119 W. Li, H. Yao, K. Yan, G. Zheng, Z. Liang, Y. M. Chiang and Y. Cui, *Nat. Commun.*, 2015, **6**, 7436.

120 C. Barchasz, J.-C. Leprêtre, S. Patoux and F. Alloin, *Electrochim. Acta*, 2013, **89**, 737–743.

121 F. Liu, S.-B. Cao, X.-G. Ou, Q.-Q. Hu and C.-M. Li, *Adv. New Renewable Energy*, 2020, **8**, 143–150.

122 J. A. Dean, *University of Tennessee*, McGrawHill, Inc, Knoxville, 1999.

123 J. Coetzee and C. Gardner, *Anal. Chem.*, 1982, **54**, 2625–2626.

124 N. Papageorgiou, W. Maier and M. Grätzel, *J. Electrochem. Soc.*, 1997, **144**, 876.

125 Y. Zhao, M. Hong, N. Bonnet Mercier, G. Yu, H. C. Choi and H. R. Byon, *Nano Lett.*, 2014, **14**, 1085–1092.

126 C. Shao, Y. Zhao and L. Qu, *SusMat*, 2022, **2**, 142–160.

127 G. Nikiforidis, K. Tajima and H. R. Byon, *ACS Energy Lett.*, 2016, **1**, 806–813.

128 Z. Cheng, H. Pan, F. Li, C. Duan, H. Liu, H. Zhong, C. Sheng, G. Hou, P. He and H. Zhou, *Nat. Commun.*, 2022, **13**, 125.

129 N. S. Choi, Z. Chen, S. A. Freunberger, X. Ji, Y. K. Sun, K. Amine, G. Yushin, L. F. Nazar, J. Cho and P. G. Bruce, *Angew. Chem., Int. Ed.*, 2012, **51**, 9994–10024.

130 X. Yang, K. R. Adair, X. Gao and X. Sun, *Energy Environ. Sci.*, 2021, **14**, 643–671.

131 F.-C. Liu, Z. Shadike, F. Ding, L. Sang and Z.-W. Fu, *J. Power Sources*, 2015, **274**, 280–285.

132 B. Sun, P. Wang, J. Xu, Q. Jin, Z. Zhang, H. Wu and Y. Jin, *Nano Res.*, 2021, **15**, 4076–4082.

133 R. Tomat and A. Rigo, *J. Appl. Electrochem.*, 1986, **16**, 8–14.

134 D. Zhou, D. Shanmukaraj, A. Tkacheva, M. Armand and G. Wang, *Chem*, 2019, **5**, 2326–2352.

135 X. Zhang, Y. Yang and Z. Zhou, *Chem. Soc. Rev.*, 2020, **49**, 3040–3071.

136 K. Li, Z. Hu, J. Ma, S. Chen, D. Mu and J. Zhang, *Adv. Mater.*, 2019, **31**, e1902399.

137 Z. Liu, W. Hu, F. Gao and H. Deng, *J. Mater. Chem. A*, 2018, **6**, 7807–7814.

138 Y. X. Ren, T. S. Zhao, H. R. Jiang, M. C. Wu and M. Liu, *J. Power Sources*, 2017, **347**, 136–144.

139 M. J. Giammona, J. Kim, Y. Kim, P. Medina, K. Nguyen, H. Bui, G. O. Jones, A. T. Tek, L. Sundberg, A. Fong and Y. H. La, *Adv. Mater. Interfaces*, 2023, **10**, 2300058.

140 P. K. Nayak, L. Yang, W. Brehm and P. Adelhelm, *Angew. Chem., Int. Ed.*, 2018, **57**, 102–120.

141 Y. Liu, J. Li, Q. Shen, J. Zhang, P. He, X. Qu and Y. Liu, *eScience*, 2022, **2**, 10–31.

142 C. Li, M. Qiu, R. Li, X. Li, M. Wang, J. He, G. Lin, L. Xiao, Q. Qian, Q. Chen, J. Wu, X. Li, Y.-W. Mai and Y. Chen, *Adv. Fiber Mater.*, 2021, **4**, 43–65.

143 H. Zhu and R. J. Kee, *Electrochim. Acta*, 2016, **219**, 70–81.

144 X. Lu, M. E. Bowden, V. L. Sprenkle and J. Liu, *Adv. Mater.*, 2015, **27**, 5915–5922.

145 H. Yingying, W. Xiangwei and W. Zhaoyin, *Energy Storage Sci. Technol.*, 2021, **10**, 781.

146 C. Guo, B. Han, W. Sun, Y. Cao, Y. Zhang and Y. Wang, *Angew. Chem., Int. Ed.*, 2022, **61**, e202213276.

147 L. Xiang, S. Yuan, F. Wang, Z. Xu, X. Li, F. Tian, L. Wu, W. Yu and Y. Mai, *J. Am. Chem. Soc.*, 2022, **144**, 15497–15508.

148 T. Zhang, F. Wei, Y. Wu, W. Li, L. Huang, J. Fu, C. Jing, J. Cheng and S. Liu, *Adv. Sci.*, 2023, **10**, 2301918.

149 Z. Lin, Q. Xia, W. Wang, W. Li and S. Chou, *InfoMat*, 2019, **1**, 376–389.

150 H. Che, S. Chen, Y. Xie, H. Wang, K. Amine, X.-Z. Liao and Z.-F. Ma, *Energy Environ. Sci.*, 2017, **10**, 1075–1101.

151 H. Tian, H. Shao, Y. Chen, X. Fang, P. Xiong, B. Sun, P. H. L. Notten and G. Wang, *Nano Energy*, 2019, **57**, 692–702.

152 M. Xu, Y. Li, M. Ihsan-Ul-Haq, N. Mubarak, Z. Liu, J. Wu, Z. Luo and J. K. Kim, *Energy Storage Mater.*, 2022, **44**, 477–486.

153 L. Zhang, L. Ge, G. He, Z. Tian, J. Huang, J. Wang, D. J. L. Brett, J. Hofkens, F. Lai and T. Liu, *J. Phys. Chem. C*, 2021, **125**, 18604–18613.

154 M. Qian, M. Tang, J. Yang, W. Wei, M. Chen, J. Chen, J. Xu, Q. Liu and H. Wang, *J. Colloid Interface Sci.*, 2019, **551**, 177–183.

155 J. Ding, H. Zhang, W. Fan, C. Zhong, W. Hu and D. Mitlin, *Adv. Mater.*, 2020, **32**, e1908007.

156 L. Ma, Y. Lv, J. Wu, C. Xia, Q. Kang, Y. Zhang, H. Liang and Z. Jin, *Nano Res.*, 2021, **14**, 4442–4470.

157 J. Xiong, M. Ye, Z. Wang, J. Chen, Y. Zhang, Y. Tang and C. C. Li, *Chem. Eng. J.*, 2022, **442**, 135927.

158 C. Wei, Y. Tao, H. Fei, Y. An, Y. Tian, J. Feng and Y. Qian, *Energy Storage Mater.*, 2020, **30**, 206–227.

159 Z. Yang, B. Wang, Y. Chen, W. Zhou, H. Li, R. Zhao, X. Li, T. Zhang, F. Bu, Z. Zhao, W. Li, D. Chao and D. Zhao, *Natl. Sci. Rev.*, 2023, **10**, nwac268.

160 H. Yang, T. Zhang, D. Chen, Y. Tan, W. Zhou, L. Li, W. Li, G. Li, W. Han, H. J. Fan and D. Chao, *Adv. Mater.*, 2023, **35**, 2300053.

161 R. Zhao, X. Dong, P. Liang, H. Li, T. Zhang, W. Zhou, B. Wang, Z. Yang, X. Wang, L. Wang, Z. Sun, F. Bu, Z. Zhao, W. Li, D. Zhao and D. Chao, *Adv. Mater.*, 2023, **35**, 2209288.

162 W. Zhou, M. Song, P. Liang, X. Li, X. Liu, H. Li, T. Zhang, B. Wang, R. Zhao, Z. Zhao, W. Li, D. Zhao and D. Chao, *J. Am. Chem. Soc.*, 2023, **145**, 10880–10889.

163 Z. Pei, Z. Zhu, D. Sun, J. Cai, A. Mosallanezhad, M. Chen and G. Wang, *Mater. Res. Bull.*, 2021, **141**, 111347.

164 J. Zhang, G. Jiang, P. Xu, A. Ghorbani Kashkooli, M. Mousavi, A. Yu and Z. Chen, *Energy Environ. Sci.*, 2018, **11**, 2010–2015.

165 C. Bai, F. Cai, L. Wang, S. Guo, X. Liu and Z. Yuan, *Nano Res.*, 2018, **11**, 3548–3554.

166 L. Hang, W. Li, H. Wen, T. Zhang and G. Jiang, *Chem. Eng. J.*, 2022, **443**, 136230.

167 F. Chen, X. Chen, Q. Hao, X. Sun and N. Li, *Nanoscale*, 2022, **14**, 15269–15274.

168 Y. Ji, J. Xu, Z. Wang, M. Ren, Y. Wu, W. Liu, J. Yao, C. Zhang and H. Zhao, *J. Electroanal. Chem.*, 2023, **931**, 117188.

169 J. Xu, W. Ma, L. Ge, M. Ren, X. Cai, W. Liu, J. Yao, C. Zhang and H. Zhao, *J. Alloys Compd.*, 2022, **912**, 165151.

170 T. Liu, H. Wang, C. Lei, Y. Mao, H. Wang, X. He and X. Liang, *Energy Storage Mater.*, 2022, **53**, 544–551.

171 D. Yu, A. Kumar, T. A. Nguyen, M. T. Nazir and G. Yasin, *ACS Sustainable Chem. Eng.*, 2020, **8**, 13769–13776.

172 Z. Gong, C. Song, C. Bai, X. Zhao, Z. Luo, G. Qi, X. Liu, C. Wang, Y. Duan and Z. Yuan, *Sci. China Mater.*, 2022, **66**, 556–566.

173 K. Lu, H. Zhang, B. Song, W. Pan, H. Ma and J. Zhang, *Electrochim. Acta*, 2019, **296**, 755–761.

174 S. Chai, J. Yao, Y. Wang, J. Zhu and J. Jiang, *Chem. Eng. J.*, 2022, **439**, 135676.

175 C. Chen, Z. Li, Y. Xu, Y. An, L. Wu, Y. Sun, H. Liao, K. Zheng and X. Zhang, *ACS Sustainable Chem. Eng.*, 2021, **9**, 13268–13276.
176 Y. He, M. Liu, S. Chen and J. Zhang, *Sci. China: Chem.*, 2021, **65**, 391–398.
177 W. Liu, P. Liu, Y. Lyu, J. Wen, R. Hao, J. Zheng, K. Liu, Y. J. Li and S. Wang, *ACS Appl. Mater. Interfaces*, 2022, **14**, 8955–8962.
178 S. Chen, Y. He, S. Ding and J. Zhang, *J. Phys. Chem. C*, 2023, **127**, 7609–7617.
179 Y. Hou, C. Zhu, Q. Wang, X. Zhao, K. Luo, Z. Gong and Z. Yuan, *Chin. Chem. Lett.*, 2023, 108697, DOI: 10.1016/j.cclet.2023.108697.
180 J. Sun, H. Ma and D. Wang, *J. Alloys Compd.*, 2023, **947**, 169696.
181 L. Ma, G. Zhu, Z. Wang, A. Zhu, K. Wu, B. Peng, J. Xu, D. Wang and Z. Jin, *Nano Lett.*, 2023, **23**, 5272–5280.
182 X. Yang, H. Fan, F. Hu, S. Chen, K. Yan and L. Ma, *Nano-Micro Lett.*, 2023, **15**, 126.
183 M. Liu, Q. Chen, X. Cao, D. Tan, J. Ma and J. Zhang, *J. Am. Chem. Soc.*, 2022, **144**, 21683–21691.
184 S. Ding, Q. Chen, S. Chen, Y. Tian and J. Zhang, *Chin. Chem. Lett.*, 2023, **34**, 108232.
185 S. Niu, B. Zhao and D. Liu, *ACS Appl. Mater. Interfaces*, 2023, **15**, 25558–25566.
186 X. Zeng, X. Meng, W. Jiang, J. Liu, M. Ling, L. Yan and C. Liang, *ACS Sustainable Chem. Eng.*, 2020, **8**, 14280–14285.
187 D. Lin, D. Rao, S. Chiovoloni, S. Wang, J. Q. Lu and Y. Li, *Nano Lett.*, 2021, **21**, 4129–4135.
188 X. Miao, Q. Chen, Y. Liu, X. Zhang, Y. Chen, J. Lin, S. Chen and Y. Zhang, *Electrochim. Acta*, 2022, **415**, 140206.
189 W. Wu, C. Li, Z. Wang, H.-Y. Shi, Y. Song, X.-X. Liu and X. Sun, *Chem. Eng. J.*, 2022, **428**, 131283.
190 L. Ma, Y. Ying, S. Chen, Z. Huang, X. Li, H. Huang and C. Zhi, *Angew. Chem., Int. Ed.*, 2021, **60**, 3791–3798.
191 W. Gao, S. Cheng, Y. Zhang, E. Xie and J. Fu, *Adv. Funct. Mater.*, 2023, **33**, 2211979.
192 G. Kasiri, R. Trócoli, A. B. Hashemi and F. La Mantia, *Electrochim. Acta*, 2016, **222**, 74–83.
193 B. Tang, L. Shan, S. Liang and J. Zhou, *Energy Environ. Sci.*, 2019, **12**, 3288–3304.
194 F. C. Anson and J. J. Lingane, *J. Am. Chem. Soc.*, 1957, **79**, 1015–1020.
195 Y. A. Fialkov, *Bull. Acad. Sci. USSR, Div. Chem. Sci.*, 1954, **3**, 847–855.
196 F. A. Philbrick, *J. Am. Chem. Soc.*, 1934, **56**, 1257–1259.
197 R. Whitaker, J. Ambrose and C. Hickam, *J. Inorg. Nucl. Chem.*, 1961, **17**, 254–256.
198 Y. L. Wang, J. C. Nagy and D. W. Margerum, *J. Am. Chem. Soc.*, 1989, **111**, 7838–7844.
199 Y. Bichsel and U. Von Gunten, *Environ. Sci. Technol.*, 1999, **33**, 4040–4045.
200 E. T. Urbansky, B. T. Cooper and D. W. Margerum, *Inorg. Chem.*, 1997, **36**, 1338–1344.
201 A. J. Downs and C. J. Adams, *The Chemistry of Chlorine, Bromine, Iodine and Astatine: Pergamon Texts in Inorganic Chemistry*, Elsevier, 1973, vol. 7.
202 Y. Ji, J. Xie, Z. Shen, Y. Liu, Z. Wen, L. Luo and G. Hong, *Adv. Funct. Mater.*, 2023, **33**, 2210043.
203 X. Qu, Y. Tang, X. He, J. Zhou, Z. Tang, W. Feng and J. Liu, *J. Electrochem.*, 2022, 211026, DOI: 10.13208/j.electrochem.211026.
204 J. Zhang, Q. Dou, C. Yang, L. Zang and X. Yan, *J. Mater. Chem. A*, 2023, **11**, 3632–3639.
205 G. Chen, Y. Kang, H. Yang, M. Zhang, J. Yang, Z. Lv, Q. Wu, P. Lin, Y. Yang and J. Zhao, *Adv. Funct. Mater.*, 2023, **33**, 2300656.
206 X. Jin, L. Song, C. Dai, Y. Xiao, Y. Han, X. Li, Y. Wang, J. Zhang, Y. Zhao, Z. Zhang, N. Chen, L. Jiang and L. Qu, *Adv. Mater.*, 2022, **34**, 2109450.
207 W. Shang, J. Zhu, Y. Liu, L. Kang, S. Liu, B. Huang, J. Song, X. Li, F. Jiang, W. Du, Y. Gao and H. Luo, *ACS Appl. Mater. Interfaces*, 2021, **13**, 24756–24764.
208 F. Wang, J. Tseng, Z. Liu, P. Zhang, G. Wang, G. Chen, W. Wu, M. Yu, Y. Wu and X. Feng, *Adv. Mater.*, 2020, **32**, 2000287.
209 L. Xu, E.-Y. Choi and Y.-U. Kwon, *Inorg. Chem. Commun.*, 2008, **11**, 1190–1193.
210 Y. Hou, F. Kong, Z. Wang, M. Ren, C. Qiao, W. Liu, J. Yao, C. Zhang and H. Zhao, *J. Colloid Interface Sci.*, 2022, **629**, 279–287.
211 Y. Zhang, T. Zhao, S. Yang, Y. Zhang, Y. Ma and Z. Wang, *J. Energy Chem.*, 2022, **75**, 310–320.
212 L. Zhang, J. Huang, H. Guo, L. Ge, Z. Tian, M. Zhang, J. Wang, G. He, T. Liu, J. Hofkens, D. J. L. Brett and F. Lai, *Adv. Energy Mater.*, 2023, **13**, 2203790.
213 Z. Wang, J. Huang, Z. Guo, X. Dong, Y. Liu, Y. Wang and Y. Xia, *Joule*, 2019, **3**, 1289–1300.
214 T.-T. Su, J.-B. Le, K. Wang, K.-N. Liu, C.-Y. Shao, W.-F. Ren and R.-C. Sun, *J. Power Sources*, 2022, **550**, 232136.
215 Y. Tian, S. Chen, Y. He, Q. Chen, L. Zhang and J. Zhang, *Nano Res. Energy*, 2022, **1**, e9120025.
216 H. Peng, Y. Fang, J. Wang, P. Ruan, Y. Tang, B. Lu, X. Cao, S. Liang and J. Zhou, *Matter*, 2022, **5**, 4363–4378.
217 S. Chen, Q. Chen, J. Ma, J. Wang, K. S. Hui and J. Zhang, *Small*, 2022, **18**, e2200168.
218 Y. Zhang, L. Wang, Q. Li, B. Hu, J. Kang, Y. Meng, Z. Zhao and H. Lu, *Nano-Micro Lett.*, 2022, **14**, 208.
219 W. Shang, Q. Li, F. Jiang, B. Huang, J. Song, S. Yun, X. Liu, H. Kimura, J. Liu and L. Kang, *Nano-Micro Lett.*, 2022, **14**, 82.
220 R. Yi, X. Shi, Y. Tang, Y. Yang, P. Zhou, B. Lu and J. Zhou, *Small Struct.*, 2023, **4**, 2300020.
221 H. X. Dang, A. J. Sellathurai and D. P. J. Barz, *Energy Storage Mater.*, 2023, **55**, 680–690.
222 L. Yan, T. Liu, X. Zeng, L. Sun, X. Meng, M. Ling, M. Fan and T. Ma, *Carbon*, 2022, **187**, 145–152.
223 K. Wang, J.-B. Le, S.-J. Zhang, W.-F. Ren, J.-M. Yuan, T.-T. Su, B.-Y. Chi, C.-Y. Shao and R.-C. Sun, *J. Mater. Chem. A*, 2022, **10**, 4845–4857.
224 J. Yang, R. Zhao, Y. Wang, Z. Hu, Y. Wang, A. Zhang, C. Wu and Y. Bai, *Adv. Funct. Mater.*, 2023, **33**, 2213510.
225 Q. P. Jian, M. C. Wu, H. R. Jiang, Y. K. Lin and T. S. Zhao, *J. Power Sources*, 2021, **484**, 229238.

226 M. Mousavi, G. Jiang, J. Zhang, A. G. Kashkooli, H. Dou, C. J. Silva, Z. P. Cano, Y. Niu, A. Yu and Z. Chen, *Energy Storage Mater.*, 2020, **32**, 465–476.

227 G.-M. Weng, Z. Li, G. Cong, Y. Zhou and Y.-C. Lu, *Energy Environ. Sci.*, 2017, **10**, 735–741.

228 Y. Zhao, Y. Li, J. Mao, Z. Yi, N. Mubarak, Y. Zheng, J.-K. Kim and Q. Chen, *J. Mater. Chem. A*, 2022, **10**, 14090–14097.

229 S. Ito, M. Sugimasa, Y. Toshimitsu, A. Orita, M. Kitagawa and M. Sakai, *Electrochim. Acta*, 2019, **319**, 164–174.

230 J. Yang, Y. Song, Q. Liu and A. Tang, *J. Mater. Chem. A*, 2021, **9**, 16093–16098.

231 C. Xie, H. Zhang, W. Xu, W. Wang and X. Li, *Angew. Chem., Int. Ed.*, 2018, **57**, 11171–11176.

232 C. Xie, Y. Liu, W. Lu, H. Zhang and X. Li, *Energy Environ. Sci.*, 2019, **12**, 1834–1839.

233 L. Gao, Y. Ding, G. He and G. Yu, *Small*, 2022, **18**, 2107055.

234 P. Tangthuam, J. Pimoei, A. A. Mohamad, F. Mahlendorf, A. Somwangthanaroj and S. Kheawhom, *Heliyon*, 2020, **6**, e05391.

235 Z. Yuan, X. Liu, W. Xu, Y. Duan, H. Zhang and X. Li, *Nat. Commun.*, 2018, **9**, 3731.

236 C. Zhang, L. Zhang, Y. Ding, S. Peng, X. Guo, Y. Zhao, G. He and G. Yu, *Energy Storage Mater.*, 2018, **15**, 324–350.

237 M. Mousavi, H. Dou, H. Fathiannasab, C. J. Silva, A. Yu and Z. Chen, *Chem. Eng. J.*, 2021, **412**, 128499.

238 J. Liu, T. Ma, M. Zhou, S. Liu, J. Xiao, Z. Tao and J. Chen, *Inorg. Chem. Front.*, 2019, **6**, 731–735.

239 B. Li, J. Liu, Z. Nie, W. Wang, D. Reed, J. Liu, P. McGrail and V. Sprenkle, *Nano Lett.*, 2016, **16**, 4335–4340.

240 A. A. Williams, R. K. Emmett and M. E. Roberts, *Phys. Chem. Chem. Phys.*, 2023, **25**, 16222–16226.

241 X. Wu, A. Markir, Y. Xu, C. Zhang, D. P. Leonard, W. Shin and X. Ji, *Adv. Funct. Mater.*, 2019, **29**, 1900911.

242 Y. Fang, Z. Chen, L. Xiao, X. Ai, Y. Cao and H. Yang, *Small*, 2018, **14**, 1703116.

243 L. Yu, F.-C. Liu and Z.-W. Fu, *Electrochim. Acta*, 2009, **54**, 2818–2822.

244 Y. Zhang, S. Liu, Y. Ji, J. Ma and H. Yu, *Adv. Mater.*, 2018, **30**, 1706310.

245 Z.-W. Fu, L. Yu, S.-C. Cheng, J. Yao and H. Li, *Electrochem. Commun.*, 2007, **9**, 1–5.

246 K. Zhang and Z. Jin, *Energy Storage Mater.*, 2022, **45**, 332–369.

247 D. Aurbach, Z. Lu, A. Schechter, Y. Gofer, H. Gizbar, R. Turgeman, Y. Cohen, M. Moshkovich and E. Levi, *Nature*, 2000, **407**, 724–727.

248 H. D. Yoo, I. Shterenberg, Y. Gofer, G. Gershinsky, N. Pour and D. Aurbach, *Energy Environ. Sci.*, 2013, **6**, 2265–2279.

249 Z. Liu, X. Pu, W. Hu, F. Gao and H. Deng, *J. Phys. Chem. C*, 2018, **122**, 28518–28527.

250 X. Chen, T. Hou, K. A. Persson and Q. Zhang, *Mater. Today*, 2019, **22**, 142–158.

251 M. Chen, W. Zhu, H. Guo, Z. Tian, L. Zhang, J. Wang, T. Liu, F. Lai and J. Huang, *Energy Storage Mater.*, 2023, **59**, 102760.

252 Y. Wu and N. Liu, *Chem*, 2018, **4**, 438–465.

253 R. E. Ciez and J. F. Whitacre, *Nat. Sustainability*, 2019, **2**, 148–156.

254 J. Zheng, D. Lv, M. Gu, C. Wang, J.-G. Zhang, J. Liu and J. Xiao, *J. Electrochem. Soc.*, 2013, **160**, A2288.

255 D. Lv, J. Zheng, Q. Li, X. Xie, S. Ferrara, Z. Nie, L. B. Mehdi, N. D. Browning, J. G. Zhang and G. L. Graff, *Adv. Energy Mater.*, 2015, **5**, 1402290.

256 L. Luo and A. Manthiram, *ACS Energy Lett.*, 2017, **2**, 2205–2211.

257 M. Zhao, B. Q. Li, H. J. Peng, H. Yuan, J. Y. Wei and J. Q. Huang, *Angew. Chem., Int. Ed.*, 2020, **59**, 12636–12652.

258 C. Wang, K. Fu, S. P. Kammampata, D. W. McOwen, A. J. Samson, L. Zhang, G. T. Hitz, A. M. Nolan, E. D. Wachsman, Y. Mo, V. Thangadurai and L. Hu, *Chem. Rev.*, 2020, **120**, 4257–4300.

259 L. Fan, S. Li, L. Liu, W. Zhang, L. Gao, Y. Fu, F. Chen, J. Li, H. L. Zhuang and Y. Lu, *Adv. Energy Mater.*, 2018, **8**, 1802350.

260 Z. Zhao, J. Zhao, Z. Hu, J. Li, J. Li, Y. Zhang, C. Wang and G. Cui, *Energy Environ. Sci.*, 2019, **12**, 1938–1949.

261 J. Fu, X. Ji, J. Chen, L. Chen, X. Fan, D. Mu and C. Wang, *Angew. Chem.*, 2020, **132**, 22378–22385.

262 G. Zampardi and F. La Mantia, *Nat. Commun.*, 2022, **13**, 687.

263 L. Yan, S. Zhang, Q. Kang, X. Meng, Z. Li, T. Liu, T. Ma and Z. Lin, *Energy Storage Mater.*, 2023, **54**, 339–365.

264 L. Qiao, C. Wang and X. S. Zhao, *ACS Appl. Energy Mater.*, 2021, **4**, 7012–7019.

265 Q. Zhang, F.-H. Li, X.-X. Zhang, H.-B. Wang, F.-C. Li, Z.-Y. Guo and Z. Zhang, *J. Electrochem. Soc.*, 2021, **168**, 040522.

266 Y. Zhao, N. B. Mercier and H. R. Byon, *ChemPlusChem*, 2015, **80**, 344–348.

267 J. Xu, J. Wang, L. Ge, J. Sun, W. Ma, M. Ren, X. Cai, W. Liu and J. Yao, *J. Colloid Interface Sci.*, 2022, **610**, 98–105.

268 Q. Guo, H. Wang, X. Sun, Y. N. Yang, N. Chen and L. Qu, *ACS Mater. Lett.*, 2022, **4**, 1872–1881.

269 Y. Wu, Y. Qian, C. Huang, Y. Zhang, Y. Yang, A. Hu, Q. Tang and X. Chen, *Electrochim. Acta*, 2023, **460**, 142593.

270 Y. Du, R. Kang, H. Jin, W. Zhou, W. Zhang, H. Wang, J. Qin, J. Wan, G. Chen and J. Zhang, *Adv. Funct. Mater.*, 2023, 2304811, DOI: **10.1002/adfm.202304811**.

271 D. Zhao, Q. Zhu, Q. Zhou, W. Zhang, Y. Yu, S. Chen and Z. Ren, *Energy Environ. Mater.*, 2022, e12522, DOI: **10.1002/eem2.12522**.

272 Q. Chen, S. Chen and J. Zhang, *J. Power Sources*, 2023, **556**, 232529.

273 W. Han and X. Li, *J. Power Sources*, 2023, **580**, 233296.